

NOAA Technical Report ERL 402-NHEML 2



Influence of Earth Surface and Cloud Properties on the South Florida Sea Breeze

Patrick T. Gannon, Sr.

September 1978



U. S. DEPARTMENT OF COMMERCE
National Oceanic and Atmospheric Administration
Environmental Research Laboratories



Digitized by the Internet Archive
in 2013

<http://archive.org/details/influenceofearth00gann>



Influence of Earth Surface and Cloud Properties on the South Florida Sea Breeze

Patrick T. Gannon, Sr.
National Hurricane and Experimental Meteorology Laboratory
Coral Gables, Florida

September 1978

U. S. DEPARTMENT OF COMMERCE

Juanita M. Kreps, Secretary

National Oceanic and Atmospheric Administration

Richard A. Frank, Administrator

Environmental Research Laboratories

Boulder, Colorado

Wilmot Hess, Director

NOTICE

The Environmental Research Laboratories do not approve, recommend, or endorse any proprietary product or proprietary material mentioned in this publication. No reference shall be made to the Environmental Research Laboratories or to this publication furnished by the Environmental Research Laboratories in any advertising or sales promotion which would indicate or imply that the Environmental Research Laboratories approve, recommend, or endorse any proprietary product or proprietary material mentioned herein, or which has as its purpose an intent to cause directly or indirectly the advertised product to be used or purchased because of this Environmental Research Laboratories publication.

CONTENTS

	Page
Abstract	1
1. INTRODUCTION	1
1.1 Differential Surface Heating and the Sea Breeze	1
1.2 Content of the Study	1
1.3 Previous Observational Studies of Sea and Lake Breeze Circulations	2
1.4 Previous Theoretical Studies of Land-Water Circulations	4
1.5 Objectives of the Study	5
1.6 Summary	5
2. PHYSICAL PROPERTIES OF THE SURFACE	6
2.1 Surface Albedo	6
2.2 Thermal Inertia	7
2.3 Soil Moisture	8
2.4 Summary	10
3. STUDY AREA	11
3.1 Physical Features of Study Area	11
3.2 Soil and Vegetation Profiles	12
3.3 Summary	13
4. OBSERVATIONS TO SUPPORT THEORETICAL MODEL	15
4.1 Systems Employed for Data Acquisition	15
4.2 Albedo of the Surface	16
4.3 Solar Radiation	17
4.4 Evaporation	18
4.5 Emissivity	19
4.6 Soil Surface Temperatures	19
4.7 Water Surface Temperatures	21
4.8 Inference of Thermal Inertia	21
4.9 Summary	24
5. THEORETICAL ELEMENTS	24
5.1 Model Dynamic Equations	25
5.2 Model Surface Layer and Planetary Boundary Layer	26
5.3 Heating Function	29
5.4 Solar Spectrum	29
5.5 Solar Energy Transfer Processes	30
5.6 Long-Wave Radiation Transfer	33
5.7 Surface Heating Method	34
5.8 Model Domain and Grid Spacing	35
5.9 Initialization of the Model	36
5.10 Computational Sequence	36
5.11 Summary	37
6. NUMERICAL EXPERIMENTS	37
6.1 Design of Experiments	38
6.2 Results: Systematic Variations of Surface Properties Uniformly and Singly Prescribed for All Land Grid Points	42
6.3 Results: Systematic Variations of Surface Properties Uniformly and Singly Prescribed for Coastal Zones	46
6.4 Results: Systematic Variations of Surface Properties Uniformly and Simultaneously Prescribed for Coastal Zones	48
6.5 Results: Systematic Variations of Cirrus Cloud Optical Properties Uniformly Prescribed for All Land Grid Points	50
6.6 Results: Systematic Variation of Thick Cirrus Cloud Optical Properties Uniformly Prescribed for Interior and Coastal Zones	50
6.7 Importance of Evaporation Over South Florida	51
6.8 Summary of Sensitivity Studies	53
6.9 Case Study of July 16, 1975	54

CONTENTS (Continued)

	Page
7. SUMMARY AND CONCLUSIONS	69
7.1 Summary of the Problem	69
7.2 Summary of Observational Study	69
7.3 Summary of Numerical Modeling Experiments	69
7.4 Conclusions	70
7.5 Suggestions for Further Research	71
8. ACKNOWLEDGMENTS	71
9. REFERENCES	72
10. BIBLIOGRAPHY	74
APPENDIX A. RADIATION TRANSFER EQUATIONS	77
APPENDIX B. DENSITOMETER TECHNIQUES FOR DERIVATION OF CLOUD PROPERTIES	87
APPENDIX C: SOIL MOISTURE HISTORY: JULY 1 to 16, 1975	89

INFLUENCE OF EARTH SURFACE AND CLOUD PROPERTIES ON THE SOUTH FLORIDA SEA BREEZE

Patrick T. Gannon, Sr.

ABSTRACT. A two-dimensional numerical sea breeze model that includes radiation and heat budget physics is used to study sea breeze circulations affected by South Florida surface and cloud conditions. Sensitivity experiments show major differences in the intensities and inland penetrations that result from prescribed distributions of surface and cirrus cloud properties. A case study experiment for July 16, 1975, provides a measure of the importance of surface and cumulus cloud properties that were observed or deduced for this one day. Significant differences exist between the model version using a surface heat budget formulation and the version using prescribed thermal forcing. The strength of the sea breeze predicted with the heat budget formulation decreases with increasing initial basic state wind speeds, while the opposite effect occurs with thermal forcing. Soil moisture is the dominant controlling surface property, followed by albedo and thermal inertia. Cirrus clouds can prevent the evolution of the sea breeze when the geometric thickness of cirrus exceeds 2 km. A case study demonstrates the importance of cumulus cloud shielding of the surface from solar radiation. The mesoscale sea breeze convergence zone is seen to evolve adjacent to organized cloud fields, but not necessarily coincident with them. This is an important consideration when sea breeze models are verified with observed cloud fields.

1. INTRODUCTION

1.1 Differential Surface Heating and the Sea Breeze

Most investigators of the sea breeze or related land-water circulations have specified the land and sea temperatures as either constant or as simple periodic heating functions, or as randomized temperature perturbations. This investigation was conducted to determine the nature of the physical factors related to the heating of the surface, the communication of this heating to the overlying atmosphere, and the effects of this heating on the sea breeze.

This study, the first detailed investigation to determine the effects of surface properties and clouds on the sea breeze over South Florida, has relevance for South Florida agencies concerned with weather modification, weather forecasting, hydrology, water management, agriculture, and environmental alteration. Transferability of the results is greatest for tropical areas that experience atmospheric land-water circulations similar to the sea breeze.

1.2 Content of the Study

This modeling study, which relies heavily upon actual observations, describes the effects of topographical inhomogeneities and clouds in altering the location, structure, and intensity of the South Florida sea breeze. These inhomogeneities and clouds exercise their influence through the establishment of temporal and spatial variations in land surface temperature.

The physical properties of the topography that exercise a control over surface heating are the surface albedo, surface thermal inertia, and soil moisture. Albedo is here defined as the ratio of the total direct and diffuse solar radiant energy reflected from the land surface to that total direct and diffuse solar energy incident upon it. Thermal inertia is a measure of the resistance of a given material to a change in temperature. Thermal inertia is equal to $(K\rho C)^{1/2}$ where K is thermal conductivity, ρ is soil density, and C is specific heat. Variations in ground surface temperature depend

on thermal inertia, while the variation of temperature with depth depends on both conductivity (or diffusivity) and density (Kahle et al., 1975; Sutton, 1953). Although thermal inertia is not measurable directly with remote sensing, it can be inferred, under certain conditions, from observations of the diurnal temperature change of the surface and the surface albedo (Pohn et al., 1974). Low thermal inertias correspond to large diurnal temperature amplitudes; the opposite holds for high thermal inertias. Soil moisture is a surface property of great importance in the surface heat budget. The evapotranspiration component is directly dependent upon the amount of soil moisture in the upper few centimeters of the soil. It will be shown that this component is the major soil property determining the diurnal amplitude of surface heating and the flux of water vapor into the boundary layer. Albedo, thermal inertia, and soil moisture are discussed in greater detail in Section 2.

Cumuliform and high clouds, if present over a region before sea breeze generation over that region, exercise a major control over the surface heating pattern. When formed as a result of the mesoscale convergence in the vicinity of the sea breeze "front," these clouds create an interacting effect by shielding the surface from solar radiation. This interacting effect is not necessarily negative. It can be positive in such a way that the convergence and upward motions associated with the sea breeze front are amplified. Amplification results from the increased gradient of surface heating that is created between the cloud-free and cloudy region. It will be shown that clouds alter the basic sea breeze thermal and motion fields in which they were generated.

Sea breeze circulation is affected by the spatial variations of surface heating through vertical turbulent transfer of heat, momentum, moisture, and horizontal advection of these properties. Diffusion of these properties proceeds upward through the surface layer and modifies the overlying planetary boundary layer. The sea breeze circulation is altered as a result.

The sea breeze is an important mechanism for the organization of the fields of heat, moisture, and momentum before the onset of significant convective processes. It has been established, through analysis of motion fields derived from high-density wind observations (Garstang, 1974; Ulanski, 1976, personal communication; Cunnig, 1976, personal communication), that well-defined mesoscale convergence fields of heat, moisture, and mass, clearly associated with the sea breeze, exist about 1 to 2 hours before the onset of significant cloudiness and precipitation. The validity of employing a numerical sea breeze

model that does not simulate moist convection and release of latent heat (a dry model) to determine the peninsula-scale precursor convergence fields has been established by Pielke and Mahrer (1976). If the location and magnitude of these convergence fields are more correctly simulated through inclusion of surface property and cloud effects in numerical models, a diversity of problem areas can be investigated.

This study was motivated by the desire to resolve critical questions relating to the following potential applications:

- 1) Enhanced capability to predict favorable conditions for conventional weather modification activities designed to promote cloud merger and increased rainfall.

- 2) Simulation of the effects of proposed mesoscale weather modification techniques involving dispersion of particles at cirriform cloud levels to induce surface differential heating (Gray et al., 1976).

- 3) Improvement of daily summer season weather forecasting for regions that experience convection resulting from sea and lake breezes (Cotton and Pielke, 1976).

- 4) Evaluation of the effects of past and proposed alteration of natural surface topography, these effects to include inadvertent weather modification and redistribution of rainfall that results from quasi-permanent deviations in sea breeze location and intensity.

This study evaluates the influence of surface albedo, surface thermal inertia, soil moisture, and clouds with the aid of a numerical sea breeze model. The model includes sophisticated radiation and heat budget formulations. Observations of surface temperature, radiation, and cloud cover in the study area are provided to support the choices of albedo, thermal inertia, soil moisture, and cloud properties used in model simulations.

1.3 Previous Observational Studies of Sea and Lake Breeze Circulations

Previous observation programs have identified characteristics common to a variety of sea and lake breeze circulations that occur under varying synoptic and terrain conditions: the presence of a return flow aloft; the sea and lake breeze front and associated convergence zone; the rotation to the right in the Northern Hemisphere, as time progresses, of the wind vector by Coriolis acceleration; the inverse relationship between larger scale wind speed and intensity of the circulation; and

the tendency for cumuliform clouds to form in the convergence zones. Although some investigators suggest that spatial variations in surface properties are relevant, systematic observations of time and space variations in surface properties are inadequate. Furthermore, the influence of changes in these properties on land-water circulations has not been sufficiently observed or modeled. Cloud interaction effects caused by the shielding of the surface from solar radiation have not been investigated.

Fisher's (1960) observations verified the cellular structure of the sea breeze. The vertical temperature structure exhibited lapse rates greater than dry adiabatic during peak heating hours. These became less than dry adiabatic as cooler ocean air advected inland later in the day. Fisher stressed that sea breeze observations could not be completely isolated from the large-scale flow pattern. This has been well substantiated by subsequent investigators (Tingle, 1971). Curvature and irregularities in the coastline were seen to affect the sea breeze structure. However, radiation, air-surface heat budget, and cloud interaction observations were not made in this study.

Moroz (1967) investigated the lake breeze on the eastern shore of Lake Michigan. His most interesting observation concerned the pulsing behavior of the lake breeze where it was observed to alternately accelerate and decelerate. No mention was made of specific thermal, moisture, or cloud patterns that existed with this behavior. Moroz held that the extent and features of the land- and water-induced atmospheric flow systems are strongly dependent upon the heat distribution at the surface.

Hsu (1969) conducted an extensive observational study of the Texas Coast sea breeze. This study differed in scope from earlier investigations in that small, medium, and mesoscale variations were studied. The composite network observations were also used to synthesize a three-dimensional model of the Texas Coast sea breeze. Hsu recognized the influence of variations in vegetative cover and soil properties, but did not measure heat budget components (radiation, evaporation, sensible heat, etc.) during the experiment. The formation of cumulus clouds in the sea breeze convergence zone was noted, but radiation-related interaction effects were not investigated.

Bhumralkar (1974) did an observational study of the "heated island" effect at Grand Bahama Island. The observations verify the importance of latent heat release and microphysical processes in convection. The resultant interaction on atmospheric motion arising from surface cooling due to rainfall is demonstrated. However, the

relationship of time- and space-dependent differential surface heating from surface properties and clouds on the development of the convergence zone was not expressly investigated.

Estoque et al. (1976) performed a combined observational and numerical study of the lake breeze over Lake Ontario. They found the structure and behavior of the Lake Ontario breeze similar to the breezes studied by Moroz over Lake Michigan. Their determination that a reduction in lake breeze intensity results from a reduction in lake-land temperature differences is important for the South Florida case. A decrease in intensity should occur in late summer as insolation decreases and the sea surface temperatures reach their maximum value.

Although not observed in conjunction with a sea breeze circulation experiment, the cloud cover effect described by Weiss and Purdom (1974) is considered relevant. They provide striking evidence of the influence of early morning cloud cover with its associated surface cooling on the outbreak of afternoon convection on the mesoscale.

Plank (1962), in a study of cumulus clouds over Florida, noted the importance of topographical features in the location of cloud groups and bands. Although his study was more oriented towards the cumulus scale, cloud groups and lines on the scale of the sea breeze were also seen to be anchored to topographical features. Pielke (1973) also noted this topographical influence on the sea breeze over Florida.

During the NOAA 1973 Florida Area Cumulus Experiment (FACE), surface, radar, satellite, rawinsonde, aircraft, and photographic observations were composited to provide a three-dimensional picture of the evolution of organized convection over South Florida as it occurred in the sea breeze convergence zone (Pielke and Cotton, 1977). If one accepts that the presence of a line of visible cumuliform clouds (before downdrafts) denotes the general location of sea breeze convergence zones, then this type of study employing multiple visual acquisition platforms represents an advance over former observational experiments.

From the point of view of this paper, none of the aforementioned programs provides sufficient documentation of the effect of spatial and temporal variations in surface properties (e.g., soil moisture) and clouds on the evolution of the mesoscale sea breeze convergence zone. The principal difficulty is the lack of sufficient conventional and remote (satellite) observations of surface properties to allow for accurate observation or numerical simulation of the diurnal heating cycle.

1.4 Previous Theoretical Studies of Land-Water Circulations

Numerical experiments have been conducted on sea and lake breezes. The atmospheric forcing in many of these experiments arises as a result of surface temperatures which are prescribed as a function of time. In some cases, the land surface is prescribed as an elevated heat source during the computations. The response of the perturbed atmosphere over a surface subjected to differential temporal and spatial heating has not been investigated in great detail. This differential heating arises from variations in radiation, cloud cover, and thermal properties.

Estoque (1962) prescribed a temperature wave of a specific form at the land surface in an early numerical experiment. He identified the primary physical processes acting to initiate and maintain the sea breeze. The imposed temperature wave results in a differential heating through turbulent transfer processes, and there is established a horizontal pressure gradient force. Eddy viscosity then continuously modifies the motion field. Subsequent numerical and observational experiments have consistently verified Estoque's results, showing the sensitivity of sea breeze intensity, extent, and shape on the prevailing geostrophic flow. The intensity of the sea breeze circulation was defined by the magnitude of the vertical motion. It was found that with a basic wind flow perpendicular to the coastline, stronger vertical motions occurred with a wind speed of 5 m s^{-1} compared to a no-motion (zero wind speed) case. In comparing offshore and onshore wind regimes, the maximum upward motion occurred when the basic flow was offshore. This flow regime contributes to an increased horizontal pressure gradient near the coastline as the air in contact with the surface is heated as it is advected toward the coast.

Estoque and Bhumralkar (1969), in an experiment that simulated flow over a heated island, specified the temperature as constant and 10°C higher for a narrow (10 km) heat source and varying wind conditions. This study on the narrow island suggests that induced circulations are weak when the prevailing flow is strong and normal to the heat source. Horizontal variations in momentum and heat fluxes resulted solely from the local heat source. However, the perturbations in potential temperature and wind 3 hours after the initial time were seen to extend about 20 km downwind with a basic flow of 10 m s^{-1} . This pattern was associated with downward motion over the heat source itself. The induced perturbations are stronger for the case where the basic wind flow is

parallel to the island and, in this case, upward motions prevail over the heat source.

McPherson (1968), in his three-dimensional numerical experiment on the Texas coast sea breeze, allowed the land to heat in a sinusoidal manner. The model predicted, in accordance with observations, that near-surface potential temperature rises to a maximum before the passage of the sea breeze convergence zone and then decreases. Tingle (1971) employed the observed diurnal surface (shelter) temperature wave as the driving force of his model circulation. Pielke (1973) also employed a sinusoidal surface heating function.

Walsh (1974), in an analytic analysis of the sea breeze, also specified the temperature deviation as a simple sinusoidal function. Hill (1974) specified the surface heating as randomized temperature perturbations. Neumann and Mahrer (1975), in a study of lake and land breezes, imposed a diurnal temperature wave that was both time- and space-dependent.

Pearson (1973), in an analytic and numerical study of the sea breeze, evaluated the contribution of inertial gravity waves and nonlinear terms to the development of the sea breeze. Arbitrary spatial and temporal heating functions were employed to evaluate sea breeze response. The velocity of the sea breeze front was found to depend only on the total heat input into the air above the surface. The major structure of the sea breeze circulation was found to be relatively independent of the way final inland temperature is obtained. However, Pearson recognized the need for a modeling effort that considered radiation, evaporation, surface thermal response, and cloud shadow zones. He stressed that specification of the temperature at the ground as horizontally homogeneous is unrealistic. This latter procedure does not allow heat transferred to the air to cool the land surface, for the land is being forced to act as an infinite heat source. The lower boundary condition should be formulated in terms of a heat budget at the surface.

Of particular relevance to this work is the more recent study of Otterman (1975). Otterman invokes the "thermal mountain" concept first introduced by Stern and Malkus (1953). This concept helps explain local air-mass uplift over a heated island and enhancement of the sea breeze as shown by the numerical model results of Estoque and Bhumralkar (1969). The thermal mountain, $M(x)$, is defined as the vertical displacement of a streamline from its undisturbed level over a heated island or relative heat source located within a larger domain. Mathematically, it is represented by

$$M(x) = \frac{T}{sT_m} [1 - e^{-gsKx/U^3}].$$

$M(x)$ is the shape of the mountain above the heat source, where τ is the uniformly elevated temperature of the surface, x is the distance along wind direction from edge of the heat source, s is stability, T_m is air temperature, U is wind speed, g is the acceleration of gravity, and K is eddy conductivity. It is seen that, for a finite heat source of distance x , $M(x)$ will be maximized for light winds and high values of τ , all other factors held constant. If the width of the heat source (x) is allowed to increase, the mountain will grow further.

This brief review of theoretical studies of sea and lake breezes reveals that previous researchers recognized the role of surface heating. The specific changes in circulation location and intensity resulting from variable surface properties and clouds were not studied. Pearson's findings concerning the influence of variable heating and his suggestion that the effect of heat budget components be studied in detail are highly significant to the present work.

1.5 Objectives of the Study

As the natural surface of the earth is characterized by inhomogeneities, and clouds are seen to exist with sea and lake breezes, it is appropriate to investigate the effects of surface properties and clouds in some detail. Previous observational studies have not considered the effects of prevailing surface and cloud conditions on sea and lake breezes. Previous theoretical studies prescribed the time variation of surface heating. These arbitrary formulations do not permit the circulation to interact with the land surface and modify its temperature. A heat budget formulation will allow the surface temperature to evolve naturally in response to the radiation fluxes, surface sensible and latent heat fluxes, cloud effects, and atmospheric structure.

The principal objective of this study is to analyze the effects of horizontal and time variations of land surface heating on the sea breeze. These heating variations result from spatial and temporal variations in surface and cloud properties. This objective is attained through the use of observations and numerical modeling. The observed or deduced values of albedo, thermal inertia, soil moisture, and clouds form the basis for data input to the model.

Observations are studied to evaluate the actual surface temperature response to incoming and outgoing radiation, clouds, soil moisture, and rainfall. Important questions considered are: What are the observed distributions of surface properties in the area selected for numerical simulation? What is the albedo profile across the study

area? What is the magnitude and range of thermal inertia deduced from the albedo and surface temperature observations? How do cloud cover, soil moisture, and sudden rain affect observed surface temperature? With this information, realistic values of surface properties and clouds are prescribed in numerical sensitivity and case study experiments.

The numerical model is used to study surface and atmospheric responses to specified changes in the magnitude and distribution of surface and cloud properties. Results from numerical experiments using a surface heat budget formulation are compared against those from a sinusoidal heating function.

The modeling is done in two experimental modes. The first mode consists of sensitivity experiments with hypothetically specified values and spatial distributions of surface and cloud properties. Answers are sought for the following questions: What are the major differences between the heat budget model results and those from the sinusoidal heating function? What is the relative importance of the different soil properties and cirrus clouds in determining surface heating and sea breeze response? What changes in surface heating and sea breeze evolution occur when the scale of horizontal heating variations that results from surface properties and clouds is altered in a systematic fashion? What changes result when the scale and magnitude vary simultaneously?

The second experimental mode consists of a case study of a sea breeze that occurred over South Florida on a given day. This case study is a special sensitivity experiment. On this day, surface properties and cumulus cloud cover were observed or deduced in some detail. This information constitutes the data input to the model. Answers are sought for the following questions: What is the relative importance of surface properties and clouds in establishing the intensity and movement of the sea breeze? What is the degree of realism that can be attained through numerical simulation of this sea breeze event in which observed or deduced surface and cloud properties form the data base for the model?

1.6 Summary

The sea breeze originates as a result of differential heating between land and water. The fields of heat, mass, and moisture associated with sea breeze convergence zones are important for subsequent convection. This fact provides the incentive for this study. The degree to which these fields are organized and the location of these fields is influenced by the patterns of surface heating over

Florida. These patterns change because of variations in surface albedo, thermal inertia, soil moisture, and cloud cover. These properties are rarely measured and few observational and theoretical studies of lake and sea breezes have considered their influence. This study evaluates the influence of surface properties and clouds on the South Florida sea breeze with a variety of numerical sensitivity experiments and a case study.

2. PHYSICAL PROPERTIES OF THE SURFACE

As it is held that a knowledge of surface albedo, thermal inertia, and soil moisture is essential for the proper understanding and prediction of variations in sea breeze behavior, this section describes those properties in some detail. A discussion of cloud effects on the incoming and outgoing short- and long-wave radiation fluxes is deferred until Sections 4, 5, and 6.

This section provides the physical definition of the surface properties and their relation to each other and the surface heat budget. Some discussion is devoted to the techniques and difficulties involved in observing or deducing these quantities.

2.1 Surface Albedo

The albedo is here defined as the ratio of the incoming direct and diffuse solar radiation that is reflected by the surface to the total incident. As

the radiation that is reflected increases with solar zenith angle, the influence of this angular dependence must be specified. The modification factors (table 1) chosen to account for this angular dependence are based upon those of Kondratyev (1969). The albedo is calculated after all atmospheric absorption, scattering, and reflection processes are completed. The shortwave radiation not reflected is that component which enters into the surface heat budget formulation.

Not only does the albedo change with solar zenith angle, but it varies over a moderate range depending upon the amount of soil moisture in the upper centimeter of soil. Figure 1 from Idso (1975) shows the variation of albedo with soil moisture for a given soil type. Black peat organic soils, such as those found in the Florida Everglades and the agricultural region south of Lake Okeechobee, undergo a decrease in albedo from 14% to 7% after wetting. Soils that decrease in albedo after wetting could experience higher daytime temperatures if their moisture release characteristics were limited.

It is shown in Section 6 that changes in surface albedo produce significant changes in sea breeze intensity. These changes occur as a result of increased sensible heat flux to the atmosphere. This effect should be considered in planning for large-scale alteration of the surface. For example, removal of vegetation from a region with low albedo soils could result in a more intense sea breeze. Alternatively, use of construction materials with high albedos may reduce metropolitan sensible heat input and the sea breeze. It has been observed that the three surface properties are interdependent.

Table 1.
Surface albedo modification factors

Morning		Afternoon	
Solar zenith angle (degrees)	Modification factor	Solar zenith angle (degrees)	Modification factor
91-75	1.744	0-2	1.00
75-68	1.55	2-8	1.01
68-62	1.46	8-14	1.01
62-55	1.30	14-22	1.01
55-48	1.21	22-28	1.02
48-42	1.17	28-35	1.03
42-35	1.13	35-42	1.04
35-28	1.09	42-48	1.08
28-22	1.05	48-55	1.10
22-14	1.02	55-62	1.16
14-8	1.015	62-68	1.24
8-2	1.01	68-75	1.35
2-0	1.00	75-91	1.47

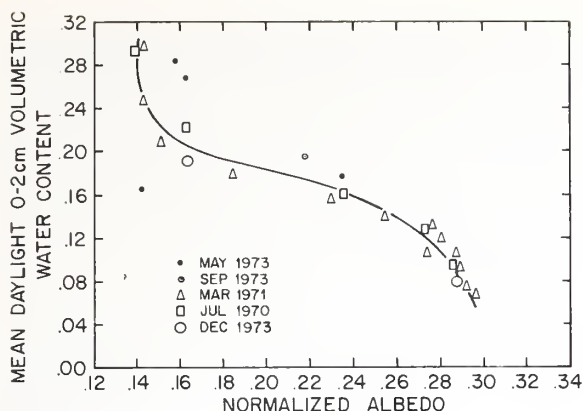


Figure 1. Variation of soil albedo (horizontal axis) with soil moisture (cm^3/cm^3) in the upper 2 cm (vertical axis) for a given soil type. (Idso, 1975, Fig. 8, p. 120, with permission)

2.2 Thermal Inertia

Thermal inertia is defined

$$TI = (K\rho_s C_s)^{1/2} \quad (\text{cal s}^{-1/2} \text{ cm}^{-2} \text{ }^\circ\text{C}^{-1})$$

where K is thermal conductivity ($\text{cal cm}^{-1} \text{ s}^{-1} \text{ }^\circ\text{C}^{-1}$),
 ρ_s is soil density (g cm^{-3}),
 and C_s is soil specific heat ($\text{cal g}^{-1} \text{ }^\circ\text{C}^{-1}$).

Thermal inertia is a quantitative measure of the resistance of a material to a change in temperature. In the case of the surface, the variation in ground surface temperature depends on the value of this property, while the subsurface temperature profile depends on both conductivity (or diffusivity) and density (Kahle et al., 1975). Although thermal inertia cannot be measured directly by remote sensing, it can be deduced from a knowledge of the noon versus midnight temperature difference and the surface albedo, but only for near-dry surfaces. It can also be calculated under certain conditions. Water, wet soils, and moist vegetation have high thermal inertias (0.2 to 0.6). Sand, rocks, dry soils, and building materials have characteristically low thermal inertias (0.04 to 0.10). The top few centimeters of the ground react to the net energy flux in such a way that this single thermal parameter, together with the heat budget components of evaporation, sensible heat, short-wave radiation, and net infrared radiation, describes the air-ground boundary temperature.

A major advantage in employing a heat budget equation with this single thermal parameter is the simplicity with which the surface temperature

is calculated. The heat budget equation employed in the model to calculate surface temperature T is

$$T = T_0 + \frac{2F_n}{TI} \left(\frac{\Delta t}{\pi} \right)^{1/2}. \quad (1)$$

T_0 is the initial temperature (kelvin), F_n is the net energy flux ($\text{cal cm}^{-2} \text{ s}^{-1}$) across the air-ground interface, TI is the thermal inertia ($\text{cal s}^{-1/2} \text{ cm}^{-2} \text{ }^\circ\text{C}^{-1}$), and Δt is the time step (seconds). More is said about the surface heat budget formulation in Section 5.7.

The thermal inertia includes the effect of heat flux into the ground, and it is not required that the vertical profile of flux beneath the surface be calculated. The alternative is to numerically solve the heat conduction equation

$$\frac{\partial T}{\partial t} = \frac{\partial}{\partial z} \left(K \frac{\partial T}{\partial z} \right)$$

in a soil layer for depths of about 50 cm together with an energy balance equation that defines the equilibrium temperature at the surface. See, for example, Estoque (1973). The quantity K ($\text{cm}^2 \text{ s}^{-1}$) is the soil diffusivity or thermometric conductivity. That the solution of this equation requires considerable computer time and core storage is one reason for using equation (1).

The choice of the thermal inertia formulation is in line with the practical orientation of this study; we wish to show the importance of those surface properties for which some capability exists or will exist for determining their values. In the next decade, high-resolution, high-frequency satellite observations of surface soil temperature, soil moisture, and albedo should be routinely available. No capability exists, or is forecast to exist, where subsurface thermal properties will be directly determined. Currently, the thermal inertia can be deduced from conventional satellite (or aircraft) temperature and albedo data under certain conditions and for certain regions.

Pohn et al. (1974) investigated the interrelationships among the day-versus-night (near-noon minus near-midnight) surface temperature difference (ΔT), albedo, emissivity, thermal inertia, and elevation of the ground. It was found that ΔT was reasonably independent of elevation and emissivity, moderately dependent on albedo, and strongly dependent on thermal inertia. Figure 2 shows the empirical set of curves that were derived from their investigation. The curves are valid for a latitude strip running from 22°N to 25°N and for a solar declination angle corresponding to mid-May.

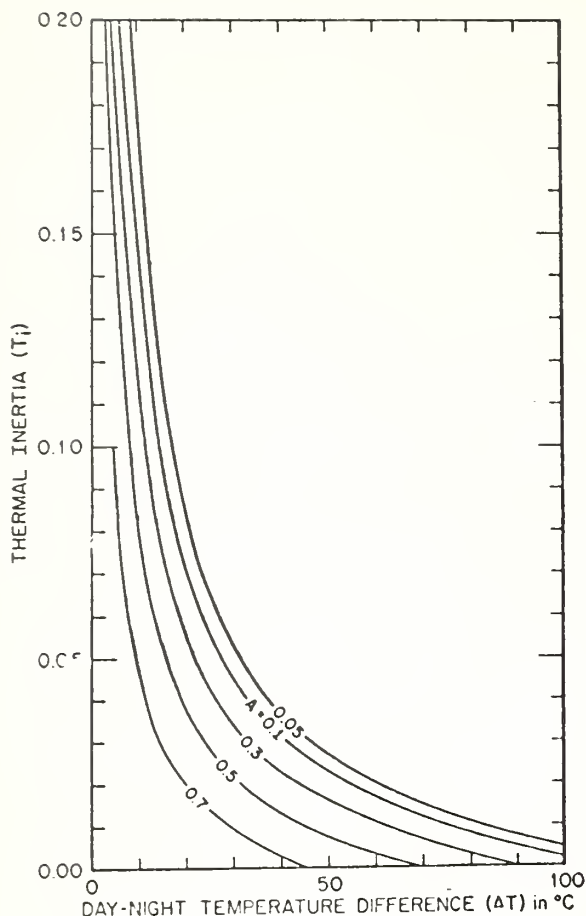


Figure 2. Surface albedo (A) as a function of thermal inertia (T_i) and day-night temperature difference (ΔT). (From Pohn et al., 1974.)

It is important to note that in the construction of figure 2, soil moisture and sensible heat fluxes were not considered in the computer-generated diurnal temperature curves for the site (Oman) in question (Pohn et al., 1974). Under stable, arid conditions and light winds, turbulent transfer of latent and sensible heat should be negligible factors in determining ΔT . Under these conditions, only solar radiation, downward atmospheric radiation, and thermal emission of the surface are important. As surface moisture increases, thermal inertia increases. Watson (1975) points out that the addition of moisture to a dry soil results in a much larger increase in thermal inertia than should be expected for the increase in soil density. Idso (1975) demonstrates this effect for several soil types. The specific heat and the conductivity also increase as soil moisture increases. There is an upper limit to the thermal inertia that various

saturated soils can attain. Thus, rocks and soils have a much smaller contrast in thermal inertia when they are wet (Watson et al., 1971). The reverse is noted in the case of surface albedo. Rocks and soils show a marked decrease in albedo when they are wetted (Idso et al., 1975; Coulson and Reynolds, 1971). This decrease partially compensates for the increased thermal inertia.

As soil moisture increases, the utility of figure 2 diminishes. The diurnal temperature range is increasingly dependent upon the evapotranspiration. The increase in thermal inertia resulting from moist soil is, in general, minor compared with the cooling associated with evapotranspiration. This is verified through numerical simulations with the model (to be discussed). At values of soil moisture approaching saturation, variations in thermal inertia over a moderate range do not result in significant differences of surface temperature or atmospheric motions. Similar findings were reported by Idso et al. (1975). They found that the differences between net radiation and soil heat flux in saturated soil was almost twice that for soil at near-dry conditions. These observations can be explained by the large decrease in net flux into the ground which occurs when evaporation is high. These observations also imply that errors in estimating thermal inertia are not serious when soil moisture contents are high.

An alternative procedure for estimating thermal inertia consists of solving for this quantity using (1). During early morning periods (e.g., 0300 EDT to 0600 EDT), when clear skies and light winds prevail, only upward surface radiation and downward atmospheric infrared radiation are important. Fluxes are most likely to be constant over this period, and, if the initial and final surface temperatures and fluxes are known or estimated, the thermal inertia can be calculated.

In summary, thermal inertia and evaporation increase (decrease) with the addition (removal) of moisture. The relationship would have to be defined separately for each type of soil. The set of surface relative humidity versus volumetric moisture content curves presented by Nappo (1975) provides a good example for the evapotranspiration case.

2.3 Soil Moisture

Soil moisture is the dominant physical property controlling ground surface heating; it does this primarily through the evapotranspiration process and secondarily through its influence on thermal inertia and albedo. The evapotranspiration process dominates through the cooling it

produces at the air-ground interface. With high values of soil moisture, a large fraction of the net flux is used to convert soil water into vapor at the air-ground interface (or at the leaf surface of vegetation) instead of passing into the soil and increasing surface temperature. The increase of thermal inertia with increased soil moisture is a linear process (Idso et al., 1975). Some compensation in the surface heating profile occurs with decreased albedo which accompanies increased soil moisture.

The importance of soil moisture in boundary layer processes has been stated by Philip (1957) and others during the past 25 years. Tag (1969) performed numerical experiments in which albedo, diffusivity, and soil moisture were allowed to vary somewhat linearly between a typical city and the surrounding countryside. He reaffirmed that soil moisture is dominant in reducing the amplitude of the diurnal temperature wave in the country. Approximately 60% of all relevant publications dealing with soil moisture have appeared during the past decade (Monteith, 1975). Thorough treatment of the subject of soil moisture as it relates to bare and vegetated surfaces and its impact on atmospheric processes is beyond the scope of this work. Here, an attempt is made to synthesize the principal processes.

Basic soil moisture retention, drainage, and evaporation characteristics can be classified by soil texture (Salter and Williams, 1965). Soil texture classes range from coarse sands through fine loams and silts to very fine-particled clays. Organic (nonmineral) soils, such as peats and mucks, exhibit the maximum water retention capability. Over South Florida, soil texture varies over almost the entire range from the sandy coastal regions to the muck-dominated interior. Figure 3, from Yong and Warkentin (1975), shows the standard U. S. Department of Agriculture triangle in which mineral soils are defined based upon the sand, silt, and clay components. Sands drain quickly and have a low available water capacity (Monteith, 1975). However, even at low moisture contents existing before complete loss of water, moisture just below the surface can be transformed to vapor for evaporation quite easily (Nappo, 1975; Monteith, 1975). Studies show a predictable increase in available water with decreasing grain size. Therefore, the clays, and especially muck soils, drain slowly and retain more water, but are unable, because of capillary forces, surface forces, etc., to release the water for vertical movement in spite of higher soil-water potential values. Typical water retention curves from Yong and Warkentin (1975) are shown in figure 3.

In bare soils, water budgeting must consider rainfall, drainage (hydraulic conductivity), and evaporation of that water retained against

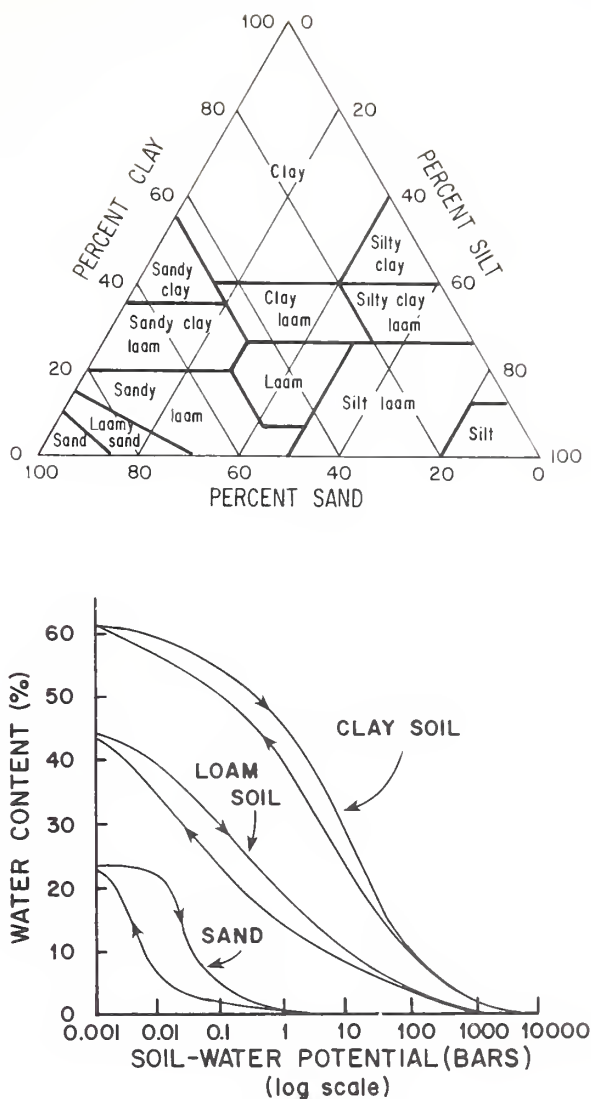


Figure 3. Charts of soil properties (from Yong and Warkentin, 1975, Figs. 1.2 and 4.8). Above: U. S. Department of Agriculture Soil Triangle showing percent clay, silt, and sand in the soil textural classes. Below: Representative water-retention curve showing relationship between potential and content for different soils. (Courtesy of authors and publisher.)

gravity. A typical drainage curve for finely textured Florida sand is shown in figure 4.

Drainage (hydraulic conductivity) is most rapid in sandy soils and is 2 to 3 orders of magnitude slower in organic or clay soils. As the amount of water left for drainage decreases, the drainage rate decreases (van Bavel et al., 1968; Monteith, 1975). In the top few centimeters of bare soil, that water which is not drained is available for evaporation.

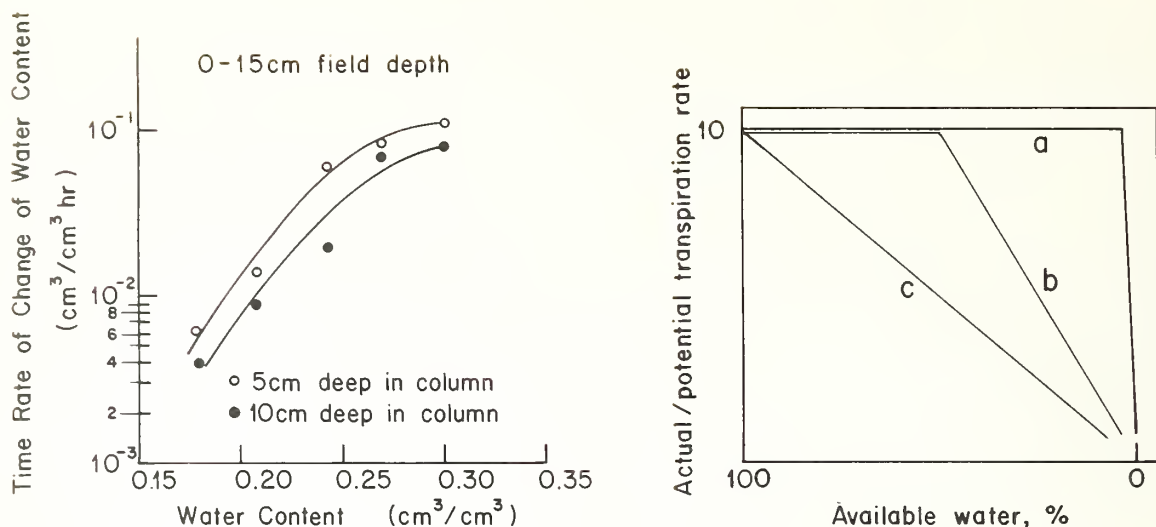


Figure 4. Soil property charts. Left: Drainage curve for finely textured Florida sand (Elzeftawy and Mansell, 1975). The abscissa is water content in cm^3/cm^3 , and the ordinate is time rate of change of water content in cm^3/cm^3 per hour. (Reproduced from *Soil Science Society of America Proceedings*, Vol. 39, Jul-Aug 1975, No. 4, p. 603, by permission of the Soil Science Society of America.) Right: Schematic diagram showing shape of the three general evaporation profiles (Monteith, 1975, Vol. 1, p. 147). The abscissa is available water (%), and the ordinate is the ratio of the actual to the potential transpiration rate. (With permission, from *Vegetation and the Atmosphere*, copyright by Academic Press, Inc. (London) Ltd.)

That point at which the evapotranspiration rate becomes less than the maximum possible (potential evapotranspiration rate) is dependent upon a wide variety of climatic, plant, and soil factors.

The complications arising from vegetation are formidable. As van Bavel et al. (1968) show, with any root system, consumptive use by the plants can induce a reverse (upward) flux by water in the vicinity of the root zone. In this case, with soil moisture between field capacity and the wilting percentage (Salter and Williams, 1965), the evapotranspiration is at its maximum value for a longer period than for the similarly wetted bare soil. Only evapotranspiration profiles with vegetation on a sandy base show little change from the bare soil case (Holmes and Robertson, 1963).

The question of evaporative water loss in conjunction with vegetated surfaces is not a trivial one. With the stripping away of vegetation, an important moisture source for the atmosphere is severely capped and the surface is exposed to greater heating. This removal of transpiring surfaces should then have a measurable influence on sea breeze boundary layer temperature structure. If, as Sutton (1953) states, Porton, in southern England, can experience temperatures of 60°C on macadam, 55°C on sand, and 44°C for a grass-covered surface, then little imagination is required to visualize the temperature changes in the tropics which would result from replacing vegetated surfaces with artificial substances.

For the case study experiment, it is assumed that vegetated and bare soil regions can be treated the same in the water-budgeting method used to determine soil moisture. Only rainfall, drainage, and evaporation are considered. It is recognized that a reverse upward flux can occur in the case of vegetation (van Bavel et al., 1968), yet even this process can be modified in the tropics. It has been found that with saturated soils, plants (including sugarcane) can lose water faster than it is replaced by the root system (Gooding, 1972).

The procedures used to determine soil moisture for the given case-study day are discussed in Section 6. Experimental results showing the effects of soil moisture are also given in Section 6. The time history of soil moisture for selected soil types is discussed in Appendix C.

2.4 Summary

The surface albedo is seen to affect the net short-wave radiation flux that enters the topmost surface layers. As shown in figure 2, albedo is also necessary to determine the thermal inertia of the surface. This latter quantity describes the resistance to heating of the topmost few centimeters of the ground. Its use in the appropriate heat balance equation simplifies the computation of the boundary temperature of the air-ground interface. Soil moisture is the most important surface property and exercises a major control over the diurnal

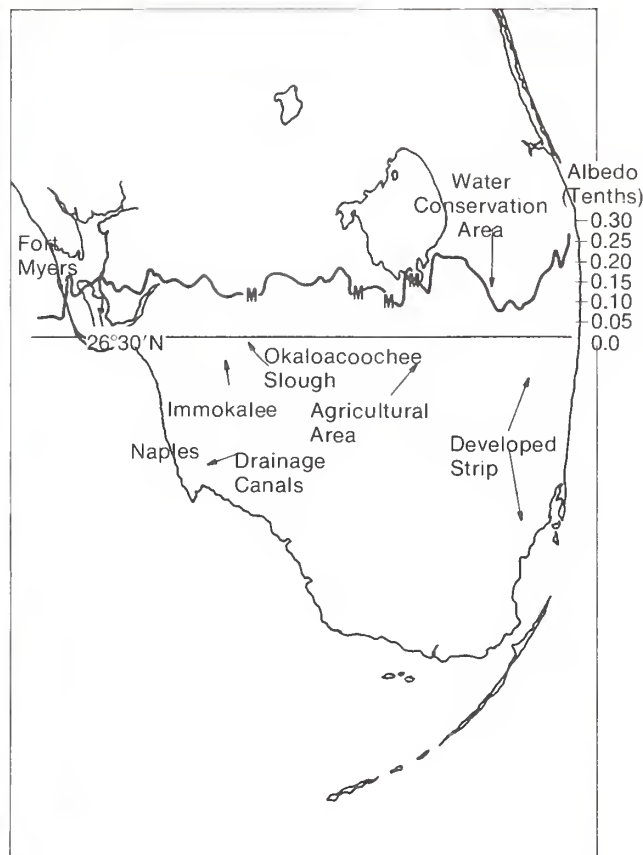
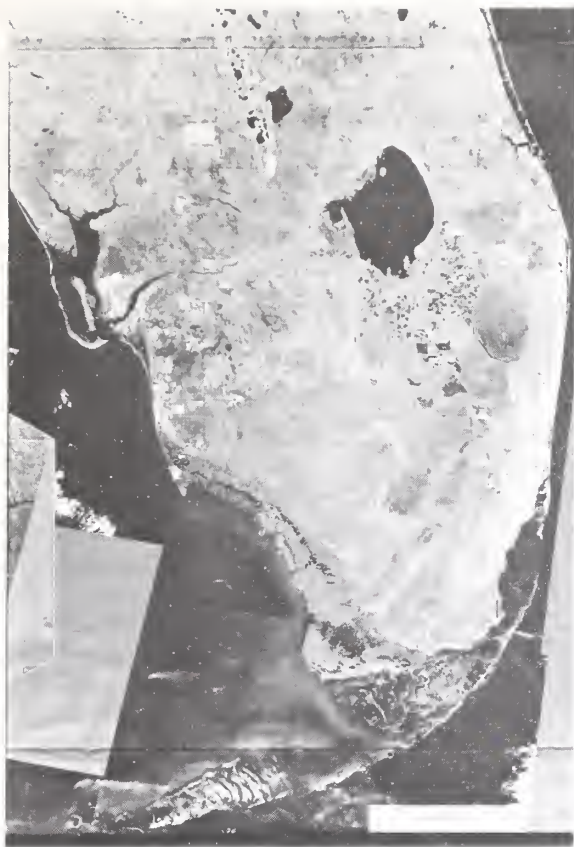


Figure 5. LANDSAT-1 false-color composite mosaic (1975) of South Florida with overlay which identifies well-defined topographical features and albedo profile across Florida at 26°30'N. Profile was obtained from NCAR Queen Air research aircraft on July 16, 1975.

temperature range through control of the evapo-transpiration component. The addition of moisture to soil results in an increase in thermal inertia and a decrease in albedo. Soil moisture determination in bare soils is complicated, but even more so in the case of vegetated surfaces. Vegetation transpires in response to a complex array of factors. The determination of soil moisture conditions for modeling and forecasting purposes should be given high priority.

3. STUDY AREA

The study area consists of an east-west oriented, 11-km-wide strip centered along 26°30'N across Florida. This area was chosen because it crosses the meteorological surface network established by the National Oceanic and Atmospheric Administration (NOAA) in conjunction with the Florida Area Cumulus Experiment (FACE) of 1975. (The data from the network are used to validate numerical results from model runs. Sec-

tion 4 treats the subject of data acquisition in detail.) The study area is interesting for the many inhomogeneities that are encountered along it.

3.1 Physical Features of Study Area

Figure 5, a false-color LANDSAT photo composited of imagery from four spectral bands in the visible and near-infrared, shows the experimental cross section. A narrow, populated strip, approximately 11-km wide, characterizes the eastern coastal portion. West of this strip lies the Loxahatchee National Wildlife Refuge, also known as Water Conservation Area Number One. This body of water, partially covered by vegetation, exerts a significant influence on cumulus and mesoscale processes in its vicinity. The effects are similar to, but smaller in scale than, those associated with Lake Okeechobee. The most pronounced effect is the development of divergent flow over this water body on a normal sea breeze day. The result is a relatively cloud-free air mass over the water.

West of the water conservation area is a large region devoted primarily to cultivation of sugar cane. This region was once the original marsh of the Everglades. The black rectangular plots are bare, black muck soils. The lighter areas are planted largely with sugar cane. A seasonal change in planting results in changes of surface albedo with time. The black muck has an albedo of about 5%, while the sugar cane reflects up to 20% of the incoming solar energy (Gooding, 1972). It is considered significant that drying of the Everglades black peat muck can increase its albedo to 14%. This area is also subjected to controlled irrigation, as well as drainage, making soil moisture determination extremely difficult. West of the agricultural area is a well-drained, sandy region dominated by pine, palmetto, and cypress.

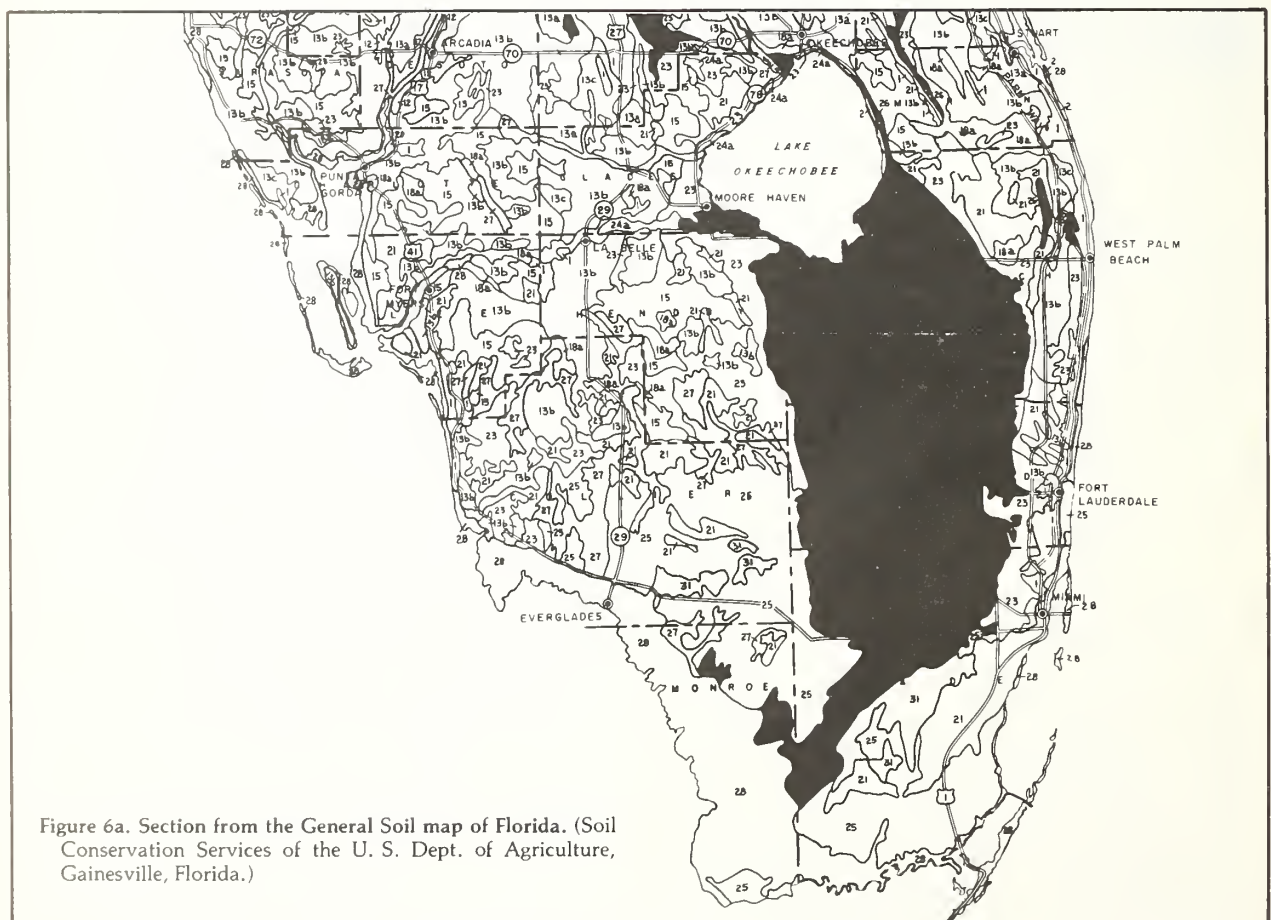
The large, swampy region southwest of Lake Okeechobee is the Okaloacoochee Slough. This water body expands noticeably during the South Florida summer as it is the natural basin for water draining from the sandy areas surrounding it. West of the slough, the Immokalee area is characterized by pine and palmetto scrub growing on a sandy base. The elevation is slightly higher here.

The sand-dominated areas exhibit different thermal properties and heating patterns than the sugar cane growing region south of Lake Okeechobee. The quick drainage characteristics of the sandy soils generally permit more rapid drying and more intense heating than would occur for muck soils.

A complicated mix of swamp and poorly drained sands dominates the remainder of the region to the west coast. Explosive population growth (42% in 1975) promises radical coastal alteration of the region surrounding Fort Myers, Florida. The effects of urbanization can be seen in figure 5 near Fort Myers and northeast of Naples, where streets and drainage canals are visible.

3.2 Soil and Vegetation Profiles

Figure 6 shows soils of South Florida; figure 7 shows the natural vegetation. With urbanization, land drainage, water conservation measures, flood control, and introduction of exotic foreign vegetation, the patterns shown in figures 6 and 7 have been altered radically in the past two decades.



3.3 Summary

The study area across Florida at 26°30'N was chosen on the basis of the availability of meteorological data from the NOAA FACE 1975 experiment. As the study area possesses a wide variety of surface features, it is ideally suited for the purposes of this investigation.

AREAS DOMINATED BY EXCESSIVELY DRAINED SOILS

Soils dominantly thick acid sands

- 1 St. Lucie — Lakewood — Pomello association

Soils dominantly thick neutral to alkaline sands

- 2 Palm Beach — Cocoa association

AREAS DOMINATED BY WELL DRAINED TO MODERATELY WELL DRAINED SOILS

Soils dominantly thick to moderately thick acid sands

- 3 Lakeland — Eustis — Blanton association
3a Lakeland — Eustis — Norfolk association

Soils dominantly thick to thin sands influenced by alkaline materials

- 4 Jonesville — Chiefland — Hernando association
9 Hernando — Chiefland — Jonesville association

Soils dominantly thick to thin phosphatic sands and loamy sands overlying finer-textured materials

- 5 Arredondo — Gainesville — Fort Meade association
8 Hague — Zuber — Fellowship association

Soils dominantly thin acid sand to sandy loam overlying finer-textured subsoils

- 6 Norfolk — Ruston — Orangeburg association
7 Magnolia — Faceville — Tifton association
10 Shubuta — Cuthbert — Lakeland association
11 Kalmia — Cahaba association

Soils dominantly thick to thin acid sands, some of which overlie finer-textured subsoils

- 12 Blanton — Klej association
12b Kanapaha — Blanton association
17a Rex — Blanton association
17b Blanton — Bowie — Susquehanna association
17c Goldsboro — Lynchburg association

AREAS DOMINATED BY SOMEWHAT POORLY DRAINED SOILS

Soils dominantly thick acid sands with organic pans; interspersed with soils without a pan formation

- 13a Leon — Plummer — Rutlege association
13b Leon — Immokalee — Pompano association
13c Leon — Pomello — Plummer association
13d Leon — Blanton — Plummer association

Soils dominantly thick acid sands with dark surface soils

- 14 Scranton — Ona association

Soils dominantly thick to thin sands overlying finer-textured alkaline materials

- 15 Adamsville — Pompano association
18a Sunniland — Bradenton association
18b Panasoffkee — Bushnell association
21 Broward — Parkwood — Keri association

AREAS DOMINATED BY POORLY TO VERY POORLY DRAINED SOILS

Soils dominantly thick to thin sand to sandy loam surface soils overlying finer-textured acid subsoils

- 19 Coxville — Bladen — Weston association
20 Leaf — Bladen — Rains association
22 Plummer — Rutlege association
24b Bayboro — Portsmouth — Rains association

Soils dominantly moderately thick to thin sands to sandy loams overlying finer-textured alkaline materials

- 23 Pompano — Charlotte — Delray association
24a Manatee — Felda association

Soils dominantly moderately thick to thin marly materials overlying limestone

- 25 Perrine — Ochopee association

Soils dominantly peats and mucks

- 26 Everglades — Brighton — Pamlico association

MISCELLANEOUS LAND TYPES

- 27 Fresh Water Swamp — Marsh
28 Tidal Marsh — Coastal Beach — Coastal Dunes
31 Rockland

Figure 6b. Florida soils indicated in Fig. 6a.



Figure 7a. Section from the General Map of Natural Vegetation of Florida. (Dade County Agricultural Agent's Office, Homestead, Florida.)

- 1 Coastal strand. A zoned vegetation on sand dunes and rock, composed of pioneer herbs and shrubs near shore with scrub and forest zone more interior. The strand of the Florida Keys has many tropical forests and scrub.
- 2 Pine Flatwoods. Open woodlands of one to three species of pine: longleaf, slash, and pond pines. Many herbs, saw palmetto, shrubs and small trees form an understory. Included in general flatwoods areas are small hardwood forests, many kinds of cypress swamps, prairies, marshes, and bay tree swamps.
- 3 Southern Slash Pine Forests. Open woodlands of *Pinus elliottii densa*, mostly on rocklands. Some herbs, shrubs, and hardwood trees of understory are tropical. Small tropical and subtropical hammock forest areas are included.
- 4 Forests of Mixed Hardwoods and Pines. Mostly on uplands of clay soils in northwest section. Many differences in composition and age; some young second growth is mostly pines. The more mature forests are mostly hardwoods.
- 5 Sand Pine, *Pinus clausa*, Scrub Forests. Mostly on excessively drained deep sandy soils. These occur on old dunes of #1, and on old dunes or dry sands in the interior.
- 6 Forests of Longleaf Pine, *Pinus palustris*, and Xerophytic (dry site) Oaks. Mostly on well drained uplands. The turkey oak, *Quercus laevis*, and wire grass, *Aristida stricta*, are common. Many former areas of this type are now citrus groves in the central section.
- 7 Cypress Swamp Forests. Mostly in depressions and bordering rivers and lakes. Forests of many shapes, as round domes and long strands. Some have hardwood species associated. Cypress is also common in #2 and #8, and a scrub form in #14.
- 8 Swamp Forests, mostly of Hardwoods. Several kinds bordering most rivers and in basins. Some Bay Tree, Gum, *Nyssa*. Titi and cypress zones occur in many of these hardwood swamps.
- 9 Mangrove Swamp Forests and Coastal Marshes. Usually there are tidal conditions which vary from saline to brackish. Tropical mangrove forests in southern area; and grass, sedge, and rush marshes along more temperate coasts.
- 12 Hardwood Forests. Mostly on rich soil uplands. These are mixed evergreen and deciduous hardwoods. Some areas are nearly original hardwood stands but many are old second growth with pines.
- 13 Grasslands of Prairie Type. Wet Prairies on seasonally flooded lowlands. Dry Prairies on seldom flooded flatlands. Many former areas of these are now improved pastures.
- 14 Region of open Scrub Cypress. Mostly on rock and marl soils that are often flooded. Small areas in this region are tall domes and strands. Also there are some hardwood and palm hammocks.
- 15 Forests of abundant Cabbage Palms, *Sabal palmetto*. Vary from scattered palms to groves of palms and oaks in hammocks. Cabbage palms are also abundant in #2, #3, #8, #13, #14, and #17.
- 16 Fresh Water Marshes. Some are mixed marshes of many kinds of herbs and bushes, and some are dominated by one plant, such as the Saw Grass Marshes, mainly of *Mariscus jamaicensis*.
- 16a Everglades Region Saw Grass Marshes. Area mostly dense to sparse saw grass, a few tree islands and sloughs.
- 16b Everglades Region Marshes, Sloughs, Wet Prairies, and Tree Islands. The tree islands vary from Bay Tree type to Tropical Hardwoods. Region now changing.
- 17 Wet to Dry Prairie-Marshes on Marl and Rockland. Some are mostly thin saw grass, others are bushes and grasses.
- w Water Areas. Only a few of the thousands of lakes and ponds are shown. These and rivers are habitats for abundant aquatic plants.

Figure 7b. Florida vegetation indicated in Fig. 7a.

4. OBSERVATIONS TO SUPPORT THEORETICAL MODEL

Certain special observations were taken in support of this investigation. The data acquisition devices were emplaced in the NOAA FACE 1975 mesonetwork with the cooperation of NOAA personnel supporting the FACE 1975 cloud seeding program. Other observations that were gathered in support of FACE 1975 were also made available for this study.

This section discusses the data acquisition systems and the measurements of surface albedo, solar radiation, evaporation, and land and water surface temperature. From these data, some representative values of thermal inertia are deduced. Soil moisture was not observed during the FACE 1975 experiment, but some inferences concerning temporal changes in this quantity are made from observations of rainfall and evaporation. The discussion of procedures for determining soil moisture for use in a case study experiment is deferred until Section 6.

4.1 Systems Employed for Data Acquisition

The FACE 1975 observational mesonetwork is shown in figure 8. The FACE 1975 surface mesonetwork consisted of a variety of recording instruments, including devices for measuring wind, rainfall, soil and air temperature, and incoming solar radiation. In addition, a variety of surface and aerial photos were taken. The cross-peninsula section shown in figure 5 runs from east to west just south of the Field Observing Site (FOS) which is shown in figure 8. Most of the network is in the sugar cane and irrigation canal complex south of Lake Okeechobee.

The C-130 and DC-6 aircraft of the Miami-based NOAA Research Flight Center were used to gather high quality data related to this study. In addition to conducting randomized seeding experiments and making cloud microphysical measurements, NOAA aircraft measured the surface infrared signature along the cross section with a Barnes PRT-5 infrared radiometer. Most of the surface temperature data derived from the radiometer readings were gathered on 15 early afternoon runs during July 1975; however, one special night flight was made in an effort to determine a representative day-versus-night surface temperature difference.

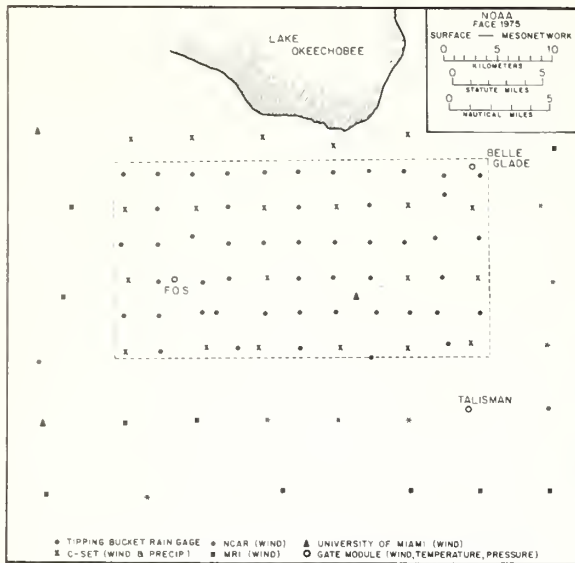


Figure 8. FACE 1975 observational mesonet network.

As an integral portion of the total FACE 1975 data base, high-resolution, high-frequency visible and infrared data from the Synchronous Meteorological Satellite (SMS-1) were collected. Through the assistance of the Miami-based National Environmental Satellite Service (NESS) Field Services Station and the Cumulus Group of the National Hurricane and Experimental Meteorology Laboratory, visible and infrared imagery were provided on many days at 30-min intervals from dawn to dusk.

The surface measurements of primary relevance to this program were derived from soil and water temperature sensors, whole-sky cameras, and an Eppley upward-facing pyranometer. The three observing platforms used to collect data were located at FOS, the Belle Glade Agricultural Experiment Station, and the Talisman site. The platforms were NOAA-built, self-contained data collection modules which were used in the 1974 GATE experiment on oceanographic research vessels. Figure 9 shows the GATE module at FOS. The three modules were equipped to record soil temperature from two probes. The modules also digitally recorded air temperature, pressure, wind speed, and wind direction. Whole-sky color photos were taken every 10 min during daylight hours from July 22, 1975, to September 15, 1975. During this same period, the Talisman site recorded incoming direct and diffuse solar radiation each minute. Table 2 lists the sensors of primary relevance to this project.

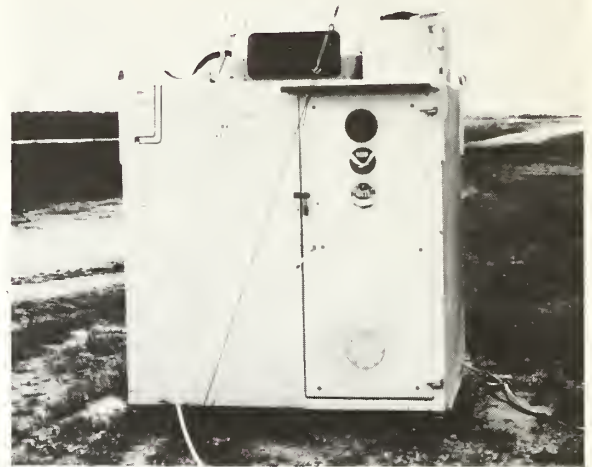


Figure 9. GATE module at the field observation site.

Surface mesonet measurements of rainfall and wind were used in conjunction with case study experiments reported in Section 6. The locations of the devices used to record these elements are shown in figure 8. Rain gage measurements were used to adjust the National Weather Service, Miami, WSR-57 weather radar rainfall estimates used in water balance computations for soil moisture. The results of the case study experiment were validated with the wind values.

4.2 Albedo of the Surface

Short-wave radiation devices on the NCAR Queen Air research aircraft were used for measuring albedo across $26^{\circ}30'N$. With the upward-facing and downward-facing pyranometers, albedo profiles for various cloud-free flight paths were obtained for July 16, 1975. An almost cloud-free east-west pass was made from 1134 EST to 1209 EST on this day. The albedo profile is displayed in figure 5, Section 3.1, so that general comparisons with surface features can be made. An albedo value of 5% was noted for the Atlantic Ocean and Gulf of Mexico. Note the high values (20%–25%) over the sand and developed areas between the Atlantic Ocean and the reservoir. Values over the reservoir are low (7%–10%), as would be expected for a water surface with some vegetation. The albedo rises abruptly (20%) over the pasture

Table 2.
Sensor data from FACE 1975 mesonetwork

Sensor	Field location	Parameter	Location of sensor	Period of observation	Sampling frequency
Eppley pyranometer	Talisman site (H-12)	Incoming direct and diffuse short wave rad.	Top of module	7/21 to 9/15	Every minute
Whole-sky camera	Talisman site (H-12)	All-sky color photos	Top of module	7/22 to 9/15	Every 10 minutes
	Field observation site (FOS)			8/1 to 9/15	
Soil surface temperature probe	Belle Glade Agric. Experimental Station (A-12)	Water surface temperature	0.5-cm depth in 2-3 ft deep stagnant canal	7/21 to 9/15	Every minute
		Soil surface temperature	0.5-cm depth in black muck with 16-inch grass cover		Every minute
Soil surface temperature probe	Talisman site	Soil surface temperature	0.5-cm depth in black muck	7/21 to 9/15	Every minute
Soil surface temperature probe	Talisman site	Soil surface temperature	0.5-cm depth in black muck with tall grass cover	7/21 to 9/15	Every minute
Soil surface temperature probe	Field observation site	Soil surface temperature	0.5-cm depth in light sandy soil	7/21 to 9/15	Every minute
		Soil surface temperature	0.5-cm depth in light sandy soil with sparse weed cover		Every minute

area just west of the reservoir. Note the erratic nature of the profile in the agricultural area south of Lake Okeechobee. The low values (8%–12%) correspond to uncultivated black organic peat soils, and the relatively high values (13%–17%) correlate with sugar cane in various stages of growth. As in Barbados (Gooding, 1972), the albedos for cane range from 12% to 19%, depending upon stage of growth. The increase in albedo (approximately 15%) from the agricultural area to the Okaloachoochee Slough results from a mix of sandy soil and vegetation. The Slough has low values (10%), while the sandy ridge just west of it shows an increase to 15%. The albedo profile from there westward is fairly homogeneous (15%–17%) and typical of a moderately vegetated surface. Maxima in the profile are noted for the developed strip south of Fort Myers and the beaches. These albedo values over Florida correspond remarkably well in the general sense with those found by Kung et al. (1964).

4.3 Solar Radiation

Figure 10 shows the short-wave radiation and corresponding soil temperature record for July 29, July 31, August 1, and August 2, 1975. The radiation record was obtained with an Eppley pyranometer at the Talisman site. This annotated example shows the influence of clouds and rainfall on the incoming direct and diffuse solar radiation and soil surface temperature. Solar radiation is given in langley (Ly) per minute. One langley is one cal cm^{-2} . Although surface temperature is a subject treated separately in Section 4.6, the temperature record is included here as an example of the direct response of soil surface temperature to the solar beam as it is, in turn, affected by clouds, rainfall, and variable atmospheric moisture content. The soil temperature probe in this instance is buried 0.5 cm deep in black Everglades peat muck. The surface temperature is seen to respond

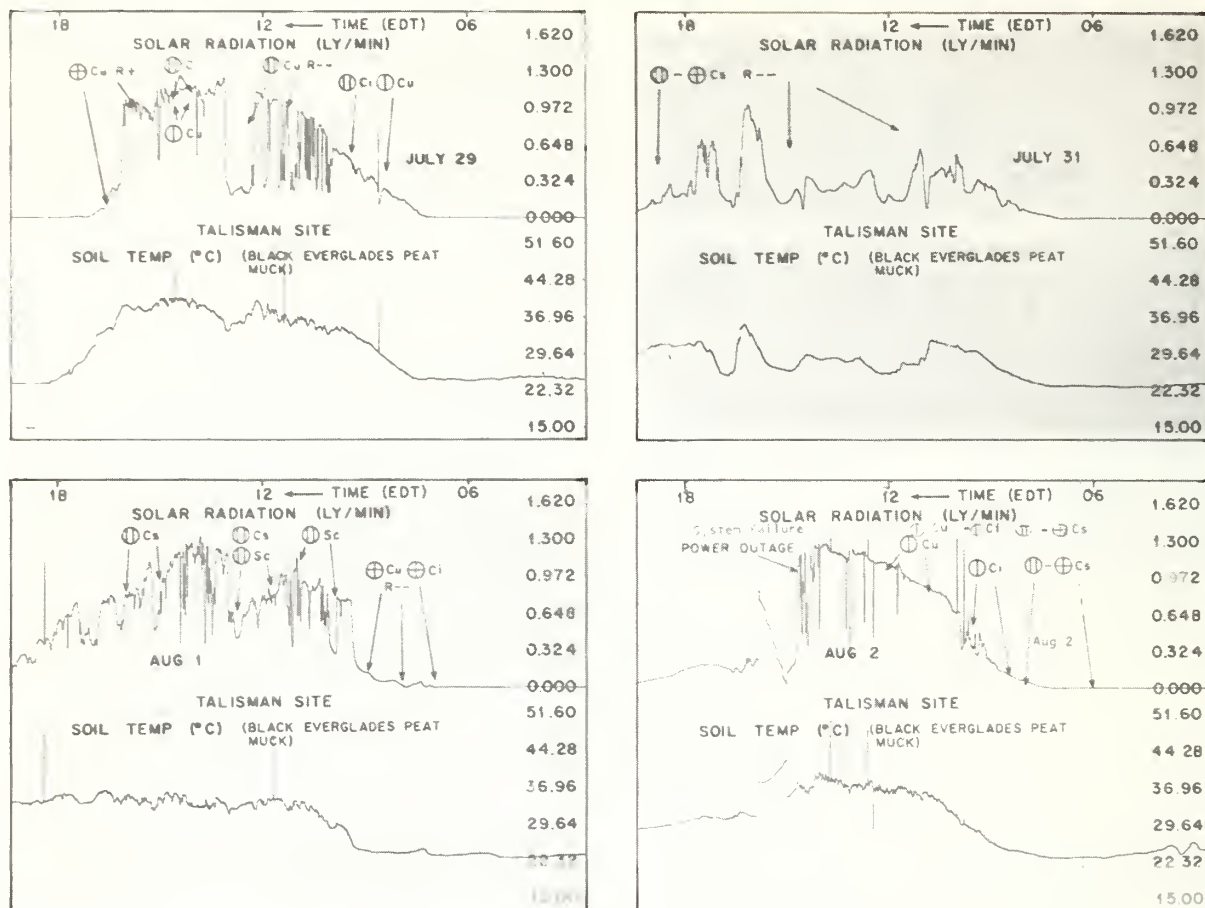


Figure 10. Solar radiation and soil temperature record for Talisman site on (a) July 29, 1975, (b) July 31, 1975, (c) August 1, 1975, and (d) August 2, 1975. The upper record for each day is incoming solar radiation (Ly/min). The lower record for each day is soil surface temperature ($^{\circ}\text{C}$) at 0.5 cm in black Everglades peat muck soil. Cloud cover and rainfall symbols refer to portions of traces marked by arrows.

4.4 Evaporation

to rainfall immediately. The radiation and temperature records for July 31 clearly illustrate the influence of cirriform cloud on surface heating. The clouds and rainfall on this diagram pertain to the entire period shown on the time axis.

The examples shown also demonstrate the aperiodic nature of surface heating during summer in South Florida. It is clear, therefore, that formulations of surface heating as simple harmonic (Carslaw and Jaeger, 1959; Watson, K., 1971) or sinusoidal are not appropriate forcing functions in modeling the sea breeze over South Florida.

Seven National Weather Service observation stations in South Florida measure daily the pan water evaporation loss (Environmental Science Services Administration, 1968). A standard factor of 0.70 is applied to the pan values to obtain a representative water loss value applicable to lakes and other large water bodies.

Unfortunately, none of the observation stations lies along the cross section. The evaporation values from the seven stations are averaged and used in water-budgeting computations to determine soil moisture. This procedure is fully explained in Section 6.

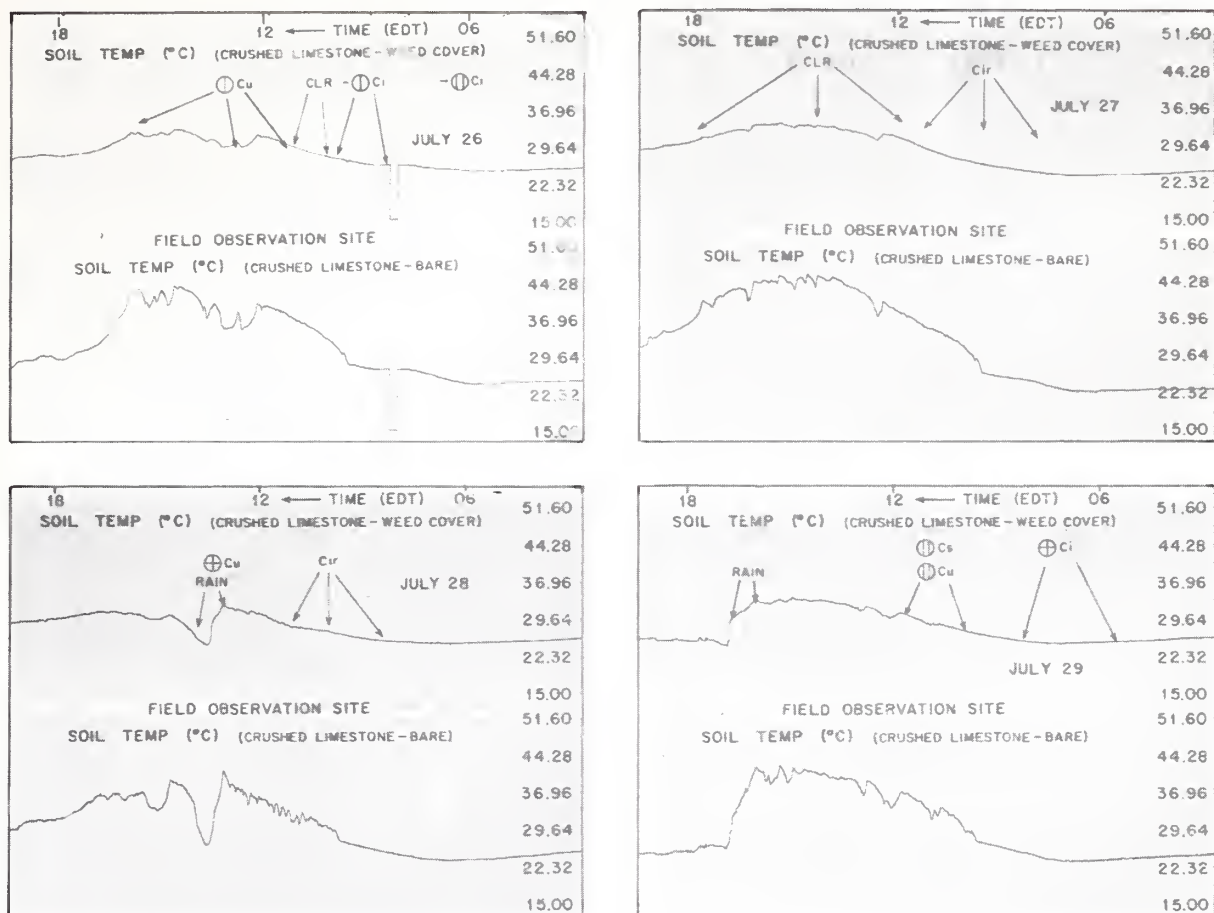


Figure 11. Soil surface temperature record for the field observation site on (a) July 26, 1975, (b) July 27, 1975, (c) July 28, 1975, and (d) July 29, 1975. The upper record for each day is soil surface temperature ($^{\circ}\text{C}$) at 0.5 cm in crushed beige limestone with a scanty weed cover. The lower record is soil surface temperature ($^{\circ}\text{C}$) for the same limestone surface a few feet away with no vegetation cover. Cloud cover and rainfall symbols refer to portions of traces indicated by arrows.

4.5 Emissivity

Although surface emissivity values for the study region, as reported in the University of Florida IFAS (1975) Mid-Term Report, varied from 0.908 (coastal and sandy regions) to 0.98 (agricultural region with black muck south of Lake Okeechobee), the single value of 0.98 is adopted. The lower values were representative of winter conditions. During the wet season, the moistened surfaces would have values closer to 1.0.

4.6 Soil Surface Temperatures

Figures 11 through 13 show the soil surface (0.5 cm deep) temperature profiles for July 25 through August 3, 1975, at FOS. Since solar radiation observations were not made at FOS, comparisons between radiation and temperature measurements were not possible. For each day, the lower set of curves is the temperature profile for the light beige, crushed limestone fill used for the road adjacent to FOS. The upper set of curves is the temperature profile for the same surface partially covered by weeds. The consistently lower temperatures in the upper curves during daylight hours and the higher temperatures during hours of darkness illustrate the modifying effect of sparse vegetation.

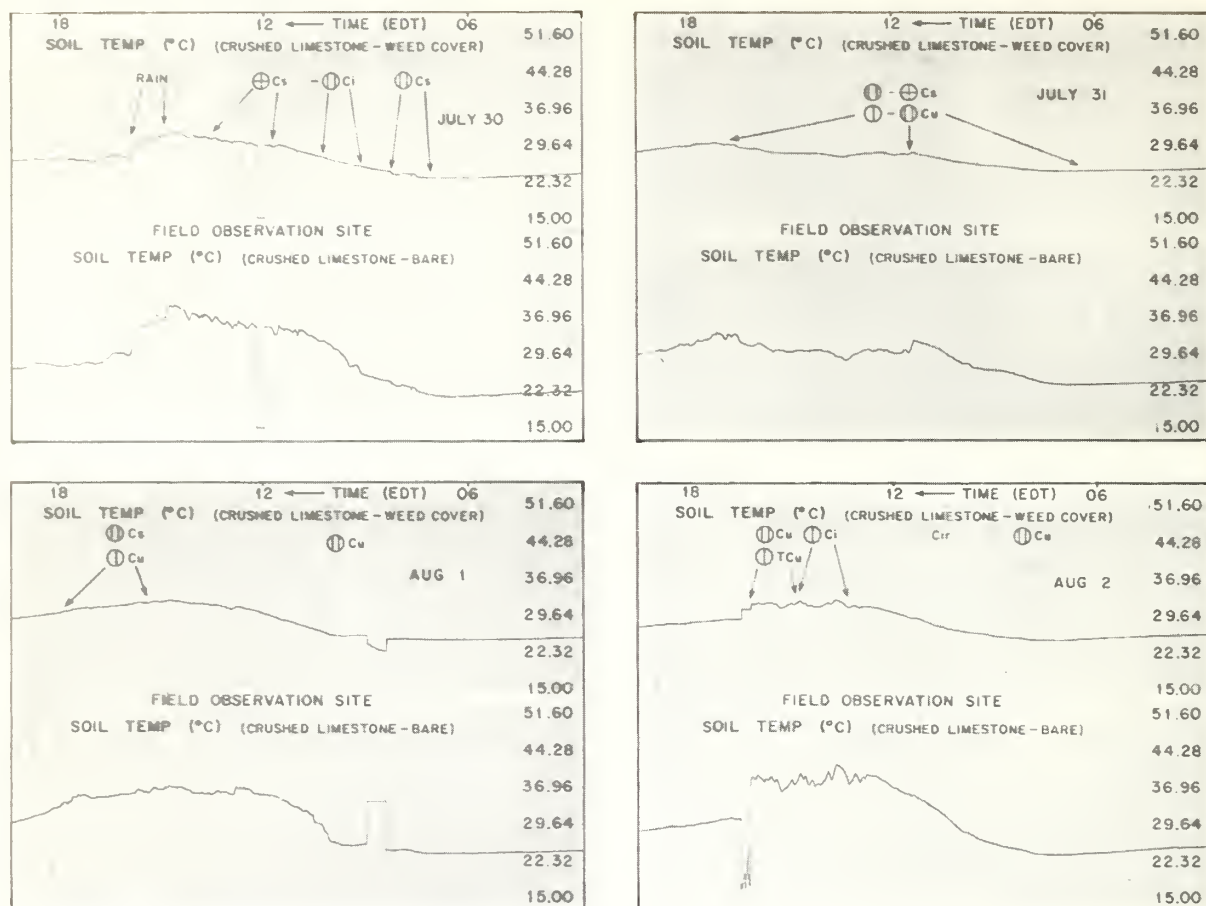


Figure 12. Soil surface temperature record for the field observation site on (a) July 30, 1975, (b) July 31, 1975, (c) August 1, 1975, and (d) August 2, 1975. (See legend, Fig. 11.)

The temperature traces reveal the influence of cloud cover and rainfall. Cloud cover from July 26 through July 31 was obtained from SMS-1 imagery. The cloud cover was established from all-sky camera color photographs taken every 10 min at the site for August 1, 2, and 3. The onset, duration, and cessation of rainfall were established with nearby mesonet rainfall gages and all-sky photos. The onset of the drying phase (Priestley and Taylor, 1972) can be seen on August 1 (July 31 was dry, but thick, persistent cirriform clouds delayed drying for a day). This single station record is indicative of the inhomogeneities in surface temperature that can exist over the peninsula on any given day.

Figure 14 shows representative daytime (near noon solar time) profiles along 26°30'N across the Florida peninsula of 600-m wind, 600-m temperature, 600-m dew point, and ground surface temperature. For information concerning the gather-

ing and processing of this data, see section 3, pages 29–62 of NOAA Tech. Memo. ERL WMPO-28 (Staff, Cumulus Group, 1976), which deals with cloud physics. The surface temperatures were derived from a Barnes PRT-5 radiometer. This sensor was part of the FACE 1975 instrumentation affixed to the NOAA DC-6 aircraft. At this level, effective surface temperature was reduced by 1° from the actual because of atmospheric attenuation. The most obvious feature in the profiles is the variation among them. As cloud bases were above 600 m, the variations did not result from clouds intervening between the sensor and the surface. The spatial and temporal variations in the surface temperature resulted from differences in surface albedo, thermal inertia, soil moisture, and clouds. The clouds acted to cool the surface by shielding it from solar radiation and at the same time retarded cooling by providing increased downward long-wave radiation.

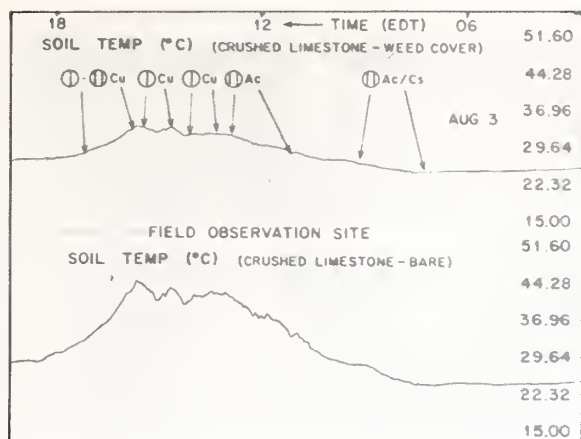


Figure 13. Soil surface temperature record for the field observation site on August 3, 1975. (See legend, Fig. 11.) The higher surface temperatures on this day reflect the onset of the drying phase.

Certain prominent spatial temperature difference patterns are evident on July 7 and 8. On July 10, a very synoptically disturbed day, convective activity and extensive cirrus were observed over the eastern half of South Florida much earlier than normal. Note the high surface temperatures across the western half of the cross section. This is a good example of the interaction effect of clouds where the mesoscale convergence associated with differential heating is shifted some tens of kilometers by alterations in the heating pattern. The air temperature and dew point profiles were elevated in this western portion and acted to retard cooling as sensible and latent heat flux from the surface was reduced.

Figure 15 shows the temperature profile from a NOAA DC-6 traverse across the peninsula shortly after 0000 EDT on August 20, 1975. One reason for conducting this night flight was to obtain a representative midnight temperature profile for determining the thermal inertia.

4.7 Water Surface Temperatures

Observations of water surface temperatures are important in South Florida, because the diurnal range varies widely as a function of depth and recency of rainfall. Water surface temperature records for South Florida water bodies are practically nonexistent. There is, however, a considerable record of subsurface temperature for natural water bodies which is maintained by the Miami-based Water Resources Division, U. S. Geological Survey. Temperature measurements were made at an average depth of 6 inches in a marsh (2 ft

deep), a pond (4 ft deep), a borrow pit (30 ft deep), and a creek (1 ft deep). Representative diurnal temperature variations ranged from 4° to 8°C. To illustrate depth dependence, a small pond in the Everglades only 5 inches deep in mid-May experienced a 14°C diurnal temperature variation. The same pond, having attained a depth of 12 inches in mid-August, experienced a variation of 9.5°C.

To supplement these observations, special water surface temperature measurements were taken at Belle Glade during the FACE 1975 experiment. The water surface probe was identical to the soil surface probes used at FOS and the Talisman site. The probe was fixed to the bottom of a styrofoam sheet which floated in a 4- to 5-ft-deep irrigation and drainage canal that was approximately 15 ft wide. Most of the time, the water was stagnant or only slowly moving. On occasion, floodgates were opened so that the water was forced to move. Representative noon-to-midnight temperature differences had an average range of 1.13°C, with the maximum range being 3.4°C.

4.8 Inference of Thermal Inertia

It was noted in Section 2.2 that thermal inertia is not an observed quantity, but rather inferred from a knowledge of the noon-midnight surface temperature difference (ΔT) and the albedo. It was further noted that thermal inertia can be derived from a graph (fig. 2) relating albedo to thermal inertia and ΔT . When the graph is used, certain precautions must be observed. Care must be exercised to insure that ΔT is determined for a midnight-to-noon period that has minimum cloud cover. The land surface must be allowed to cool during the early morning hours without receiving downward infrared radiation from the bases of clouds. During the period after sunrise, the land surface must be exposed to solar radiation. The most important precaution relates to the interpretation and usage of the thermal inertia values deduced from ΔT and albedo values for soils having significant soil moisture contents in the upper few centimeters (arbitrarily chosen here as soil moisture in excess of 25% of field capacity).

The empirical relationship shown by figure 2 was based upon the energy balance between downward solar and atmospheric infrared radiation and upward infrared radiation. Latent and sensible heat were not considered. The evapotranspiration component exercises such a large influence on the net flux that enters the surface that an observed ΔT could reflect more the effect of evapotranspiration than thermal inertia.

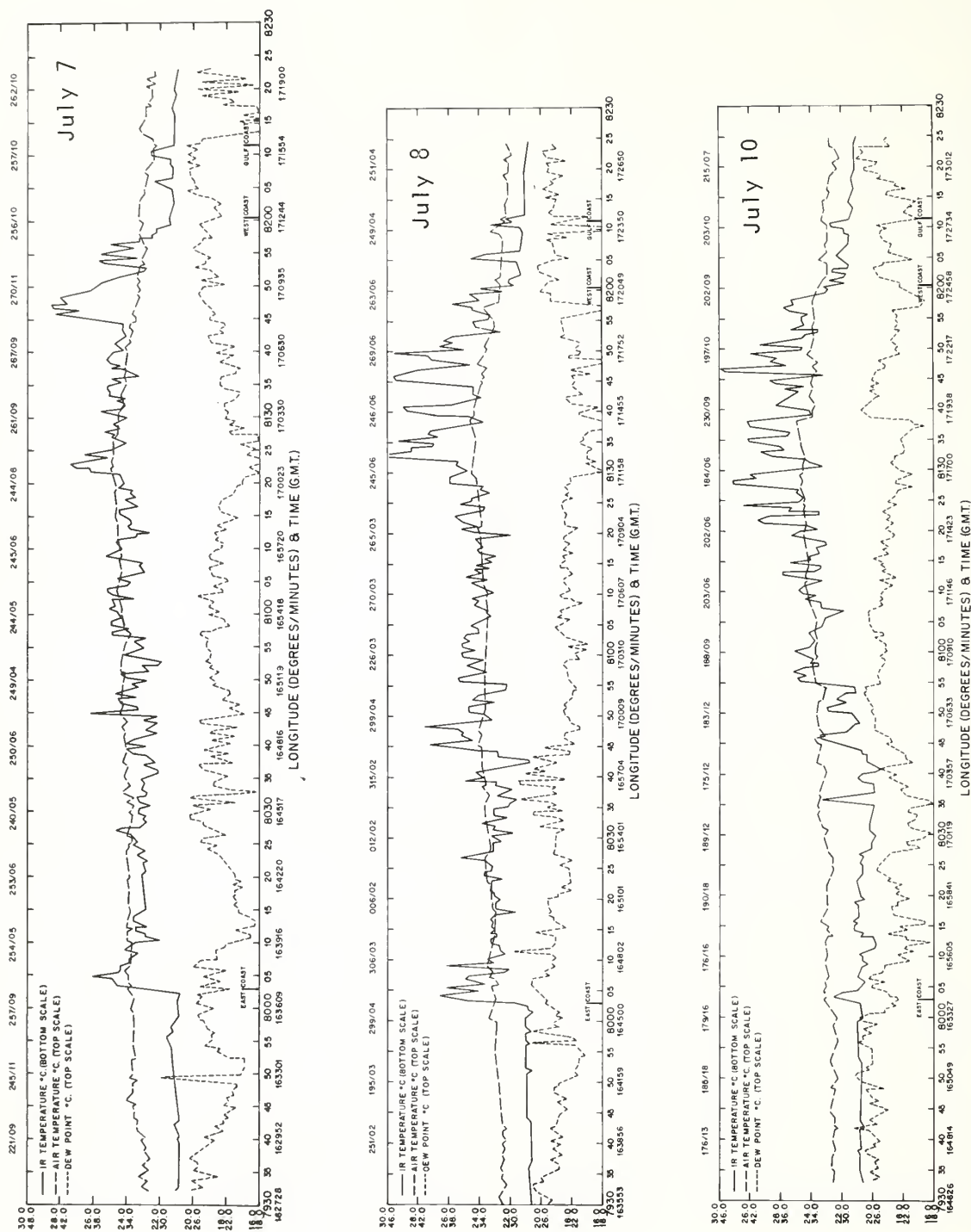


Figure 14. Representative daytime profiles across the Florida peninsula at 26°30'N for (a) July 7, 1975, (b) July 8, 1975, and (c) July 10, 1975. Pairs of numbers on the vertical ordinate indicate air temperature and dew point (top), and surface IR temperature (bottom). Wind direction/wind speed (kn) are given at the top of each diagram.

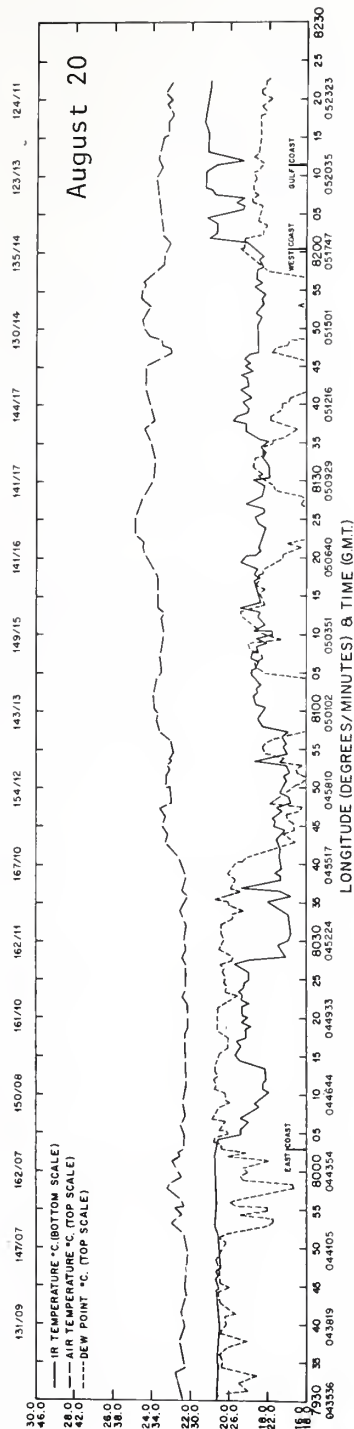


Figure 15. Representative midnight temperature profiles across the Florida peninsula at 26°30'N for August 20, 1975. (See legend, Fig. 14.)

As a check on thermal inertia values deduced from soil surface temperature measurements from FOS and Talisman under clear sky conditions, two methods of thermal inertia determination for selected clear days were used. The first was direct use of figure 2. (The albedo for Talisman is estimated to be 7%, and that for FOS is estimated to be 18%.) The second method is considered the most reliable, but the most difficult to use with remote sensing. The thermal inertia is calculated from (1) for a period shortly before sunrise. The equation is repeated here for convenience.

$$T = T_0 + \frac{2F_n}{TI} \left(\frac{\Delta t}{\pi} \right)^{1/2} \quad (1)$$

T is the final surface temperature, T_0 is the initial surface temperature, Δt is the time period in seconds from 0200 EST to 0500 EST, TI is thermal inertia and is the quantity to be determined, and F_n is the net energy flux entering the surface. The components of F_n are the downward atmospheric radiation and the upward surface radiation based upon the observed surface temperature at 0300 EST. Evaporation and sensible heat fluxes are very small during early morning hours and need not be considered. Under these conditions of almost constant flux, a reliable value of the thermal inertia of the surface can be calculated. Results are in table 3.

It is evident that the two methods give different results. It is not readily apparent why thermal inertias calculated by the second method for Talisman on July 20 and 22 are higher than the first method. For dry days, the calculated thermal inertias are much lower than those obtained from the graph.

Figure 2 is considered very reliable for use over heavily developed areas with minimal soil and vegetation. For example, the near-noon surface temperature maximum of 44°C on July 27, 1975 (not shown), along the east coast at 26°30'N, 80°07'W is compared with the surface temperature of 24°C just after midnight, August 20, 1975 (fig. 15). The thermal inertia from figure 2, in which a surface albedo of 25% is used, is 0.06. This is a representative value for many types of construction materials.

High thermal inertias which characterize deep-water bodies can be relied upon to define those areas which will heat much slower than others during a typical daily sea breeze cycle. Interpretation can be complicated by the presence of surface vegetation. For example, on the basis of July 27 and August 20 measurements, the thermal inertia of the conservation area at 80°20'W (albedo is 7%) with a temperature maximum of 33°C

Table 3.
Thermal inertia values for surface

Site	Date	Soil condition	First method		Second method	
			ΔT	TI	ΔT	TI
Talisman	7/20	Wet	11.3	0.156	0.2	0.313
Talisman	7/22	Wet	8.5	0.180	0.2	0.345
Talisman	7/26	Moist	10.8	0.150	0.7	0.092
Talisman	8/17	Wet	9.8	0.191	0.7	0.213
Talisman	8/7	Dry	12.4	0.135	1.0	0.06
Talisman	8/25	Dry	10.4	0.151	1.0	0.075
FOS	8/6	Dry	9.4	0.14	1.2	0.091
FOS	8/20	Wet	9.6	0.136	0.6	0.123

and a minimum of 25°C is 0.195. This is lower than one would expect for a water body having such large horizontal dimensions and depths from 4 to 6 ft. This results from the increase from 1973 to the present of broad-leaved vegetation on its surface. This increase has been photographically documented. Thermal inertia for areas with vegetation will have a larger diurnal range than TI for a water surface.

Thus, those areas having soil or a mix of soil and vegetation are the problem areas. The problem in remote sensing of thermal inertia for wet soils resides in the evaporation being strongly dependent upon soil moisture which is, in turn, strongly dependent on soil type. Whether erroneous estimates of thermal inertia for wet surface conditions present serious problems for numerical simulation of the sea breeze is a subject that is addressed in Section 6.

4.9 Summary

Along the Florida study area at 26°30'N, albedo, surface temperature, cloud cover, short- and long-wave radiation, and rainfall and wind data were gathered in support of the NOAA FACE 1975 cumulus modification experiment. The albedo and soil surface temperature data are important for establishing the ranges of albedo and thermal inertia that occur over Florida.

As a result of the diverse topographical features across Florida, considerable variations exist in albedo. Albedo values range from 5% to 30%. Incoming solar radiation is markedly affected by cloud cover and type. Peak solar radiation values with variable cloud cover are about 1.32 Ly min⁻¹. Evaporation observations are pan observations, which are taken at relatively few stations in South Florida. Surface emissivity is specified as 0.98, which is a reasonable figure for moist and vegetated regions of South Florida.

Soil surface temperature records show considerable damping of the temperature trace with

clouds and rainfall. The influence of cirriform clouds in reducing the diurnal temperature amplitude is significant. Soil moisture also reduces the diurnal amplitude. The onset of the drying phase, which shows in elevated surface temperatures, can be seen about 3 days after rainfall of ½ in or more. The aperiodic, irregular short-wave radiation and soil surface temperature records show that sinusoidal or other harmonic heating formulations are not realistic forcing functions for "simulating surface heating in models of the South Florida sea breeze."

Surface temperatures across Florida, derived from an aircraft radiometer, show certain recurring temperature maxima and minima which result from surface inhomogeneities. On days when organized cloud cover prevails over one portion of the cross section, the unshaded portion exhibits maxima in surface temperature, air temperature, and dew point.

Water surface temperatures, as expected, show a strong dependence on depth and areal coverage of the water body. Minimum land surface temperatures measure about 21°C and maxima range from 33°C to 45°C, depending upon soil type, sky conditions, and soil moisture.

Two methods of estimating thermal inertia from observations of albedo and diurnal surface temperature range are discussed. Both methods must be used with discretion. The range of thermal inertia is determined to be from 0.05 to 0.30 across the state.

No soil moisture observations were taken, and estimation of this quantity for a case study is discussed in Section 6.

5. THEORETICAL ELEMENTS

The two-dimensional physical dynamic model that serves as the vehicle for evaluating the atmospheric response to differential surface heating is based upon the three-dimensional sea breeze model developed by Pielke (1974). It is a hydrostatic, primitive equation model which describes the initiation and evolution of sea breeze convergence zones over South Florida. As the model does not treat moist convection, moisture phase changes caused by condensation are neglected. The motions described by the equations are confined to the lowest 5 km. The model includes a complete heating function. Short- and long-wave radiation, sensible heat, evapotranspiration, surface heat budget, and clouds are treated in detail. The two-dimensional model is used to study the sea breeze as it occurs across Florida along an 11-km-wide strip at 26°30'N.

The two-dimensional model used here includes the following modifications by Pielke and Mahrer (1975):

1) Use of "total state." The equations are no longer decomposed into separate basic and perturbation fields.

2) Addition of predictive equation for the growth of the planetary boundary layer. The planetary boundary layer is defined as that layer of the atmosphere from the earth's surface to the level at which the flow becomes geostrophic. It includes the surface boundary layer immediately adjacent to the earth's surface within which shear stresses are approximately constant. The specification of the top of the planetary boundary layer (Pielke, 1974) is important, as it is the upper limit for the profile function used to determine vertical exchange coefficients, which are required to calculate turbulent transfer of momentum, heat, and moisture.

3) Inclusion of vertical shear of the geostrophic wind. Vertical wind shear must be considered in the velocity profile if reasonably accurate predictions of sea breeze scalar and vector fields are to result (Pielke and Mahrer, 1975). The vertical wind shear also enters into the prediction equation for the growth of the planetary boundary layer. If, for example, easterly flow becomes stronger with height, the deepening boundary layer is accelerated westward as it is influenced by the increased momentum aloft. If easterly surface winds are overlain by westerly winds, westward motion is retarded.

4) Inclusion of surface layer parameterizations. With the inclusion of the surface layer parameterizations of Businger (1973), more accurate model predictions of wind and temperature are obtained. Vertical diffusion is represented by implicit approximations, permitting a larger time step. Predicted surface temperatures now conform more closely with reality than in earlier experiments employing a different surface layer formulation.

5) Use of virtual potential temperature. Virtual potential temperature is used for the calculation of the vertical pressure profile and the nondimensional temperature profile in the surface layer. This provides a more accurate representation of the pressure field which is so basic for determining sea breeze structure and intensity.

The semi-implicit forward-upstream differencing scheme used by Pielke (1974) is retained in this model. The scheme is advantageous, because it damps out spurious short wavelengths arising from nonlinear computational instabilities. Mahrer and Pielke (1976, personal communication) state that if (1) the grid interval is smaller than the wavelength, (2) heating is introduced

slowly into the model, and (3) the flow changes slowly in time relative to the time step, the reduction in amplitude of the finite difference prediction of the mesoscale sea breeze disturbance from the true solution is less than 10%. More recently, Pielke (1976, personal communication) found that numerical simulations using spline functions gave results similar to the forward-upstream differencing scheme.

The restriction to two dimensions arises from limitations imposed by computer memory and time requirements. The radiation subroutines account for approximately 57% of the total memory requirements and 25% of CPU time. The two-dimensional version of the model using a heat budget formulation is considered ideal for the systematic evaluation of the atmospheric response to variations in albedo, thermal inertia, soil moisture, and cloud cover.

Although the model does not simulate moist convective processes, it does describe the evolution of mass, heat, and moisture fields within which convection can be generated. The model will predict this evolution for a wide variety of atmospheric surface and cloud conditions, provided the basic flow is largely two-dimensional and parallel to the prescribed study area. As convection, release of latent heat aloft, rainfall, and downdraft interactions increase, the predictive capability of the model diminishes.

The alteration of the dry convective boundary layer in the presence of initial significant moist convection has been noted by Johnson (1977). For example, the height of the planetary boundary layer is depressed by descending motions associated with convection. These processes are not simulated in the model. As convection increases in extent and intensity, the motion fields reflect more the convective elements than the sea breeze regime which established them. The numerical simulation of mesoscale and cumulus scale interactions is a formidable requirement which must consider many more physical processes than those addressed in this paper.

5.1 Model Dynamic Equations

Following are the forms of the equation for this model:

$$\begin{aligned} \frac{\partial u}{\partial t} = & u \frac{\partial u}{\partial x} - w \frac{\partial u}{\partial z} - \theta \frac{\partial \pi}{\partial x} + f_3 v - f_2 w \\ & + \frac{\partial}{\partial z} \left[K_z^{(m)} \frac{\partial u}{\partial z} \right] + \frac{\partial}{\partial x} \left[K_H \frac{\partial u}{\partial x} \right] \end{aligned} \quad (2)$$

(east-west equation of motion),

$$\begin{aligned} \frac{\partial v}{\partial t} + u \frac{\partial v}{\partial x} - w \frac{\partial v}{\partial z} + f_3 u_s - f_3 u \\ + \frac{\partial}{\partial z} \left[K_z^{(m)} \frac{\partial v}{\partial z} \right] + \frac{\partial}{\partial x} \left[K_H \frac{\partial v}{\partial x} \right] \end{aligned} \quad (3)$$

(north-south equation of motion),

$$\begin{aligned} \frac{\partial \theta}{\partial t} = -u \frac{\partial \theta}{\partial x} - w \frac{\partial \theta}{\partial z} \\ + \frac{\partial}{\partial z} \left[K_z^{(\theta)} \frac{\partial \theta}{\partial z} \right] + \frac{\partial}{\partial x} \left[K_H \frac{\partial \theta}{\partial x} \right] + R \end{aligned} \quad (4)$$

(potential temperature equation).

R is the heating contribution from short-wave radiation and long-wave cooling (or heating).

$$\begin{aligned} \frac{\partial q}{\partial t} = -u \frac{\partial q}{\partial x} - w \frac{\partial q}{\partial z} + \frac{\partial}{\partial z} \\ \left[K_z^{(q)} \frac{\partial q}{\partial z} \right] + \frac{\partial}{\partial x} \left[K_H \frac{\partial q}{\partial x} \right] \end{aligned} \quad (5)$$

(specific humidity equation),

$$\frac{\partial w}{\partial z} = - \frac{\partial u}{\partial x} \quad (6)$$

(incompressible continuity equation),

and

$$\frac{\partial \pi}{\partial z} = - \frac{g}{\bar{\theta}} \quad (7)$$

The variable π is a nondimensional pressure and is defined as

$$\pi = c_p \left(\frac{p}{p_{00}} \right)^\chi \quad (8)$$

where $\chi = R/c_p$,

R is the gas constant of dry air,

c_p is specific heat of air at constant pressure.

The diagnostic equations (6) and (7) are solved by the upward integration of (6) from a rigid bottom ($w=0$) corresponding to the surface, whereas (7) is integrated downward from an upper free surface. The initial level of the free surface is chosen to be 4.82 km. As Pielke (1974) states, the choice of a free surface as the upper boundary condition

is dictated by the requirement that the top of the model domain be capable of responding to the addition of heat in a column. The depth of the free surface is calculated from

$$\frac{\partial s}{\partial t} = -u \frac{\partial s}{\partial x} + w_T - \int_{z_T}^{s(t)} \frac{\partial u}{\partial x} dz \quad (9)$$

where z_T is the top Eulerian grid point of the model and $s(t)$ is the height of the free surface. The pressure π on s at time t required in the downward integration of (7) is calculated from

$$\pi[s(t)] = \hat{\pi} - \frac{g}{\bar{\theta}} s(t) - \hat{s} \quad (10)$$

The carat indicates an initial value, and $\bar{\theta}$ is the mean virtual potential temperature in the layer between s and \hat{s} . (Although the chosen level of 4.82 km posed no obvious problems in most of the experiments, it is possible that a higher level would have been appropriate for the more vigorous sea breeze circulation noted in some of the experiments.)

The horizontal exchange coefficient K_H is given by

$$K_H = \alpha_{2D} (\Delta x)^2 \left[\left(\frac{\partial v}{\partial x} \right)^2 + \frac{1}{2} \left(\frac{\partial u}{\partial x} \right)^2 \right]^{1/2}$$

where α_{2D} is given the value of 0.704.

5.2 Model Surface Layer and Planetary Boundary Layer

Realistic simulation of the vertical turbulent transfer of momentum, heat, and moisture depends upon the magnitudes of the vertical exchange coefficients, $K_z^{(m)}$, $K_z^{(\theta)}$, and $K_z^{(q)}$. The form employed here (Pielke, 1974) is

$$K_z^{(\eta)} = \begin{cases} K_z^{(\eta)}|_{z_i} + [(z_i - z)^2 / (z_i - h)^2] \\ \quad \times [K_z^{(\eta)}|_h - K_z^{(\eta)}|_{z_i} + (z - h) \\ \quad \times \{ (\partial/\partial z) K_z^{(\eta)}|_h \\ \quad + 2 (K_z^{(\eta)}|_h - K_z^{(\eta)}|_{z_i}) / (z_i - h) \}], & z_i \geq z \geq h \\ K_z^{(\eta)}|_{z_i}, & z > z_i \\ (z/h) K_z^{(\eta)}|_h, & z < h \end{cases} \quad (11)$$

where η refers to m , θ , or q ; z_i refers to the top of the planetary boundary layer, and h to the top of the surface layer. The value of $K_z^{(\eta)}|_{z_i}$ is assumed

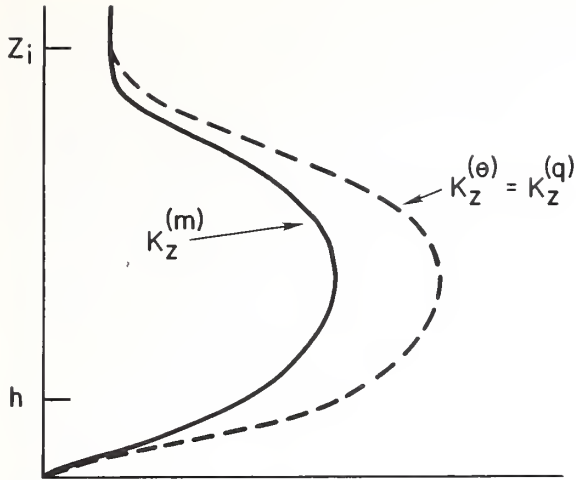


Figure 16. Profile of the eddy exchange coefficients. (Pielke, 1974, fig. 1, with permission from the American Meteorological Society.)

to be $1 \text{ cm}^2 \text{ s}^{-1}$. The coefficients for heat and moisture are assumed identical when there is stable air in the surface layer. For unstable air in the surface layer, the coefficients for heat and moisture are larger. Figure 16 illustrates the functional form.

As the value of the exchange coefficients is dependent upon the heights of the planetary boundary layer (z_i) and surface layer (h), this dependence must be realistically defined during the computational sequence. The prognostic equation for z_i is that of Deardorff (1974).

$$\begin{aligned} \frac{\partial z_i}{\partial t} = & -u \frac{\partial z_i}{\partial x} + w_i \\ & + \frac{1.8 (w_*^3 + 1.1 u_*^3 - 3.3 u_*^2 f_3 z_i)}{g \frac{z_i^2}{\theta} \frac{\partial \theta^*}{\partial z} + 9 w_*^2 + 7.2 u_*^2} \end{aligned} \quad (12)$$

The value of w_* is

$$w_* = \begin{cases} (-\frac{g}{\theta_s} u_* \theta_* z_i)^{1/3}, & \theta_* \leq 0 \\ 0, & \theta_* > 0 \end{cases}$$

where u_* and θ_* are friction velocity and friction temperature, respectively. The quantity w_i is vertical motion of the top of the planetary boundary layer, f_3 is the Coriolis parameter, θ_s is the surface virtual potential temperature, and $\partial \theta^* / \partial z$ the virtual potential temperature gradient across the top of the planetary boundary layer z_i . Existing upper level wind shear at the level z_i is accounted for by the term

$$g \frac{z_i^2}{\theta_s} \frac{\partial \theta^*}{\partial z}$$

This is explained by Pielke and Mahrer (1975) in the following way. The east-west geostrophic wind

$$u_g = \frac{\hat{\theta}}{f_3} \frac{\partial \hat{\pi}}{\partial y},$$

when differentiated with respect to z , can be written as

$$\frac{\partial u_g}{\partial z} = \frac{u_g}{\theta} \frac{\partial \hat{\theta}}{\partial z} + \frac{g}{f \hat{\theta}} \frac{\partial \hat{\theta}}{\partial y}.$$

As $\partial \hat{\theta} / \partial y$ is negligible, the second term on the right can be discarded. With the proper scaling, the term that results,

$$g \frac{z_i^2}{\theta_s} \frac{\partial \theta^*}{\partial z},$$

reflects the gradient of geostrophic wind in the vertical.

With overlying, neutrally stratified air and no surface heat flux, horizontal advection, or vertical motion, the steady-state solution of (12) becomes

$$z_i = 0.33 u_* / f_3. \quad (13)$$

The depth h of the surface layer is given as

$$h = 0.04 z_i.$$

The surface parameterizations of Businger (1973) are reflected in more accurate surface layer nondimensional wind and temperature profiles and a more consistent evaluation of surface momentum, heat, and moisture fluxes. The expressions for these profiles are given by

$$\phi_m = \begin{cases} (1 - 15 \xi)^{-1/2}, & \xi \leq 0 \\ 1 + 4.7 \xi, & \xi > 0 \end{cases} \quad (14)$$

$$\phi_q = \phi_H = \begin{cases} 0.74 (1 - 9 \xi)^{-1/2}, & \xi \leq 0 \\ 0.74 + 4.7 \xi, & \xi > 0 \end{cases} \quad (15)$$

$$\frac{\partial \phi_m}{\partial \xi} = \begin{cases} 3.75 \phi_m^5, & \xi \leq 0 \\ 4.7, & \xi > 0 \end{cases} \quad (16)$$

$$\frac{\partial \phi_H}{\partial \xi} = \begin{cases} 8.22 \phi_H^3, & \xi \leq 0 \\ 4.7, & \xi > 0 \end{cases} \quad (17)$$

$$\text{where } \phi_m = \frac{Kz}{u_*} \frac{\partial u}{\partial z} \text{ and } \phi_H = \frac{Kz}{\theta_*} \frac{\partial \theta}{\partial z}.$$

ξ is the dimensionless height z/L where z is the length scale and L is the Monin-Obukhov stability length. L is given by

$$L = \bar{\theta} u_*^2 / (kg \theta_*)$$

These profiles enter into the friction velocity, friction temperature, and friction specific humidity which are iteratively determined as described in Pielke (1974). These are given by

$$\begin{aligned} u_* &= K(u^2 + v^2)^{1/2} / [\ln(z/z_0) - \psi_1], \\ \theta_* &= K[\theta_v - \theta_v(z_0)] / 0.74 [\ln(z/z_0) - \psi_2] \\ q_* &= K[q - q(z_0)] / 0.74 [\ln(z/z_0) - \psi_2] \end{aligned} \quad (18)$$

where θ_v is virtual potential temperature, and

$$\psi_1 = \begin{cases} 2 \ln [(1 + \phi_m^{-1})/2] \\ \quad + \ln [(1 + \phi_m^{-2})/2] \\ \quad - 2 \tan^{-1} \phi_m^{-1} + \pi/2, & \xi \leq 0 \\ -4.7 \xi, & \xi > 0 \end{cases}$$

$$\psi_2 = \begin{cases} 2 \ln [(1 + 0.74 \phi_H^{-1})/2], & \xi \leq 0 \\ -6.35 \xi, & \xi > 0 \end{cases}$$

The exchange coefficients for momentum, heat, and moisture above the surface layer which are calculated with the aid of (11) are functions of (14) through (17).

$$\begin{aligned} K_z^{(m)}|_h &= k u_* h / \phi_m \\ K_z^{(q)}|_h &= K_z^{(\theta)}|_h = k u_* h / \phi_H \end{aligned}$$

The derivative of $K_z^{(\eta)}|_h$ with height, required in (11), is

$$\frac{\partial}{\partial z} K_z^{(\eta)}|_h = \frac{K_z^{(\eta)}|_h}{L} \left[\frac{1}{\xi_h} - \frac{1}{\phi^{(\eta)}(\xi_h)} \frac{\partial \phi^{(\eta)}(\xi_h)}{\partial \xi} \right]$$

where the superscript η refers to the particular exchange coefficient.

As stated in Pielke and Mahrer (1975), the form of the $K_z^{(\eta)}$ profile discussed above is the same as used in Pielke (1974), except for the difference formulas for θ_m , θ_q , u_* , θ_* , and the additional calculation of q_* . The manner in which $K_z^{(\eta)}$ is used to evaluate the vertical turbulent fluxes is somewhat different, however. If the grid point at which the flux term is evaluated is within the surface layer and is at the lowest level above the ground at which the flux term is evaluated, then the explicit surface layer flux form is given by

$$\begin{aligned} K_z^{(m)} \frac{\partial u}{\partial z} &= u_*|_x^2, & K_z^{(m)} \frac{\partial v}{\partial z} &= u_*|_y^2 \\ K_z^{(\theta)} \frac{\partial \theta_v}{\partial z} &= u_* \theta_*, & K_z^{(q)} \frac{\partial q}{\partial z} &= u_* q_* \end{aligned}$$

The subscripts x and y of u_* refer to the friction velocity components appropriate for these axes. If, on the other hand, the grid point is above

the lowest level at which the flux term is evaluated, the value of $K_z^{(\eta)}$ is calculated from (11) and multiplied by the vertical gradient of the appropriate dependent variable as in the past. In the special case where the grid point is the lowest one above the ground, but is still above the surface layer, the exchange coefficient is still evaluated using (11), but the vertical gradient term is calculated using surface layer similarity theory as given by

$$\begin{aligned} K_z^{(m)} \frac{\partial u}{\partial z} &= K_z^{(m)} \frac{u_*|_x \phi_m}{kz}, & K_z^{(m)} \frac{\partial v}{\partial z} &= K_z^{(m)} \frac{u_*|_y \phi_m}{kz} \\ K_z^{(\theta)} \frac{\partial \theta_v}{\partial z} &= K_z^{(\theta)} \frac{\theta_* \phi_H}{kz}, & K_z^{(q)} \frac{\partial q}{\partial z} &= K_z^{(q)} \frac{q_* \phi_H}{kz} \end{aligned}$$

The last technique is required because an evaluation of the vertical derivative between the ground and the next grid level above in the standard finite-difference fashion assumes that a linear gradient exists between that level and the ground. The gradient is usually steepest just above the surface and decreases in the vicinity of the first grid point.

The surface layer formulas specify temperature and specific humidity at z_0 rather than at the surface. Based upon the work of Zilitinkevich (1970) and Deardorff (1974), temperature and specific humidity at z_0 are given by

$$\theta_v(z_0) = \theta_{v_{sfc}} + 0.0962 \frac{\theta_*}{k} \left(\frac{u_* z_0}{\nu} \right)^{0.45}, \quad (19)$$

and

$$q(z_0) = q_{sfc} + 0.0962 \frac{q_*}{k} \left(\frac{u_* z_0}{\nu} \right)^{0.45} \quad (20)$$

where the subscript sfc refers to the surface, and ν is the kinematic viscosity. The quantity raised to the fractional power is the roughness Reynolds number. As θ_* is negative in the case of an unstable surface layer, the difference between θ_{sfc} and θ_{z_0} , for example, can be as great as 8°C for a highly heated surface.

The quantity q_{sfc} is the specific humidity at the air-ground interface. It refers to the soil moisture in the top 10 to 15 cm of bare soil. This moisture is transformed into water vapor within the soil and propagates upward to the surface in response to pressure gradients (suction) across the soil-air interface. At the interface, specific humidity can vary considerably from shelter level values. In the case of vegetated surfaces, the transpiration process is more complicated as was shown in Section 2.3. The quantity q_{sfc} is given by

$$q_{sfc} = \frac{(0.62197)e_s}{P_0 - e_s} \times RH$$

where sfc refers to the surface, q_{sfc} is specific humidity at the surface, e_s is saturation vapor pressure at the surface, P_0 is surface pressure, and RH is relative humidity at the air-ground interface (Nappo, 1975).

The saturation vapor pressure is computed using Tetens' formula as employed by Pielke (1974)

$$e_s = 6.1078 \exp \left[\frac{17.2693882(T_s - 273.16)}{T_s - 35.86} \right]$$

where T_s is surface temperature.

The expressions for $\theta(z_0)$ and $q(z_0)$ are highly significant since they couple the surface conditions to the overlying atmosphere. The ultimate distribution of surface heat and surface moisture, which in large measure governs the intensity and structure of the sea breeze, is a function of the surface values and the turbulent properties of the lowest layers of the atmosphere. Surface heating and evaporation, turbulent transfer of heat, moisture, and momentum, and altered sea breeze structure, are thoroughly interactive processes. Changes in surface temperature, in addition to being dependent upon net fluxes, are dependent upon surface layer profile functions, which are, in turn, dependent upon θ_* , u_* and advective terms in the primitive equations.

Although primary emphasis in this report is on the response of the sea breeze to differential heating at the surface, heating in atmospheric layers from short- and long-wave radiation is considered in the potential temperature equation (4). The effects of direct heating of the atmosphere are secondary compared with those resulting from absorption at the surface.

5.3 Heating Function

A complete heating function has been constructed to initiate the forcing of the thermally driven mesoscale circulations. The important energy components are solar radiation, atmospheric downward radiation, upward-directed surface radiation, sensible heat, latent heat, and soil (or water) heat flux. The contribution of the soil heat flux to the net flux is determined by the value of thermal inertia. Geothermal (Watson, 1975) and anthropogenic (Yu and Wagner, 1975) heat sources are neglected in the present work. The net radiation flux into the ground and the atmospheric heating rates are determined after accounting for

the transmission, absorption, and reflection of solar radiation, and long-wave terrestrial and atmospheric radiation. The radiation received and emitted by the ground is the energy component of principal interest. The heating rates are also calculated at each of the seven model levels where potential temperature and specific humidity are defined. This atmospheric heating is included for the sake of completeness and also because absorption in the atmospheric layers is already accounted for in calculating the attenuation of the fluxes.

Surface and atmospheric heating and cooling effects are greatly enhanced by clouds (Lacis and Hansen, 1974; Fleming and Cox, 1974). Also, as the vertical water vapor path length changes significantly in the convergence and divergence regions as the day progresses, the radiation components will change accordingly.

Coantic and Sequin (1971) show the importance of turbulent and radiative interactions in the surface layer. They conclude from their experiments with a 10-m surface layer, that "radiative flux divergence always acts in such a way as to increase the absolute value of turbulent heat flux over almost all of the surface layer, as compared to its value at the surface." Mak (1974) investigated radiative effects in a planetary boundary layer. He showed that an increase of water vapor near the surface enabled a near-equilibrium planetary boundary layer to exist. The attainment of this condition was marked by a simple balance of convergence of eddy heat flux and a divergence of radiant flux under typical atmospheric conditions. His conclusion that the sum of the radiant flux and sensible heat flux is the same at all levels is equivalent to Coantic's for the surface layer. Therefore, it was considered proper to include atmospheric radiative processes, albeit the vertical resolution is less than that prescribed by the aforementioned authors.

The following discussion of the radiative processes and related factors is guided primarily by the sequence in which the solar beam is affected from the top of the atmosphere to the ground. Long wave radiation transfer is discussed in Section 5.6.

5.4 Solar Spectrum

From the extraterrestrial solar spectral data of Thekaekara (1974), 25 spectral intervals were chosen. The choices were guided by the manner and sequence in which the radiant energy was affected by ozone, cirrus, molecular scattering, water vapor, carbon dioxide, oxygen, dust, and cloud forms other than cirrus. It was assumed that

Table 4.
Solar spectral intervals selected for the model

No.	Wavelength (μm)	Spectral energy ($\text{cal cm}^{-2} \text{s}^{-1} \times 10^{-6}$)	Attenuator
1	0.29 – 0.38	2000.785	Ozone absorption and scatter
2	0.38 – 0.46	3110.325	Molecular scatter
3	0.46 – 0.695	9608.161	Ozone absorption and scatter
4	0.695– 0.75	1720.017	Ozone absorption and scatter; Water vapor absorption
5	0.750– 0.785	994.901	Molecular scatter
6	0.785– 0.835	1295.49	Water vapor absorption
7	0.835– 0.855	478.56	Molecular scatter
8	0.855– 0.895	895.56	Water vapor scatter
9	0.895– 1.05	2931.33	Molecular scatter
10	1.05 – 1.20	2035.173	Water vapor absorption
11	1.20 – 1.25	551.031	Molecular scatter
12	1.25 – 1.50	2109.798	Water vapor absorption
13	1.50 – 1.55	331.335	Molecular scatter
14	1.55 – 2.35	2568.891	Water vapor absorption
15	2.35 – 3.85	911.978	Water vapor absorption
16	3.35 – 3.85	163.697	Water vapor absorption
17	3.85 – 4.55	133.438	Water vapor absorption
18	4.55 – 5.50	83.235	Water vapor absorption
19	5.50 – 6.50	50.268	Water vapor absorption
20	6.50 – 9.50	50.578	Water vapor absorption
21	9.50 – 10.50	6.054	None
22	10.50 – 12.50	6.997	None
23	12.50 – 17.50	6.43	Water vapor absorption
24	17.50 – 30.00	3.036	Water vapor absorption
25	30.00 –1000.00	0.757	Water vapor absorption

*Total spectral energy: $1.923 \text{ cal cm}^{-2} \text{ min}^{-1}$ (with energy at wavelengths less than $0.29 \mu\text{m}$ neglected)

all radiation at wavelengths less than $0.29 \mu\text{m}$ was completely absorbed by ozone. Table 4 lists the spectral intervals with the absorbers and scatterers appropriate to them. It should be noted that bulk depletion formulas for dust, carbon dioxide, and oxygen were applied to the total incoming spectral energy.

5.5 Solar Energy Transfer Processes

Figure 17 is a schematic diagram showing how the solar beam is depleted by the atmosphere and clouds before reaching the surface. Radiation transfer processes are given in Appendix A. The major portion of the solar radiation transfer processes is based on the formulations of Lacis and Hansen (1974) and Liou (1973). Certain modifications to the total spectrum treatment of Lacis and Hansen have been introduced because of the requirement to identify the spectral energy in each of the 25 chosen intervals. The modifications were necessary because this energy is selectively affected by ozone, cirrus, atmospheric particles and gases, lower clouds, and the surface in a certain sequence.

The attenuation of the solar beam by ozone is accounted for in the manner described by Lacis

and Hansen (1974). Stratospheric heating rates are not calculated since the model levels do not extend above 500 mb. Ozone absorption calculations are carried out to determine the transmitted spectral energy that would affect the troposphere and the surface. No effort is made to determine ozone absorption resulting from diffuse spectral energy that is reflected upwards by the lower atmosphere and ground.

The procedures for treating solar irradiance through cirrus cloud layers are based upon Liou (1972, 1973, 1974). The theory describing extinction caused by the scattering of solar irradiance in the visible and infrared is developed rigorously in those papers. Fleming and Cox (1974) summarize concisely the fundamental requirements for determining radiative transfer in cirrus clouds: "The determination of the radiative effects of a cirrus cloud layer requires information about the particles comprising the cloud. The composition, size, shape, orientation, and number density of the cloud particles determine their effect on the scattering and absorption of incident solar energy. The geometric thickness, when combined with these microphysical cloud properties, determines the short wave optical thickness and the range of probable infrared emissivity of the cirrus layer."

In table 5, the required optical properties are

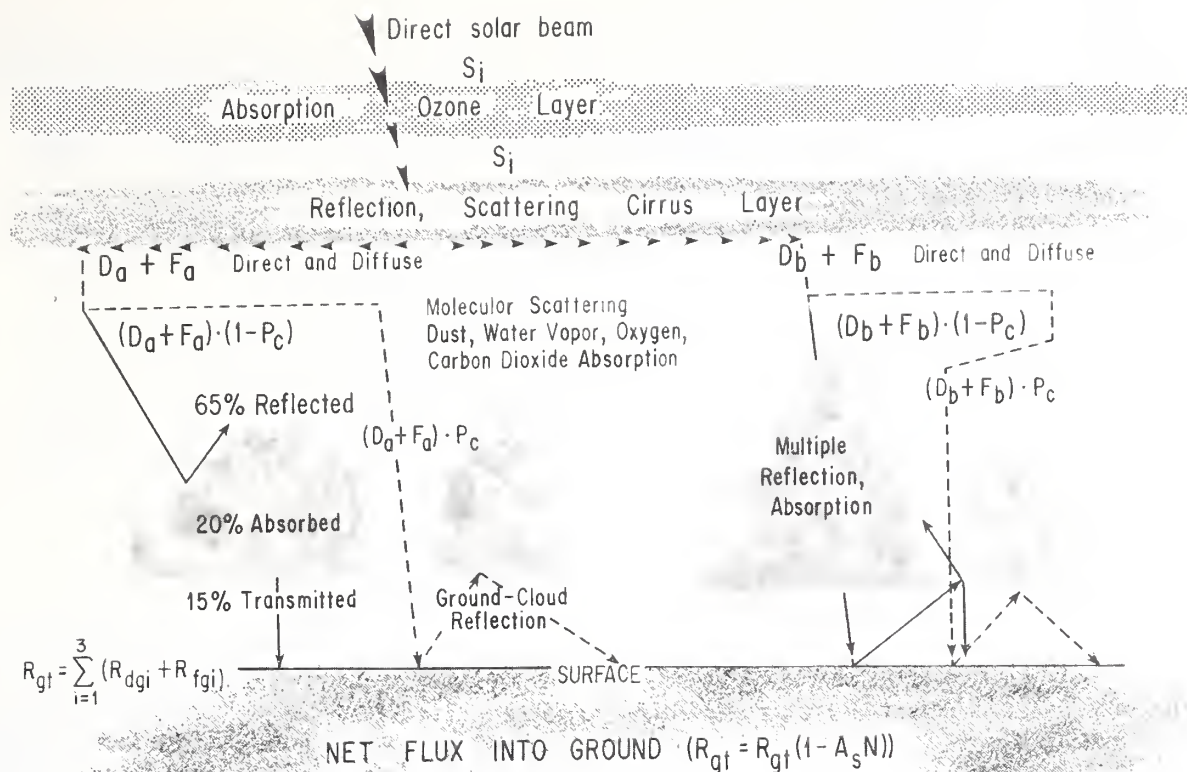


Figure 17. Solar radiation transfer. P_c is percent of radiation coming through cumulus cloud field. $(1 - P_c)$ is percent of radiation intercepted by clouds and subjected to reflection, transmission, or multiple scattering and absorption. $D_a + F_a$ is direct and diffuse radiation not affected by water vapor absorption. $D_b + F_b$ is direct and diffuse radiation affected by vapor absorption. R_{gt} is the net solar flux that enters the surface layer. A_s is surface albedo and N is a factor that depends upon solar zenith angle.

classified according to the spectral intervals chosen for the radiative transfer through cirrus. The optical properties Liou used for the wavelengths containing most of the incoming solar energy were based on observations of typical cirrus particles (Liou, 1973; Fleming and Cox, 1974). The number density is about 0.5 cm^{-3} , while the crystal length and radius are about $200 \mu\text{m}$ and $30 \mu\text{m}$, respectively. It is recognized that cirrus optical properties can vary widely in space and time in some meteorological situations (Platt, 1974).

The optical thickness is defined as

$$\tau^* = \beta_e \cdot H$$

where $H(\text{km})$ is defined as the geometric thickness of the cirrus layer. The cirrus layers treated in this paper are assumed to have the optical properties shown in table 5. Variations in optical thickness are assumed to be due strictly to changes in geometric thickness. Geometric thickness is specified for sensitivity experiments discussed in Section 6.

For case studies (Section 6), the geometric thickness is determined with the aid of a color densitometer (Appendix B).

Phase functions for the eight spectral regions (table 5) were obtained from graphical data presented in Liou (1972, 1973, 1974). Figure 18 from Liou (1973) is an example of the phase function $P(\Theta)$ versus scattering angle (Θ). The 180-degree range on the abscissas was divided into 120 intervals and $P(\cos \Theta)$ was extracted. The phase functions are required to describe the directional fractionation of downcoming and upcoming streams of radiation. Transfer of solar radiation through cirriform is treated in Appendix A.

In this study, low clouds refer to cloud types other than cirriform. Thus, cloud forms ranging from stratocumulus to cumulonimbus are classified as low clouds. It is necessary to know grid square areal coverage, bases, tops, and albedo of these low clouds. For any given low cloud cover, there is an infinite variety of locations and configurations that clouds can assume within a given grid square. For the purposes of this paper, it was

Table 5.
Optical properties of cirrus

λD	ND	ℓ	r	SR	SN	$\tilde{\omega}_0$	$\beta_v(\text{km}^{-1})$	$\langle \cos \Theta \rangle$
0.7	0.5	100	10	0.29–1.50	1–12	0.9999	1.902	0.785
2.0	0.5	200	30	1.50–2.35	13–14	0.783	12.801	0.75
2.5	0.5	200	30	2.35–3.35	15	0.901	13.57	0.753
3.0	0.5	200	30	3.85–4.55	17,23,25	0.524	12.585	0.651
				12.50–1000.0				
3.5*	—	—	—	3.35–3.85	16,18,20	0.526	10.00	0.752
				4.55–5.50				
				6.50–9.50				
6.05*	—	—	—	5.50–6.50	19	0.535	0.407	0.804
10.0	.05	200	30	9.50–10.50	21	0.520	0.520	0.80
11.5	.05	200	20	10.50–12.50	22	0.545	0.546	0.758

*For these wavelengths, a gamma-size distribution was used (Liou, 1972). $\tilde{\omega}_0$ was obtained by graphical interpolation from Irvine and Pollack (1968) data for ice spheres. β_v and $\langle \cos \theta \rangle$ were estimates from tabular data.

KEY

λD : Defining wavelength (micrometers)
ND: Ice particle number density (cm^{-1})
 ℓ : Length of ice cylinder (micrometers)
r: Radius of ice cylinder (micrometers)
 $\langle \cos \theta \rangle$: Asymmetry factor

SR: Spectral range (micrometers)
SN: Spectral interval number
 $\tilde{\omega}_0$: Single scattering albedo
 β_v : Volume extinction cross section (km^{-1})

decided to use the cloud-free line-of-sight (CFLOS) probabilities as reported in Lund (1972). (The CFLOS probabilities were determined from several thousand infrared whole-sky photographs and visual sky cover observations. The photos were taken at Columbia, Missouri, every daylight hour, coincident with National Weather Service observations for a period exceeding 3 years. Pochop and Shanklin (1966) describe the capabilities of the infrared film and camera system.) Table 6 shows the probability, for a given elevation angle and sky condition, that the line-of-sight will be clear. For example, it shows that at an elevation angle of 40° there is a 71% probability of a CFLOS for a reported 5/10 sky cover. The probabilities are used in this paper to estimate the percent of direct and diffuse solar radiation coming through the open spaces between clouds. These CFLOS probabilities are the most accurate available. The radiation that impinges on low clouds undergoes absorption, reflection, and transmission. These processes are spectrally dependent and are discussed below.

The overall albedo of low clouds, which is specifically defined for reflection of spectral energy fluxes not affected by water vapor absorption, is 0.65. This low cloud albedo figure was chosen to conform to the theoretical findings of McKee and Cox (1974). In their study for cubic clouds of large optical depths, the total upward-directed reflected radiation (directional reflectance) varied between 0.56 and 0.69 for solar zenith angles between 0° and 60° . For the optical depths and thicknesses of Florida cumuli, an albedo of 0.65 should represent a realistic figure. It

does include the fraction of reflected incident radiation that strikes and leaves the sides of cumulus clouds. This chosen albedo of 0.65 is higher than the mean values for layer cloud obtained by Drummond and Hickey (1971). However, in their aircraft-derived data, the optical depths no doubt varied widely as they sampled from the equator to 50°N latitude. The corresponding absorptivity and transmissivity for clouds with this albedo of 0.65 are 0.20 and 0.15, respectively. These choices assume an optical thickness of 100. These selections were based on the findings of Danielson et al. (1969), who investigated the wavelength range between $0.45\ \mu\text{m}$ and $0.7\ \mu\text{m}$.

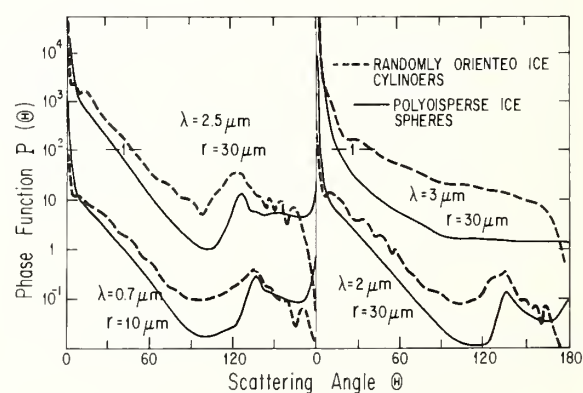


Figure 18. Phase function $P(\theta)$ as a function of scattering angle (θ) for $0.7\ \mu\text{m}$, $2\ \mu\text{m}$, $2.5\ \mu\text{m}$, and $3\ \mu\text{m}$. (K. N. Liou, 1973, *J. Geophys. Res.*, 78:1412, copyrighted by American Geophysical Union.)

Table 6.
Cloud-free line-of-sight probabilities

Zenith angle (degrees)	Elevation angle (degrees)	Sky cover (tenths)										
		0	1	2	3	4	5	6	7	8	9	10
0	90	1.00	.97	.92	.87	.81	.77	.70	.62	.48	.31	.08
10	80	.99	.97	.92	.87	.81	.77	.69	.61	.47	.31	.08
20	70	.99	.97	.91	.86	.80	.76	.68	.61	.47	.30	.08
30	60	.99	.96	.90	.85	.80	.75	.66	.60	.46	.29	.08
40	50	.99	.96	.90	.85	.78	.73	.64	.58	.45	.29	.08
50	40	.99	.95	.88	.83	.76	.71	.62	.55	.42	.27	.07
60	30	.98	.93	.86	.80	.73	.66	.57	.50	.38	.24	.06
70	20	.98	.90	.83	.75	.67	.59	.50	.42	.33	.21	.05
80	10	.97	.86	.76	.65	.55	.47	.39	.32	.24	.16	.03
90	0	.96	.82	.69	.56	.44	.38	.27	.17	.10	.05	.00

Albedo for low clouds is calculated separately for spectral energy fluxes affected by water vapor absorption. Details are given in Appendix A. No account is taken of short-wave direct and diffuse radiation reflected upward from low clouds back into the cloud-free atmosphere.

5.6 Long-Wave Radiation Transfer

Figure 19 is a schematic diagram that shows how the atmospheric streams of long-wave radiation are affected by the atmosphere and clouds. The long-wave radiation transfer routine used to determine the heating or cooling rates caused by this component in the prescribed layers and at the surface was developed by G. F. Watson (1971). The program was modified so that it could be successfully integrated into the total heating function. The modifications enable variable cirrus emissivities to be prescribed with the aid of a color densitometer (Appendix B). As originally formulated, the model treated cirrus, if it was present, as having 5/10 cloud cover in lieu of providing a technique for calculating variable emissivities. Watson's model absorptivity formulations for water vapor and carbon dioxide are those of Sasamori (1968). The Watson program was specifically designed to calculate radiation flux divergence and cooling rates in the vicinity of discontinuities, such as inversions. Therefore, some care is required in prescribing temperatures and mixing ratios in the vicinity of these discontinuities.

To enhance accuracy, the model (as adopted) adds levels if the temperature difference between two original levels exceeds 0.05°C. This is necessary as the integration of the product of the average absorptivity in a layer and the differential flux

is then more accurate if either quantity changes rapidly in a layer. Figure 20 compares cooling rates calculated and measured for a winter sounding. It can be seen that the calculated rates compare favorably with the observed rate, except at the top of the inversion. This inversion in the lower 100 mb is a feature of the applicable winter atmospheric sounding from which the three cooling rate profiles were derived. As Suomi et al. (1958) point out, the probable concentration of aerosols in this inversion layer caused measured cooling rates in excess of those that would be calculated from atmospheric data alone. This factor will result in noticeable deviation of calculated fluxes from those which would be measured when surface inversions or dust layers are present. In South Florida, daytime surface inversions generally occur only during the first hour after sunrise. However, African dust or continental pollution or haze layers often appear over South Florida in the summer and persist for as long as 4 days. The appropriate transfer processes for these events are not included in this model.

Shortly before completion of this work it was pointed out by Cox (1976, personal communication) that downward long-wave fluxes at the surface and cooling rates at the model levels were probably underestimates for the tropical atmospheres appropriate to this model study. The basis for this discrepancy lies in the presence of the water dimer molecule (Cox, 1973) in moisture-rich tropical atmospheres. This absorber is not a significant factor in midlatitude or polar atmospheres. Therefore, it must be recognized that model results are slightly different from those that would be obtained if the Colorado State University infrared radiation transfer algorithm (Cox, 1976, personal communication) were used.

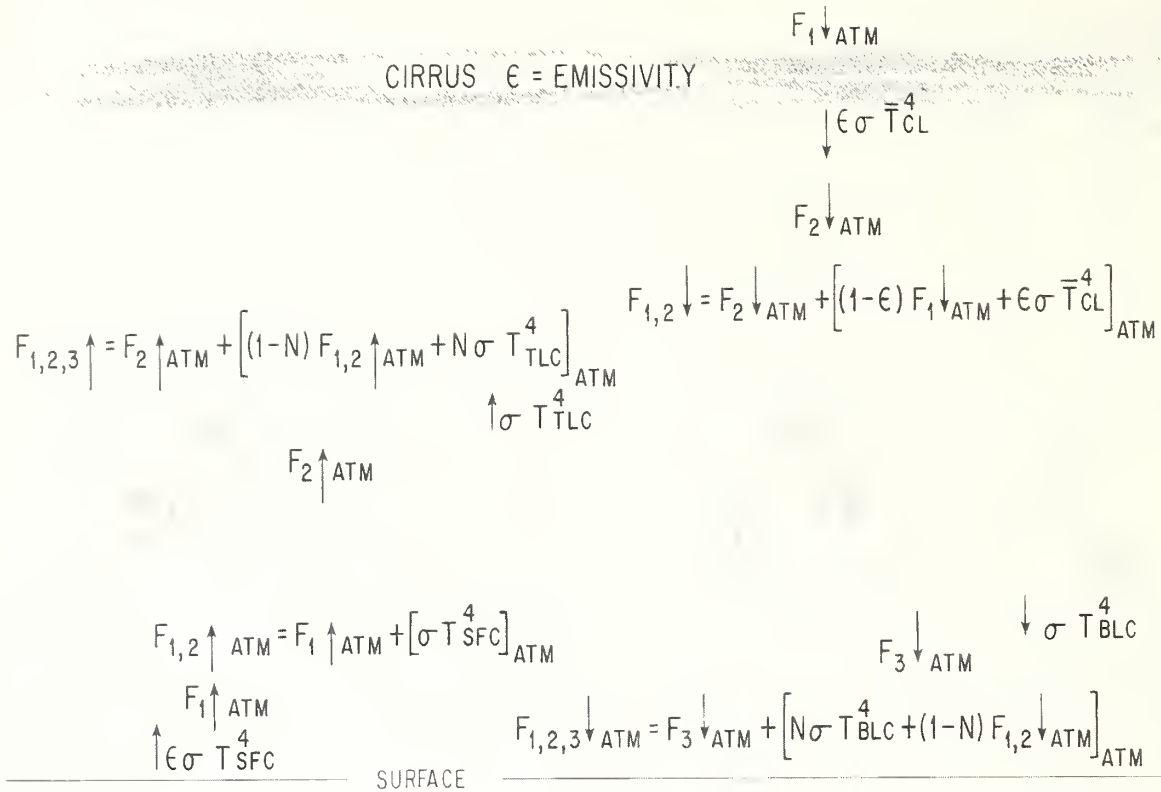


Figure 19. Long-wave radiation transfer. N is percent of low clouds. $F_{1,2,3} \downarrow_{\text{ATM}}$ and $F_{1,2,3} \uparrow_{\text{ATM}}$ are integrated downward and upward long-wave fluxes caused by water vapor and carbon dioxide. TLC refers to the top of low clouds and BLC to the base of low clouds. CL refers to the cirrus layer. The emissivity of low clouds is assumed to be unity although it is given the value 0.98 at the surface.

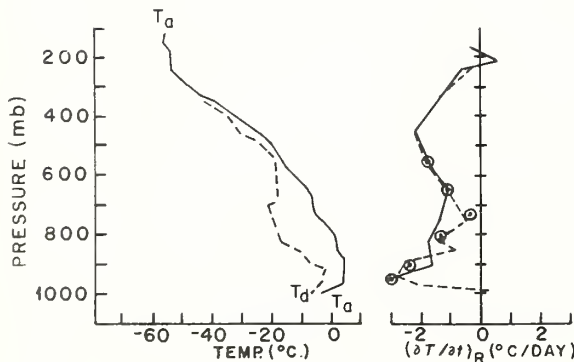


Figure 20. Comparison of cooling rates computed and measured for a winter sounding. Left: Sounding profiles (Fleagle and Businger, 1963). Right: Solid line is measured rate (Suomi et al., 1958). Dashed line is cooling rate computed by Fleagle and Businger. Circles are cooling rate computed from G. F. Watson (1971) program. (Base figure, from *Introduction to Atmospheric Physics*, R. G. Fleagle and J. A. Businger, with permission from the authors and from the copyright holder, Academic Press, N. Y.)

5.7 Surface Heating Method

The choice of the surface heat budget computation scheme was based upon the availability and simplicity of the empirical thermal inertia, albedo, and day-versus-night temperature difference relationship (Fig. 2). The computation scheme considers thermal inertia the sole ground surface layer parameter.

From Carslaw and Jaeger (1959), the temperature in a semi-infinite solid subjected to flux $f(t)$ per unit time per unit area at $z = 0$ and with the region $z > 0$ initially at constant temperature is

$$T = \frac{1}{\sqrt{\pi \kappa t}} \int_0^\infty f_0(L) e^{-\frac{L^2}{4\kappa t}} dL + \frac{1}{K} \sqrt{\frac{\kappa}{\pi}} \int_0^t f(t-\gamma) \frac{d\gamma}{\gamma^{1/2}}. \quad (21)$$

L and γ are dummy variables. $f_0(L)$ is initial vertical soil temperature profile, $f(t-\gamma)$ is incremental flux acting over $d\gamma$. κ is diffusivity, K the conductivity, and t is time. The quantity $\kappa^{1/2}K^{-1}$ is the same as the thermal inertia (TI). Near dawn (initial time), a near-perfect balance usually exists between downward atmospheric long-wave radiation and upward surface radiation. Under these conditions, the initial soil temperature profile (f_0) can be considered constant.

By treating the net flux f as constant at each time step, (21) can be written as

$$T_{\text{sfc}}^{n+1} = T_{\text{sfc}}^n + \frac{2f^{n+1}}{\text{TI}} \left(\frac{\Delta t}{\pi} \right)^{1/2}. \quad (22)$$

T_{sfc}^{n+1} is the temperature at the next time step $n+1$, T_{sfc}^n is the initial temperature at the current time step, and f^{n+1} is the net flux across the air-ground interface which is considered constant over Δt .

This is a simpler form than that employed by Shaffer and Long (1975). They indicate that the difference between this formulation and that resulting from the assumption that net flux is linear in time is small. A basic difference is that the temperatures determining the fluxes of evaporation, sensible heat, and upward surface radiation are iteratively determined in their model. In the present work, the temperatures determining these fluxes are those at the last time step. The net flux formulation is:

$$f^{n+1} = Rg + Id + E^n + S^n - I_u \text{ (cal cm}^{-2} \text{ s}^{-1}). \quad (23)$$

These fluxes are defined as follows:

1) Rg —Total direct and diffuse radiation going into the surface layer. This is recomputed every 30 min.

2) Id —Total downward long-wave radiation. This is recomputed every 30 min.

3) $E^n = \rho L u_* q_*$ (evapotranspiration). ρ is atmospheric density, L the latent heat of condensation, u_* the friction velocity, and q_* the friction specific humidity. The temperature at time step n is used to define E^n .

4) $S = \rho C_p u_* \theta_*$ (sensible heat flux). C_p is the specific heat of air at constant pressure; θ_* is the friction temperature. The temperature at time step n is used to define S .

5) $I_u = \epsilon \sigma (T_{\text{sfc}}^n)^4$ (surface radiation flux); $\epsilon = 0.98$ (surface emissivity); $\sigma = 1.3533 \times 10^{-12}$ cal $\text{cm}^{-2} \text{ deg}^{-4} \text{ s}^{-1}$ (Stefan-Boltzmann constant).

The heat balance formulation is based upon the assumption that during each time step f is constant. The assumption is reasonable in view of the smallness of the time step (about 60 s). The short-

and long-wave fluxes are recomputed every half hour.

5.8 Model Domain and Grid Spacing

The model domain is a Cartesian grid having 33 grid points along the x (east-west) direction and 7 grid points along z . Figure 21 shows the two-dimensional model domain. This grid is located along $26^\circ 30' \text{N}$. This latitude line passes south of Fort Myers, Florida, on the west coast and near Delray Beach on the east coast. Grid spacing is unchanged from that of Pielke (1974), i.e.,

$$\begin{aligned} x(i-1) + 55 \text{ km} - (i-2) \\ \times 11 \text{ km} \end{aligned} \quad (2 < i < 5)$$

$$\begin{aligned} x(i) = x(i-1) + 11 \text{ km} \quad (6 \leq i \leq 29) \\ x(i-1) + 55 \text{ km} - (33-i) \end{aligned}$$

$$\times 11 \text{ km} \quad (30 \leq i \leq 33) \quad (24)$$

To prescribe land and water coverage, urban and rural coverage, average values of albedo, thermal inertia, soil moisture, and cloud cover, each grid point is centered on an 11×11 km grid square within which coverages and averages apply.

There are seven levels in the vertical where wind, pressure, and vertical motion are defined. The vertical grid for these levels is given by

$$\begin{aligned} j \times 50 \text{ m} \quad (1 \leq j \leq 2) \\ z(j) = 1.22 \text{ km} + (j-3) \times 600 \text{ m} \quad (3 \leq j \leq 5) \\ 3.62 \text{ km} \quad (j=6). \end{aligned} \quad (25)$$

The seventh level is a material surface with an initial height of 4.82 km. Potential temperature and moisture are defined at the roughness height (z_0), at levels intermediate between the levels in (25) and at 4.82 km.

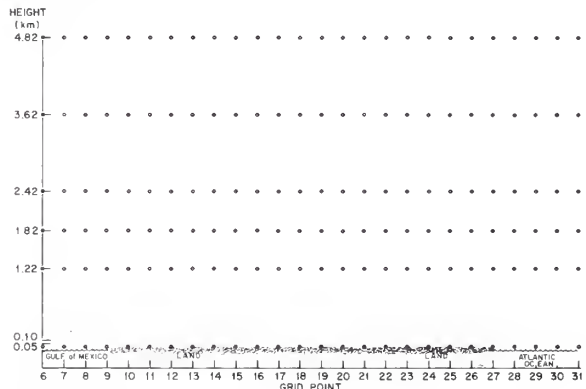


Figure 21. Outline of model grid.

5.9 Initialization of the Model

Characteristically, 1200 GMT Miami and Tampa soundings show the presence of an early morning surface inversion. The inversion, too, is usually found in the vicinity of 1000 mb. In the interior of the state, ground surface and shelter temperatures at daybreak are about 22°C (Section 4). The 1000-mb temperature is about 26°C. Therefore, it takes 2 to 3 hours (with minimum cloud cover) for the surface layer to attain a neutrally stratified state, the state defined as the initial state in the original model (Pielke, 1974). For numerically simulating a diurnal heating cycle from sunrise to late afternoon in which an actual observed 1200Z (0800 EDT) sounding is used to define initial conditions, certain adjustments are made to the sounding. The surface potential temperature over land is set equal to the prescribed sea surface potential temperature and the layer from the surface to 75 m is prescribed as adiabatic. This sounding defines the entire domain (land and sea) as having the same atmospheric structure with an initially neutrally stratified surface layer. This procedure is consistent with the requirement that a steady-state equilibrium exist over the domain at $t = 0$. However, it means that the initial time must be set from 6 to 10 hours before sunrise. This allows for slow surface radiational cooling to commence, the land breeze to be established, and an inversion to be present at sunrise.

This procedure was followed in the case of numerical sensitivity experiments (Section 6). It was found that with a very light synoptic-scale wind (1.5 m s^{-1}), unrealistic oscillations in the results were obtained when $t = 0$ at sunrise and the surface layer was initially stable. This nonlinear instability probably has its origin in the rather rapid heating that takes place with light winds over a few selected grid points. This heating is not compatible with the initial conditions prescribed in this way. Pielke (1974) states that heating must be introduced slowly. For basic wind flows at 3 m s^{-1} or higher, it made no obvious difference if the former initializing procedure was used or if the initial conditions were based on the early morning sounding with a marked inversion and the initial time was set at sunrise.

Pressure, temperature, mixing ratio, and height data are extracted from the basic Miami 1200 GMT sounding used to define the initial state. Twenty-two levels are prescribed, the first being the surface and the topmost level being 100 mb. In addition to the surface and the 7 Pielke model levels, 14 additional levels are prescribed. These additional levels are included solely for the pur-

pose of more accurate and efficient calculation of short- and long-wave fluxes. The data of these special levels are not dynamically predicted as they are at the Pielke levels, but are redefined by simple interpolation with a special subroutine. The top six levels are constant pressure levels where temperature and moisture are treated as invariant. A special subroutine redefines the values of potential temperature and moisture at the intervening levels by simple interpolation (except levels 17–22 where values are constant). The role of these 14 additional levels is explained further in Section 5.10.

5.10 Computational Sequence

The sequence in which model equations are integrated in time is given in Pielke (1974). Short- and long-wave fluxes are calculated at prescribed intervals during the computations without altering this basic sequence. The addition of the heating function routines to the two-dimensional version necessitated the addition of 4184 words of memory to the 3190 words already in the basic program.

Figure 22 shows the order in which computations are performed. Solar and infrared radiation computations are performed on the half hour. The solar zenith angle is that which exists on the quarter hour. For example, if $t = 3600$ seconds (0730 EST), the solar zenith angle is calculated for $t = 4500$ seconds (0745 EST). This procedure keeps the total solar heating over the half hour in line with that which would be obtained with calculations of greater frequency. The infrared fluxes, which change much more slowly, are based upon temperature, moisture, and pressure fields existing on the half hour (e.g., 0730 EST). Modeling of radiation fields at hourly intervals was considered, but rejected for two reasons. An important objective of this study is to determine the impact of variable and oftentimes rapidly changing cloud patterns on the radiation fields which, in turn, affect the motion fields. Also, the Pielke model remains computationally stable as heating is introduced relatively slowly. By changing from clear to partly cloudy to cloudy conditions in two steps rather than one, this possible source of instability is avoided.

Subroutine UPDATE redefines, at each grid point, the temperature and moisture values in the vertical. This is done before the radiation calculations for that grid point. Subroutine OZONE is always called, but subroutine CIRRUS is bypassed if cirrus is not present. If low clouds are absent, subroutine THRCAT (called by subroutine SOLRAD) by-

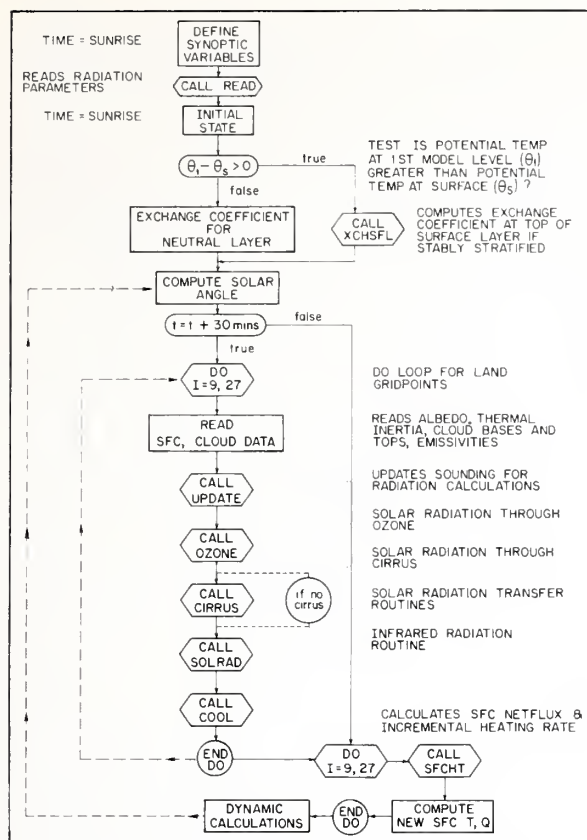


Figure 22. Order in which computations are performed.

passes the complex in-cloud radiation transfer computations. Subroutine COOL is always called. At the end of the radiation computations, surface heating and dynamic calculations at the appropriate time step are carried out. When 30 min of real time have elapsed, the cycle begins again with a new radiation calculation.

5.11 Summary

The two-dimensional improved primitive equation numerical model contains recent surface and boundary layer formulations validated by field experiments. With the inclusion of complete radiation and heat budget physics, the model is capable of evaluating the magnitude of the changes in sea breeze location and intensity which result from changes in surface thermal properties and clouds. The surface heat budget formulation based on the thermal inertia is effective and does not require explicit evaluation of subsurface fluxes. At the initial time (0530 EST), a surface inversion is present. This initially stable surface layer is modified by solar and atmospheric infrared radiation. Both are updated every half hour on

the basis of the solar zenith angle and atmospheric temperature and water vapor. Atmospheric heating resulting from absorption of short- and long-wave radiation is also taken into account in the model.

6. NUMERICAL EXPERIMENTS

Results of numerical experiments conducted to determine sea breeze response to heating patterns resulting from differences in surface properties and clouds are presented in this section. The effects of surface albedo, surface thermal inertia, surface soil moisture, and cirrus clouds on sea breeze intensity and location are shown in a systematic manner with sensitivity experiments. In this way, the surface and cirrus cloud properties are ordered according to their relative importance. Following this, results from a case study of the sea breeze of July 16, 1975, are presented. This case study is to be considered a special type of sensitivity experiment in which observed surface and cumulus cloud properties are prescribed.

Thermal inertial values based upon the observations gathered over South Florida range from 0.05 to 0.30 cal s^{-1/2} cm⁻² °C⁻¹; albedo ranges from 5% to 30%. Soil moisture values based upon daily water-budgeting computations (Appendix C) and research by agricultural agencies, can, depending upon soil type, range between zero and that amount corresponding to field capacity for a given soil type (expressed as cm³ of water per cm³ of soil). Thus, the relative humidity at the soil-surface-atmosphere interface can range from zero to 100%. The condition of zero soil moisture is relatively infrequent; thus some higher and more conservative minimum is assumed for most of the sensitivity experiments.

Cirrus properties are prescribed so that the effects of thin, medium, and thick cirrus can be demonstrated. The categories are defined by the following properties:

Cirrus Classification	Geometric Thickness (km)	Emissivity
Thin	0.2	0.1
Medium	1.0	0.38
Thick	2.0	0.6

Figure A-1 (Appendix A) was used to obtain emissivity as a function of the chosen value of geometric thickness.

All experimental results pertain to the two-dimensional (x,z) plane having its x-axis along 26°30'N across the Gulf of Mexico, the Florida peninsula, and the Atlantic Ocean.

The purpose of the sensitivity experiments (excluding the case study) is to analyze sea breeze behavior in the absence of cumuliform cloudiness. To achieve as much consistency as possible in experimental design and to retain as much realism as possible in the results, initialization of the model is based on a vertical sounding structure that is compatible with this purpose. A very dry, stable, and suppressed synoptic situation was selected. Only widely scattered shallow cumulus clouds were observed over most of Florida.

The Miami 1200 GMT sounding for August 24, 1975 (fig. 23), defines the synoptic state for the initialization of the sensitivity experiments. The observed winds were 5 m s^{-1} on the surface, increasing to 10 m s^{-1} at 500 mb. The direction was easterly and therefore parallel to the two-dimensional (x,z) plane. As sea breeze intensity was anticipated to intensify with decreasing wind speeds,

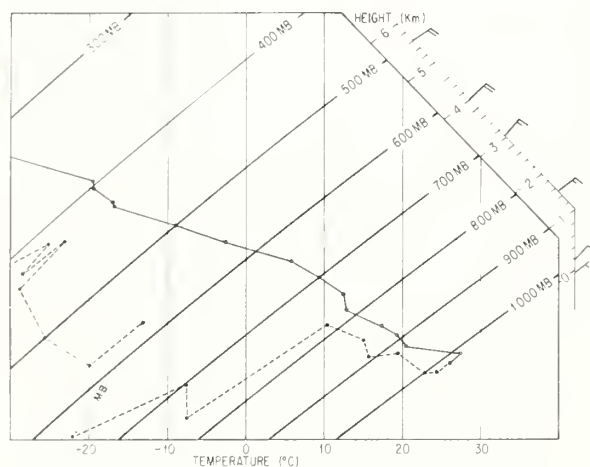
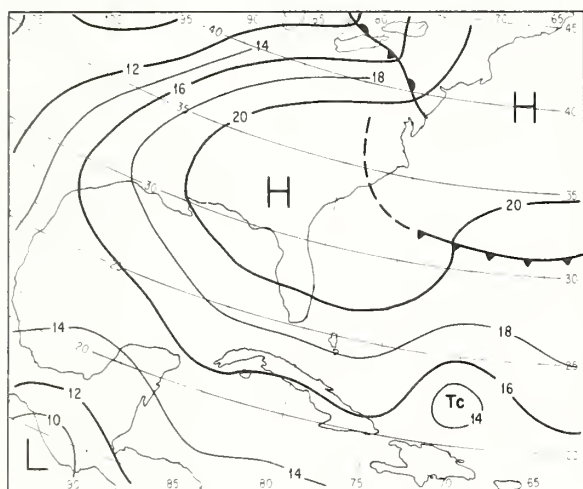


Figure 23. Prevailing meteorological conditions on August 24, 1975, in the vicinity of South Florida. Above: Surface weather map analysis at 1200 GMT. Below: Upper air sounding for 1200 GMT, Miami, Florida.

the observed winds were not used in the sensitivity experiments. For the more interesting, lighter wind conditions, two separate and weaker easterly flow regimes were specified and the experimental results stratified by these regimes. Also, a solar declination angle corresponding to July 1 was chosen. This provides an opportunity to analyze sea breeze response to maximum solar radiation forcing. It is stressed that interpretation of the experimental results must be guided by the knowledge that clouds are not prescribed nor allowed to develop as a result of the sea breeze circulations. Cloud development over Florida near highly heated surfaces is very likely with light winds, regardless of vertical sounding structure. Once initiated, the clouds shield the surface either partially or completely and reduce or reverse the heating rate. Precipitation would result in significant surface cooling.

The surface weather map for 1200 GMT (fig. 23) shows the synoptic conditions for these experiments. South Florida is seen to be under the influence of a high pressure center over southern Georgia. The pressure gradient produced surface winds over South Florida from 5 to 7 m s^{-1} during the day. On the basis of the exceptionally dry, clear, and windy conditions that were noted (see sounding), it is expected that large-scale descending motion occurred during this time. This is not accounted for in the model, which assumes zero large-scale vertical motion. Satellite and radar observations show that a rapidly moving east coast sea breeze line was generated which produced a weak scattered-to-broken line of moderate towering cumulus on the west coast in late afternoon.

6.1 Design of Experiments

The five types of sensitivity experiments are described below.

1) Systematic Variations of Surface Properties Uniformly and Singly Prescribed for All Land Grid Points.

Numerical values of surface properties are systematically varied one at a time while being uniformly prescribed for all land surface grid points. These experiments provide the basic measure of the relative importance of the surface properties. They were conducted to analyze the influence of variable surface albedo, surface thermal inertia, and surface soil moisture under two basic easterly wind flows used to initialize the model. These flows have wind speeds of 1.5 m s^{-1}

Table 7.

Experiment design; sea breeze response to systematic horizontal variations of surface properties uniformly and singly prescribed for all grid points

Exp. No.	Experiment	Surface thermal inertia	Surface albedo (%)
EASTERLY WIND, 1.5 m s^{-1}			
1	Low albedo	0.10	5.0
2	High albedo	0.10	25.0
3	Low TI	0.05	10.0
4	High TI	0.25	10.0
	Sinusoidal	—	—
EASTERLY WIND, 3.0 m s^{-1}			
5	Low albedo	0.10	5.0
6	High albedo	0.10	25.0
7	Low TI	0.05	10.0
8	High TI	0.25	10.0
	Sinusoidal	—	—

NOTE: Surface relative humidity = 85%.

Sea surface temperature = 300.56 K. No clouds.

Thermal inertia is in $\text{cal s}^{-1/2} \text{ cm}^{-2} \text{ }^{\circ}\text{C}^{-1}$.

For the sinusoidal experiments, prescribed surface temperature amplitude is 15°C .

(light wind) and 3.0 m s^{-1} (medium wind), respectively. No vertical wind shear is permitted in these experiments. Also, clouds are not prescribed.

To make meaningful comparisons, soil moisture (expressed as surface relative humidity at the interface) in this first experimental set is given a minimum value of 75%. This is probably representative of the minimum value that would commonly occur over the undeveloped regions of Florida, although it can be vanishingly small on occasion. Thus, when albedo is allowed to vary from 5% to 25%, thermal inertia from 0.05 to $0.25 \text{ cal s}^{-1/2} \text{ cm}^{-2} \text{ }^{\circ}\text{C}^{-1}$, and soil moisture from 75% to 95%, the normal range of surface properties is being examined.

Table 7 presents the experimental design for analysis of the relative importance of surface thermal inertia and surface albedo. This analysis is conducted for the two basic easterly wind regimes of 1.5 m s^{-1} and 3.0 m s^{-1} . Included in each wind category is an experiment in which the sinusoidal heating function is used to prescribe the surface temperature. In this formulation the initial surface temperature is the sea surface temperature of 300.56 K, the maximum surface temperature of 315 K is reached at or near local noon, and the minimum is again attained about 1830 local time.

Table 8 presents the experimental design for analysis of the relative importance of surface soil moisture amounts. These experiments are stratified by light and medium wind speeds. The sinusoidal heating experiments are included as in table 7.

Table 8.

Experiment design; sea breeze response to variations in soil moisture applied uniformly along x-axis

Exp. No.	Experiment	Soil Moisture (%)
EASTERLY WIND, 1.5 m s^{-1}		
9	Low SM	75.0
10	High SM	95.0
	Sinusoidal	—
EASTERLY WIND, 3.0 m s^{-1}		
11	Low SM	75.0
12	High SM	95.0
	Sinusoidal	—

NOTE: Surface thermal inertia = $0.15 \text{ cal s}^{-1/2} \text{ cm}^{-2} \text{ }^{\circ}\text{C}^{-1}$.

Surface albedo = 15%.

Sea surface temperature = 300.56 K. No clouds.

Soil moisture is expressed as surface relative humidity.

For the sinusoidal experiments, prescribed surface temperature amplitude is 15°C .

2) Systematic Variations of Surface Properties Uniformly and Singly Prescribed for Coastal Zones.

Numerical values of surface properties are systematically varied one at a time while being uniformly prescribed for three land grid points on the east coast and three land grid points on the west coast. Interior grid point values are held constant.

Table 9 presents the experimental design for analysis of the relative importance of surface albedo, thermal inertia, and soil moisture when horizontal variations are imposed at coastal zones. At grid points 10–12 and 24–26, variations are uniformly and singly prescribed while interior values remain constant. The purpose of these experiments is to analyze the effect of changes on a scale comparable with the width of developed regions on both coasts of Florida. The same wind stratification applies as in type 1 above.

3) Systematic Variations of Surface Properties Uniformly and Simultaneously Prescribed for Coastal Zones.

Numerical values of thermal inertia and soil moisture are simultaneously varied while being uniformly prescribed for three land grid points on the east coast and three land grid points on the west coast. Interior grid-point values are held constant. These experiments are performed only for the medium wind speed case.

Table 9.

Experiment design; sea breeze response to systematic horizontal variations of surface properties, uniformly and singly prescribed for coastal zones

Exp. No.	Experiment	Surface Soil Moisture (%)			Surface Thermal Inertia			Surface Albedo (%)		
		Grid Points			Grid Points			Grid Points		
		10-12	13-23	24-26	10-12	13-23	24-26	10-12	13-23	24-26
EASTERLY WIND. 1.5 m s ⁻¹										
13	Coastal low albedo	85.0	85.0	85.0	0.10	0.10	0.10	5.0	25.0	5.0
14	Coastal low TI	85.0	85.0	85.0	0.05	0.25	0.05	10.0	10.0	10.0
15	Dry coasts	75.0	95.0	75.0	0.15	0.15	0.15	15.0	15.0	15.0
	Sinusoidal	—	—	—	—	—	—	—	—	—
EASTERLY WIND. 3.0 m s ⁻¹										
16	Coastal low albedo	85.0	85.0	85.0	0.10	0.10	0.10	0.05	0.25	0.05
17	Coastal low TI	85.0	85.0	85.0	0.05	0.25	0.05	0.10	0.10	0.10
18	Dry coasts	75.0	95.0	75.0	0.15	0.15	0.15	0.15	0.15	0.15
	Sinusoidal	—	—	—	—	—	—	—	—	—

NOTE: Sea surface temperature = 300.56 K. No clouds.

Thermal inertia is in $\text{cal s}^{-1/2} \text{ cm}^{-2} \text{ }^{\circ}\text{C}^{-1}$.

Soil moisture is expressed as surface relative humidity.

For the sinusoidal experiments, prescribed surface temperature amplitude is 15°C .

Table 10 presents the experimental design for analysis of the effect of lowering soil moisture and thermal inertia simultaneously at coastal zones. For these experiments, surface relative humidity is allowed to attain a minimum value of 25%, a value representative of a heavily developed region with minimum soil and vegetation. These experiments, conducted only for the medium wind case, will (1) reveal if thermal inertia changes are important when soil moisture contents are low (but not vanishingly small), (2) reveal if heating on the scale of developed coastal zones (e.g., 33 km) produces a sea breeze response comparable with that of the light wind case, and (3) suggest the maximum sea breeze response to be expected if green areas (parks, fields, gardens, etc.) are almost eliminated on the coasts through urbanization.

4) Systematic Variations of Cirrus Cloud Optical Properties Uniformly Prescribed for All Land Grid Points.

Numerical values of cirrus cloud geometric thickness and emissivity are systematically varied while being uniformly prescribed for all land surface grid points. All experiments are for the medium wind case. They provide the basic measure of the relative influence of cirrus properties and show the importance of cirrus cloud cover in influencing sea breeze intensity. Table 11 presents the experimental design for analysis of the effect of prescribing cirrus cloud cover uniformly over all land grid points.

Table 10.

Experiment design; sea breeze response to systematic horizontal variations of surface properties uniformly and simultaneously prescribed for coastal zones

Exp. No.	Experiment	Surface Soil Moisture (%)			Surface Thermal Inertia			Surface Albedo (%)		
		Grid Points			Grid Points			Grid Points		
		10-12	13-23	24-26	10-12	13-23	24-26	10-12	13-23	24-26
EASTERLY WIND, 1.5 m s ⁻¹										
19	Coastal low SM and TI	25.0	95.0	25.0	0.05	0.15	0.05	15.0	15.0	15.0
20	Coastal low SM and TI	25.0	95.0	25.0	0.25	0.15	0.25	15.0	15.0	15.0
	Sinusoidal	—	—	—	—	—	—	—	—	—

NOTE: Sea surface temperature = 300.56 K. No clouds.

TI is thermal inertia in $\text{cal s}^{-1/2} \text{ cm}^{-2} \text{ }^{\circ}\text{C}^{-1}$.

Soil moisture is expressed as surface relative humidity.

For the sinusoidal experiment, prescribed surface temperature amplitude is 15°C .

Table 11.
Experiment design; sea breeze response to systematic horizontal variations in cirrus cloud optical properties uniformly prescribed for all land grid points

Exp. No.	Experiment	Geometric Thickness (km)	Emissivity
EASTERLY WIND, 3 m s^{-1}			
21	Thin cirrus	0.2	0.1
22	Medium cirrus	1.0	0.38
23	Thick cirrus	2.0	0.6

NOTE: Sea surface temperature = 300.56 K.
Thermal inertia is $0.15 \text{ cal s}^{-1/2} \text{ cm}^{-2} \text{ }^{\circ}\text{C}^{-1}$.
Surface albedo = 15%.
Soil moisture (expressed as surface relative humidity) = 85%.

5) Systematic Variation of Thick Cirrus Cloud Optical Properties Uniformly Prescribed for Interior and Coastal Zones.

Numerical values of cirrus cloud geometric thickness and associated emissivity are systematically varied while being uniformly prescribed for selected zones of the study area. In one experimental design, cirrus properties are prescribed for seven grid points on the east coast and seven grid points on the west coast. Interior grid points are cloud-free. In the other experimental design, cirrus properties are prescribed at 10 grid points in the interior with coastal sections remaining cloud-free. The experiments are stratified by light and medium wind speeds. These experiments provide an indication of the sea breeze response that will occur when the peninsula is partially covered by cirrus. It also suggests the type of response that

could be expected with weather modification techniques suggested by Gray et al. (1974).

Table 12 presents the experimental design for analysis of the effect of prescribing thick cirrus cloud cover uniformly at selected interior and coastal segments.

The last heat budget experiment is a case study of the sea breeze of July 16, 1975. This case study is in reality a special sensitivity experiment. The relative importance of the surface properties and clouds that were observed on this day is analyzed through this case study.

In addition to the experiments discussed thus far, three additional experiments were conducted. These were wind-stratified experiments in which a sinusoidal heating function was used to prescribe the surface daytime temperature profile. This particular method of thermal forcing is representative of the heating functions employed in previous theoretical sea breeze studies. It was employed by Pielke (1974) originally, but is being replaced by him with a heat budget and radiation function of a form different from that discussed in this paper (Pielke, 1976, personal communication).

All experiments will be compared with each other in various ways to establish the relative importance of the surface and cloud properties. It is also very important that the sensitivity experiments be compared with the sinusoidal experiment as well as with each other. This proviso is made because the heat budget and sinusoidal experiments differ in the manner in which the air interacts with the surface. The heat budget formulation allows the heat to be transferred to the air and to cool the land surface (Pearson, 1973) in certain regions; in other regions the surface heating is intensified by a reduction in the sensible and latent

Table 12.
Experiment design; sea breeze response to systematic horizontal variations in thick cirrus cloud optical properties uniformly prescribed for selected interior and coastal zones

Exp. No.	Experiment	Geometric Thickness (km)			Emissivity		
		Grid Points			Grid Points		
		9-15	16-21	22-27	9-15	16-21	22-27
EASTERLY WIND, 1.5 m s ⁻¹							
24	Interior cirrus	—	2.0	—	—	0.6	—
25	Coastal cirrus	2.0	—	2.0	0.6	—	0.6
	Sinusoidal	—	—	—	—	—	—
EASTERLY WIND, 3.0 m s ⁻¹							
26	Interior cirrus	—	2.0	—	—	0.6	—
27	Coastal cirrus	2.0	—	2.0	0.6	—	0.6
	Sinusoidal	—	—	—	—	—	—

NOTE: Sea surface temperature = 300.56 K.
Thermal inertia = $0.15 \text{ cal s}^{-1/2} \text{ cm}^{-2} \text{ }^{\circ}\text{C}^{-1}$.
Albedo = 15%.
Soil moisture (expressed as surface relative humidity) = 85%.
For the sinusoidal experiments, the prescribed surface temperature amplitude is 15°C .

heat fluxes from the surface. The effect is to increase the intensity of the descending and rising branches of the sea breeze circulation.

The format of the results is given by (1) plots of the deviation of land surface temperature (ΔT) from the 0600 EST value valid at 1400 EST, (2) plots of vertical motion w (cm s^{-1}) at 1200 m valid at 1400 EST, (3) selected representative plots of the vertical motion w (cm s^{-1}) and vertical mass flux (M) at 1200 m valid at 1600 EST as a function of time and horizontal coordinate, (4) tables summarizing the results in terms of the vertical mass flux and (5) special diagnostic displays of model results (heat budget components of evaporation, sensible heat, solar flux, upward IR flux, and downward IR flux). The case study will include profiles of heating caused by radiative and diffusive effects, radar echo displays, and streamline analyses which will be related to surface convergence zones.

The vertical mass flux, which is a measure of sea breeze intensity, is calculated for the west and east coast sea breeze zones across the peninsula at 1220 m. It is defined as:

$$M = \int_0^{\infty} \rho w dx \quad (w > 0) \quad (\text{g cm}^{-1} \text{ s}^{-1})$$

where w is vertical motion in cm s^{-1} , ρ is density, and x is distance. M is a measure of the total mass overturning within an organized sea breeze upward motion regime. Although M is a more precise measure of sea breeze intensity, upward vertical motion in the case of the ascending vertical motion regime is also a reliable indicator. Figure 24 shows the relationship between M and vertical motion w in the core at a height of 1220 m. This relationship allows the intensity to be ascertained with reasonable accuracy from the core value of w .

6.2 Results: Systematic Variations of Surface Properties Uniformly and Singly Prescribed for All Land Grid Points

Figures 25 and 26 compare the experiments listed in table 7. For the light wind case shown in figure 25, it is seen that the heat budget surface temperature deviations (ΔT) are less than the sinusoidal, except for grid point 10. On the east coast, the advection of cooler sea air results in an increase of sensible and latent heat loss from the surface which cools the surface here more than on the

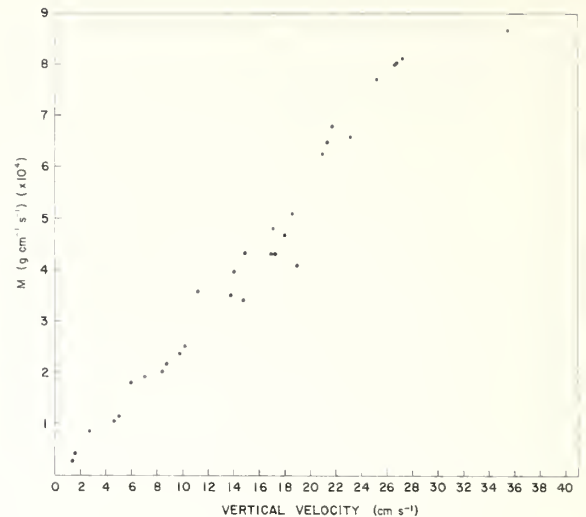


Figure 24. Relationship between vertical mass flux (M) and vertical motion (w) in sea breeze convergence zone core at 1220 m.

west coast. This increase results in the large difference (approximately 7°C) between the temperatures predicted from the sinusoidal forcing and from the heat budget. On the west coast, the advection of air with higher virtual temperature results in a decrease in sensible and latent heat fluxes from the surface. This interaction with the surface produces higher surface temperatures where the west coast convergence zone is located. The pattern is realistic. Surface temperatures (approximately 50°C) of this magnitude have been measured on cross-peninsula flights (e.g., fig. 14). However, this particular pattern with the large amplitude associated with a single spike has not been observed. The natural consequence of this heating in a convergence zone is to produce cloudiness and rain which would reduce this temperature excess. It is also likely that the formulations for heat transfer in the surface and boundary layer are not effective in removing surface layer heat in the very light winds (approaching zero) at grid point 10. These considerations do not preclude the drawing of conclusions concerning the difference between heat budget and sinusoidal experiments and the relative importance of surface properties for the light wind case.

The importance of surface albedo is clearly shown in figure 25. An increase in surface albedo from 5% to 25% results in an approximate 2°C decrease in surface temperature across the peninsula. An increase in thermal inertia from 0.05 to 0.25 has almost no influence on surface temperature. If soil moisture amounts were very low (e.g., surface relative humidity less than 25%), then

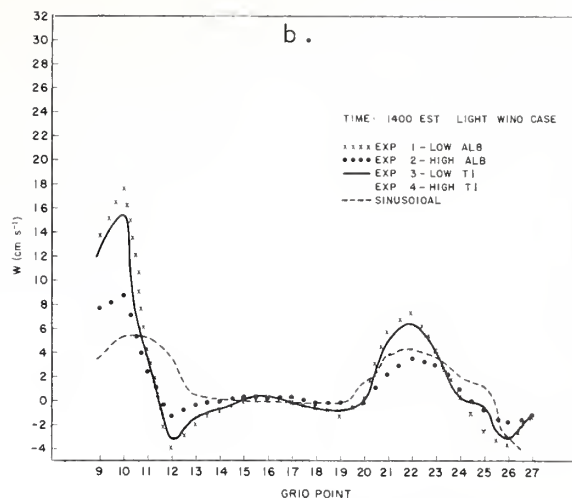
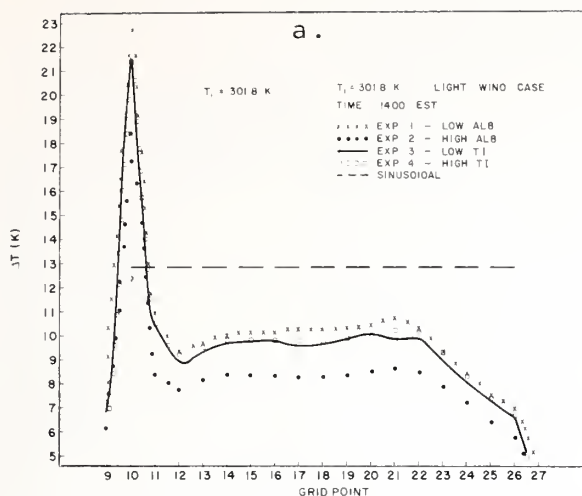


Figure 25. Comparison of albedo and thermal inertia for light wind cases (surface properties uniformly and singly prescribed for all land grid points). (a) Deviation (ΔT) of land surface temperature from 0600 EST value. (b) Vertical motion (w) at 1220 m.

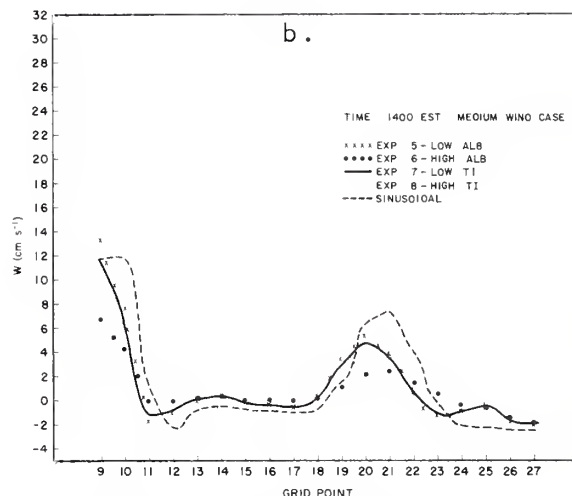
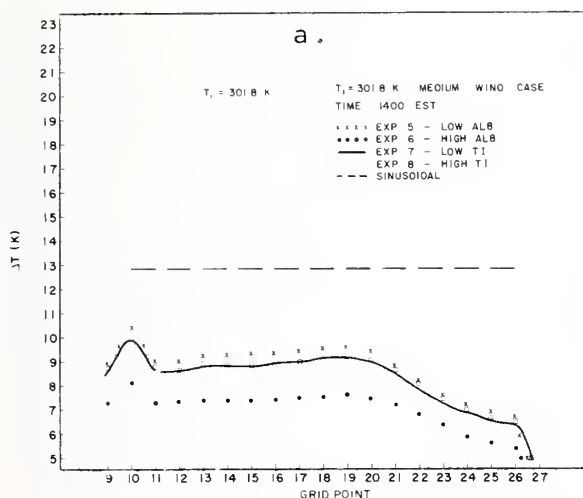


Figure 26. Comparison of albedo and thermal inertia for medium wind case (surface properties uniformly and singly prescribed for all land grid points). (a) Deviation (ΔT) of land surface temperature from 0600 EST value. (b) Vertical motion (w) at 1220 m.

these thermal inertia changes would result in significant temperature differences (Pohn et al., 1974). In these experiments, soil moisture is prescribed with 85% surface relative humidity. These results suggest that where soil moisture is moderately high, it makes little difference what the thermal inertia is.

Figure 25b shows the sea breeze response in vertical motion (w) to the surface property variations. The profiles of w for the heat budget experiments differ from w profiles in the sinusoidal version. The profiles are more concentrated and are

generally of greater amplitude than the sinusoidal case. The heat budget formulation permits variations in surface temperature. This differential heating is communicated to the lower atmosphere and is reflected in higher temperature gradients. More intense sea breeze convergence zones result from this process. It is suggested that this sea breeze response is associated with the organized and intense convection often seen over South Florida on light wind days. As in the ΔT profiles, the differences are largest between the albedo cases of 5% and 25%.

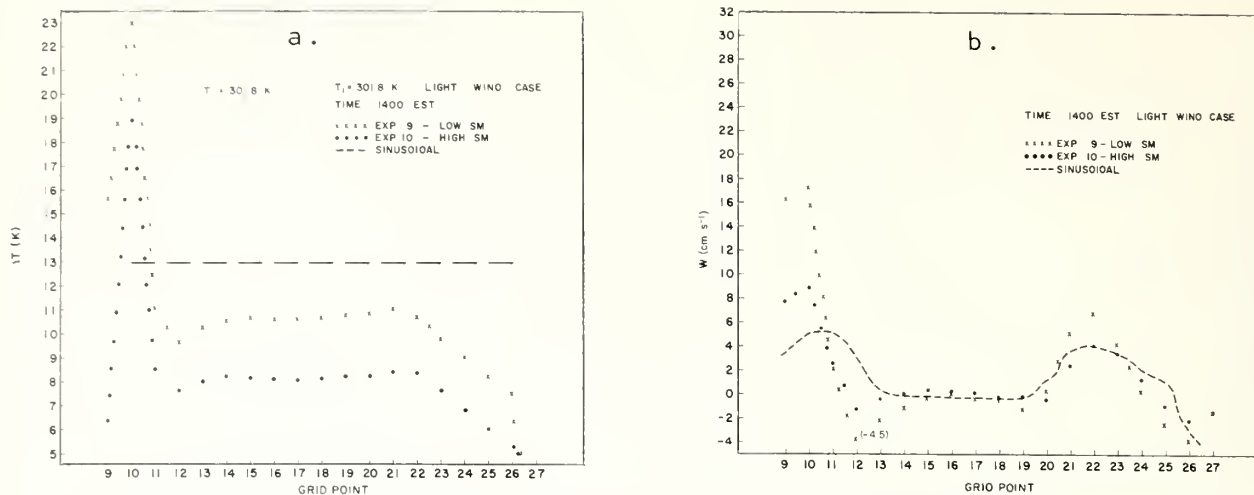


Figure 27. Comparison of soil moisture amounts for light wind case (surface properties uniformly and singly prescribed for all land grid points). (a) Deviation (ΔT) of land surface temperature from 0600 EST value. (b) Vertical motion (w) at 1220 m.

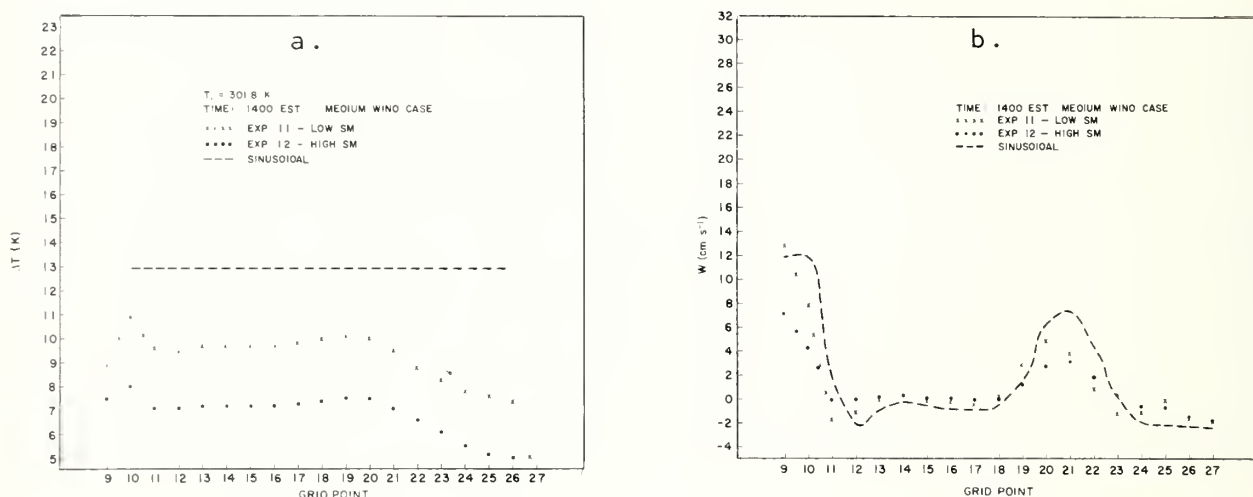


Figure 28. Comparison of soil moisture amounts for medium wind case (surface properties uniformly and singly prescribed for all land grid points). (a) Deviation (ΔT) of land surface temperature from 0600 EST value. (b) Vertical motion (w) at 1220 m.

Figure 26 shows the ΔT and w profiles for the medium wind speed case. The ΔT pattern is similar to the light wind case on the east coast, but the magnitude is far less on the west coast. As the westward-moving airstream spends less time over the heated land surface, the air incorporated into the west coast convergence zone acquires less sensible heat input from the surface. The difference in ΔT resulting from albedo changes is similar to the difference in the light wind case.

Unlike the light wind case, the w profile from the sinusoidal version has equal or greater ampli-

tude than the w profiles from the heat budget version. This is a trend opposite to that shown by the heat budget w profiles. The w maxima are shifted westward from the light wind case. Again, the difference in surface albedo exerts the greatest influence.

Figures 27 and 28 provide the comparisons between soil moisture experiments shown in table 8. For the light wind case, major differences are seen between the ΔT profiles for the low (75% surface RH) and high (95% surface RH) cases. The same characteristic differences between the heat

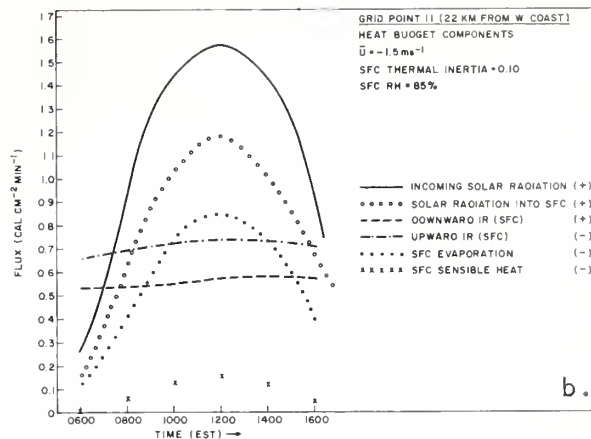
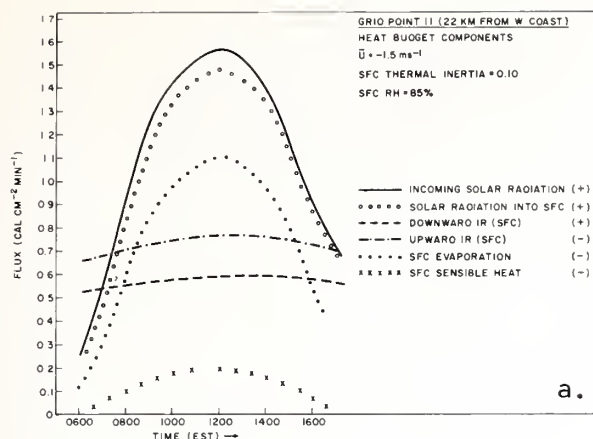


Figure 29. Diurnal components of the surface heat budget at grid point 11 (light wind case). (a) Albedo is 5% at all land grid points. (b) Albedo is 25% at all land grid points.

budget and sinusoidal temperature profiles are seen here.

The w profiles are similar to those for the low albedo (5%) case just discussed. In figure 27b, the figure in parentheses is the w value achieved below the x-axis for the appropriate grid point. Figure 28 shows the ΔT and w profiles for the medium wind speed case. The major feature on figure 28a is the large difference in ΔT between the low and high soil moisture case. The w profiles are similar to those shown in figure 26b. As in that case, the sinusoidal w amplitude is comparable with or exceeds the heat budget w profiles.

It is interesting to examine representative heat budget components that were calculated for two of the experiments discussed above. Figures 29a and 29b are plots at grid point 11 of the diurnal short- and long-wave radiation, evaporation, and sensible heat components for the 5% and 25% albedo cases. Grid point 11 was chosen because it is near the west coast sea breeze, which reaches maximum intensity and therefore is of special interest. The sensible heat input to the atmosphere is the primary contributor to sea breeze intensity. It can be seen that with an increase of surface albedo from 5% to 25%, sensible heat decreases. While not overly impressive on these diagrams, the effect is such that it is associated with a decrease in the 1600 EST value of 68,094 to 39,591 $\text{g cm}^{-1} \text{s}^{-1}$ on the west coast. This is a decrease in intensity of 42%. In terms of inadvertent or natural surface weather modification effects, this is not a trivial change. There is little change in the downward- or upward-directed IR fluxes.

Table 13 summarizes the experimental results where surface properties are uniformly and singly prescribed for all land grid points. The results are given in vertical mass flux (M) for both the west coast and east coast sea breeze. The conclusions of this series of experiments relate to the following:

- 1.) Differences between heat budget and sinusoidal versions.
 - (a) Air flow interacts with surface in heat budget version, but not with prescribed heating version. In heat budget version, the radiative, sensible, and latent heat fluxes act to change surface temperatures.
 - (b) Sea breeze intensities are greater for heat budget version as a result of higher temperature gradients.
 - (c) Sea breeze intensities decrease with increasing basic wind flow in heat budget version; opposite effect occurs in prescribed heating version.
- 2.) Importance of surface thermal properties.
 - (a) Soil moisture is the most important surface property. Albedo is next in importance.
 - (b) Variations in the thermal inertia exert minimal influence with high soil moisture values.
 - (c) The west coast sea breeze is more intense than the east coast sea breeze.
- 3.) Importance of heat budget components.
 - (a) Sensible heat is the important forcing component. The sum of sensible heat and

Table 13.

Summary of sensitivity experiments for systematic horizontal variations of surface properties uniformly and singly prescribed for all land grid points

Exp. No.	Experiment	Thermal Inertia	Albedo (%)	Soil Moisture (%)	Predicted Vertical Mass Flux (M)	
					West Coast	East Coast
EASTERLY WIND, 1.5 m s ⁻¹						
1	Low albedo	0.10	5.0	85.0	68094	37461
2	High albedo	0.10	25.0	85.0	39591	19387
3	Low TI	0.05	10.0	85.0	59700	32074
4	High TI	0.25	10.0	85.0	57108	31278
	Sinusoidal	—	—	—	31615	26945
EASTERLY WIND, 3.0 m s ⁻¹						
5	Low albedo	0.10	5.0	85.0	48612	30574
6	High albedo	0.10	25.0	85.0	28072	14175
7	Low TI	0.05	10.0	85.0	43163	28064
8	High TI	0.25	10.0	85.0	42829	25699
	Sinusoidal	—	—	—	40600	34828
EASTERLY WIND, 1.5 m s ⁻¹						
9	Low SM	0.15	15.0	75.0	74283	32837
10	High SM	0.15	15.0	95.0	42164	21429
EASTERLY WIND, 3.0 m s ⁻¹						
11	Low SM	0.15	15.0	75.0	47356	28604
12	High SM	0.15	15.0	95.0	29669	17406

NOTE: Sea surface temperature = 300.56 K. No clouds.

TI is thermal inertia in cal s^{-1/2} cm⁻² °C⁻¹.

Soil moisture is expressed as surface relative humidity (RH).

Vertical mass flux is in g cm⁻¹ s⁻¹.

evaporation components is almost constant. As evaporation is reduced, sensible heat increases. With reductions in albedo and soil moisture, sensible heat flux from the surface increases.

(b) The downward component of IR changes little from one experiment to another. It is almost constant during a diurnal cycle. The upward component also changes little.

6.3 Results: Systematic Variations of Surface Properties Uniformly and Singly Prescribed for Coastal Zones

Figures 30 and 31 provide the comparisons for coastal variations of surface properties. These should be compared as follows:

Light wind case:

Experiment 13 (Fig. 30) with Experiment 2 (Fig. 25).

Experiment 14 (Fig. 30) with Experiment 4 (Fig. 25).

Experiment 15 (Fig. 30) with Experiment 10 (Fig. 27).

Medium wind case:

Experiment 16 (Fig. 31) with Experiment 6 (Fig. 26).

Experiment 17 (Fig. 31) with Experiment 8 (Fig. 26).

Experiment 18 (Fig. 31) with Experiment 12 (Fig. 28).

These comparisons show that elevation of heating on both coasts above a reference level defined by uniform surface properties results in an increase in amplitude of east and west coast ΔT and w . There is also a retardation of the westward movement of the east coast sea breeze by 11 to 22 km.

Table 14 summarizes the experimental results where surface properties are uniformly and singly prescribed for coastal zones. Large increases in east and west coast values of M from the peninsula-wide uniformly prescribed case are seen here. In comparing these M values with those from table 13, large increases are seen for albedo and soil moisture while modest increases are seen for thermal inertia.

In summary, it is seen that changes in surface properties over short distances can result in large increases in sea breeze ΔT and w . Soil moisture is the most widely varying property and the one exerting the most influence.

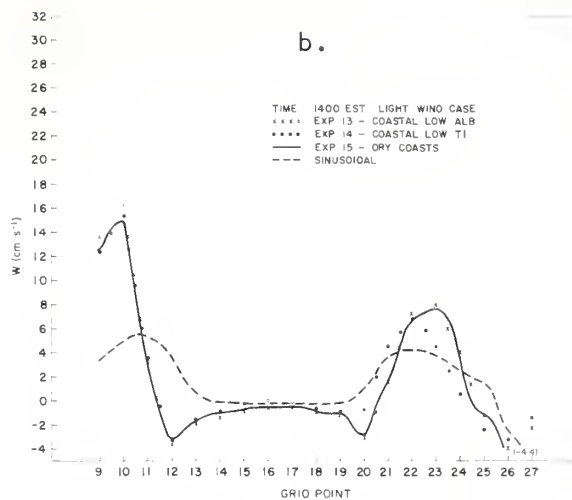
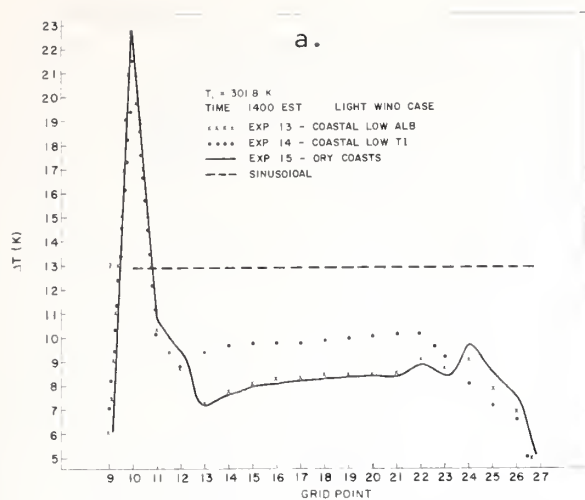


Figure 30. Comparison of coastal low albedo, thermal inertia, and soil moisture for light wind case (surface properties uniformly and singly prescribed for coastal zone). (a) Deviation (ΔT) at 1220 m. (b) Vertical motion (w) at 1220 m.

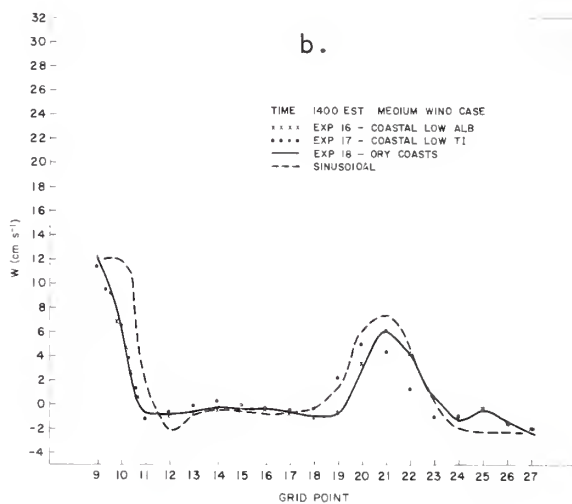
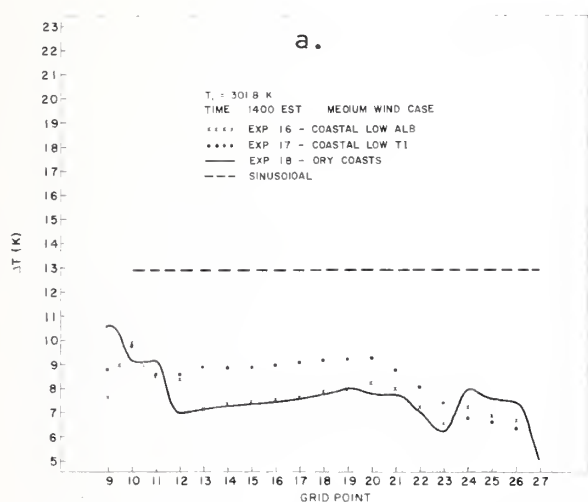


Figure 31. Comparison of coastal low albedo, thermal inertia, and soil moisture for medium wind case (surface properties uniformly and singly prescribed for coastal zones). (a) Deviation (ΔT) of land surface temperature from 0600 EST value. (b) Vertical motion (w) at 1220 m.

Table 14.

Summary of sensitivity experiments for systematic horizontal variations of surface properties, uniformly and singly prescribed for coastal zones

Exp. No.	Experiment										Predicted Vertical Mass Flux (M)	
		Soil Moisture			Surface Thermal Inertia			Surface Albedo			West Coast	East Coast
		Grid Points			Grid Points			Grid Points				
		10-12	13-23	24-26	10-12	13-23	24-26	10-12	13-23	24-26		
EASTERLY WIND, 1.5 m s ⁻¹												
13	Coastal low albedo	85.0	85.0	85.0	0.10	0.10	0.10	5.0	25.0	5.0	65408	35756
14	Coastal low TI	85.0	85.0	85.0	0.05	0.25	0.05	10.0	10.0	10.0	60472	33068
15	Dry coasts	75.0	95.0	75.0	0.15	0.15	0.15	15.0	15.0	15.0	62089	35839
	Sinusoidal	—	—	—	—	—	—	—	—	—	31615	26945
EASTERLY WIND, 3.0 m s ⁻¹												
16	Coastal low albedo	85.0	85.0	85.0	0.10	0.10	0.10	0.05	0.25	0.05	45555	26555
17	Coastal low TI	85.0	85.0	85.0	0.05	0.25	0.05	0.10	0.10	0.10	43307	28973
18	Dry coasts	75.0	95.0	75.0	0.15	0.15	0.15	0.15	0.15	0.15	46619	27563
	Sinusoidal	—	—	—	—	—	—	—	—	—	40600	34828

NOTE: Sea surface temperature = 300.56 K. No clouds.

Thermal inertia is in cal s^{-1/2} cm⁻² °C⁻¹.

Vertical mass flux is in g cm⁻¹ s⁻¹.

Soil moisture is expressed as surface relative humidity.

6.4 Results: Systematic Variations of Surface Properties Uniformly and Simultaneously Prescribed for Coastal Zones

Figure 32 shows the dramatic ΔT and w response to a simultaneous lowering of soil moisture to 25% and thermal inertia to 0.05 cal s^{-1/2} cm⁻² °C⁻¹. (The numbers in parentheses refer to ordinate values which are beyond the domain of the plot.) It is interesting to note that the east coast sea breeze lags by 44 to 55 km the 1400 EST positions shown in figures 26, 28, and 31, even though this is a medium wind experiment. These patterns probably represent extremes as clouds would normally form in response to such vigorous circulations induced by dry surfaces.

Results from Experiment 20 are not shown. The ΔT and w curves are almost coincident with those in figure 37. This indicates again that the dominant surface property is soil moisture, and thermal inertia variations will not dominate until soil moisture is vanishingly small. It should be noted, however, that the morning surface tem-

peratures were some 2° to 3°C higher for the prescribed thermal inertia of 0.05 than for the case where the value of 0.25 was prescribed. The additional heating effect was compensated for by increased afternoon evaporation which was associated with the higher surface temperatures that developed.

Figure 33 shows the diurnal profile of the heat budget components for Experiment 19. In this instance, the sensible heat input to the atmosphere exceeds the evaporation after 0900 EST. The upward IR flux from the surface is also high. It should be noted that evaporation remains at a high level after 1200 EST, unlike the patterns shown in figure 29. The downward IR component is similar to that shown in previous figures.

Table 15 summarizes the results for these experimental types. The vertical mass fluxes exceed by far those previously calculated.

In summary, it is seen that even for the medium wind case, a strong sea breeze response can result when soil moisture decreases to values most likely to be observed in highly drained and urbanized regions. Thermal inertia variations are relatively insignificant even when soil moisture is as low as 25%.

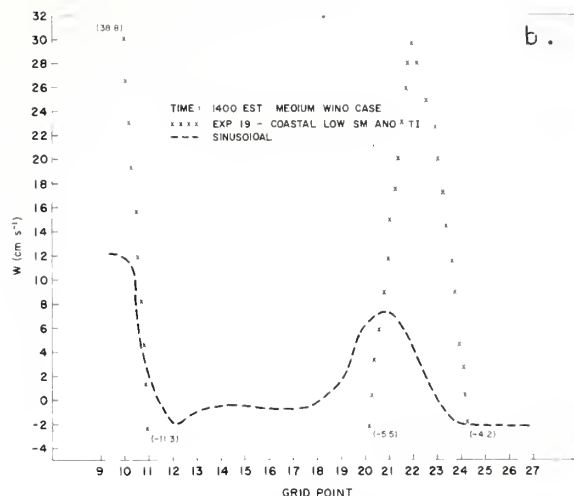
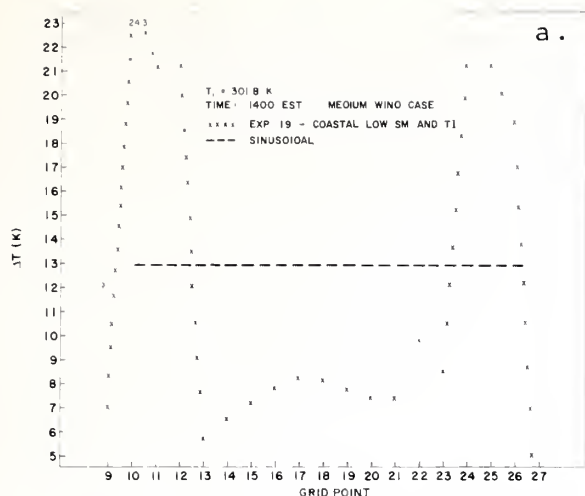


Figure 32. Comparison of soil moisture and thermal inertia for medium wind case (surface properties uniformly and simultaneously prescribed for coastal zones). (a) Deviation (ΔT) of land surface temperature from 0600 EST value. (b) Vertical motion (w) at 1220 m.

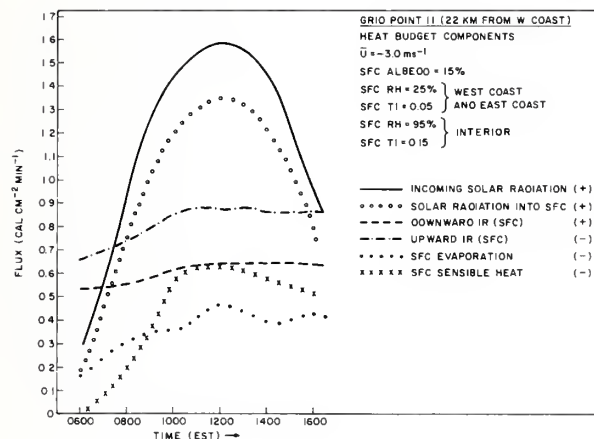


Figure 33. Diurnal components of the surface heat budget at grid point 11 (medium wind case).

Table 15.

Summary of sensitivity experiments for systematic horizontal variations in surface properties uniformly and simultaneously prescribed for coastal zones

Exp. No.	Experiment										Predicted Vertical Mass Flux (M)	
		Soil Moisture			Surface Thermal Inertia			Surface Albedo			West Coast	East Coast
		Grid Points			Grid Points			Grid Points				
		10-12	13-23	24-26	10-12	13-23	24-26	10-12	13-23	24-26		
EASTERLY WIND, 3.0 m s ⁻¹												
19	Coastal low SM and TI	25.0	95.0	25.0	0.05	0.15	0.05	15.0	15.0	15.0	118373	77216
20	Coastal low SM and TI	25.0	95.0	25.0	0.25	0.15	0.25	15.0	15.0	15.0	116114	79354
	Sinusoidal	—	—	—	—	—	—	—	—	—	40600	34828

NOTE: Sea surface temperature = 300.56 K. No clouds.

Thermal inertia is in $\text{cal s}^{-1/2} \text{cm}^{-2} \text{ } ^\circ\text{C}^{-1}$.

Vertical mass flux is in $\text{g cm}^{-1} \text{ s}^{-1}$.

Soil moisture is expressed as surface relative humidity.

Table 16.
Summary of sensitivity experiments for systematic horizontal variations in cirrus cloud optical properties uniformly prescribed for all land grid points

Exp. No.	Experiment	Geometric Thickness (km)	Emissivity	Predicted Vertical Mass Flux (M)	
				West Coast	East Coast
EASTERLY WIND 3.0 m s ⁻¹					
21	Thin cirrus	0.2	0.1	37977	22134
22	Medium cirrus	1.0	0.38	21232	9497
23	Thick cirrus	2.0	0.6	18148	0

NOTE: Sea surface temperature = 300.56 K.
Thermal inertia is $0.15 \text{ cal s}^{-1/2} \text{ cm}^{-2} \text{ }^{\circ}\text{C}^{-1}$.
Surface albedo = 15%.
Soil moisture (expressed as surface relative humidity) = 85%.
Vertical mass flux is in $\text{g cm}^{-1} \text{ s}^{-1}$.

6.5 Results: Systematic Variations of Cirrus Cloud Optical Properties Uniformly Prescribed for All Land Grid Points

The results of this series of experiments show the importance of cirrus cover. The cirrus effect can override the effects due to variable surface properties. The damping effect of cirrus shown here through modeling is compatible with the observations of solar radiation and soil surface damping discussed in Section 4. Figures 34 and 35 show the ΔT and w profiles for the thin, medium, and thick cirrus cases. The damping of the ΔT and w profiles is obvious. For the thick cirrus case, the sea breeze response is negligible.

Table 16 summarizes the results for these cirrus experiments. The decrease in M with increased cirrus thickness is very apparent.

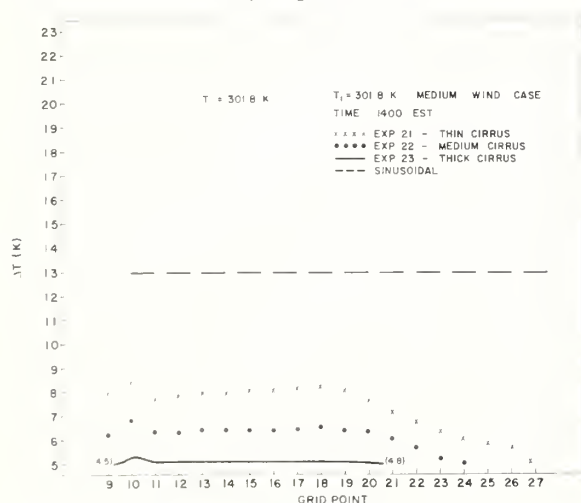


Figure 34. Land surface temperature deviations from 0600 EST value for thin, medium, and thick cirrus in medium wind case. Cirrus cloud optical properties are uniformly prescribed for all land grid points.

6.6 Results: Systematic Variation of Thick Cirrus Cloud Optical Properties Uniformly Prescribed for Interior and Coastal Zones

Figures 36 and 37 show the effect of selectively imposing thick cirrus cover in the case of light winds. Experiment 24 shows well-defined, but somewhat weak, ΔT and w patterns on both coasts as a result of prescribing thick cirrus in the interior. Experiment 25 shows well-defined ΔT maxima along the west coast and in the center of the study area when cirrus is imposed on coastal sections. The corresponding w pattern shows a higher maximum in the interior. For the medium wind case (not shown), results are similar, but weaker. A noticeable decrease in west coast ΔT occurs for the medium wind case.

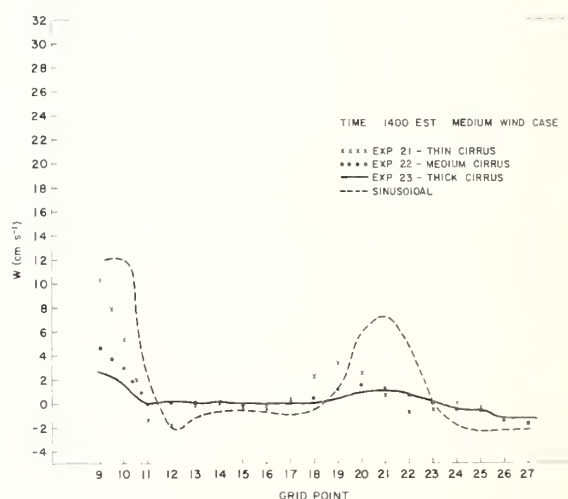


Figure 35. Vertical motion (w) at 1220 m for thin, medium, and thick cirrus in medium wind case. Cirrus cloud optical properties are uniformly prescribed for all land grid points.

Table 17.

Summary of sensitivity experiments for systematic horizontal variations in thick cirrus cloud optical properties uniformly prescribed for selected interior and coastal zones

Exp. No.	Experiment	Geometric Thickness			Emissivity			Predicted Vertical Mass Flux (M)	
		Grid Points			Grid Points			West Coast	East Coast
		9-15	16-21	22-27	9-15	16-21	22-27		
EASTERLY WIND, 1.5 m s ⁻¹									
24	Interior cirrus	—	2.0	—	—	0.6	—	38556	33919
25	Coastal cirrus	2.0	—	2.0	0.6	—	0.6	7823	38380*
	Sinusoidal	—	—	—	—	—	—	31615	26945
EASTERLY WIND, 3.0 m s ⁻¹									
26	Interior cirrus	—	2.0	—	—	0.6	—	32046	21216
27	Coastal cirrus	2.0	—	2.0	0.6	—	0.6	1645	30789*
	Sinusoidal	—	—	—	—	—	—	40600	34828

*Located in central portion of study area.

NOTE: Sea surface temperature = 300.56 K .

Thermal inertia = $0.15 \text{ cal s}^{-1/2} \text{ cm}^{-2} \text{ }^{\circ}\text{C}^{-1}$.

Albedo = 15%.

Soil moisture (expressed as surface relative humidity) = 85%.

Vertical mass flux is in $\text{g cm}^{-1} \text{ s}^{-1}$.

Table 17 summarizes the results for these cirrus experiments at selected segments of the study area. The most interesting aspect of these experiments is the shift in location of the sea breeze that can result from selective shielding of portions of the study area. Also, the greater magnitude of M in the interior than in the west coast (Experiments 25 and 27) is noteworthy.

In summary, it is seen that the maximum sea breeze response can be shifted in space and altered in intensity with partial cirrus shielding over the peninsula. If particles similar to cirrus particles could be distributed aloft in coherent patterns similar to those prescribed here, it appears likely that cumulus clouds could be generated (Gray et al., 1976) through mesoscale processes similar to those discussed here.

6.7 Importance of Evaporation Over South Florida

The potential for moist convection increases with increasing moist static energy in the lower layers of the atmosphere. This increase will normally occur through convergence of sensible heat and water vapor. In addition to that moisture advected inland from the Atlantic Ocean and Gulf of Mexico, the water vapor flux from the land and water surfaces of the peninsula is an important component of the water budget. It is shown that the total moisture supply is seriously underestimated if evapotranspiration from the surface is neglected.

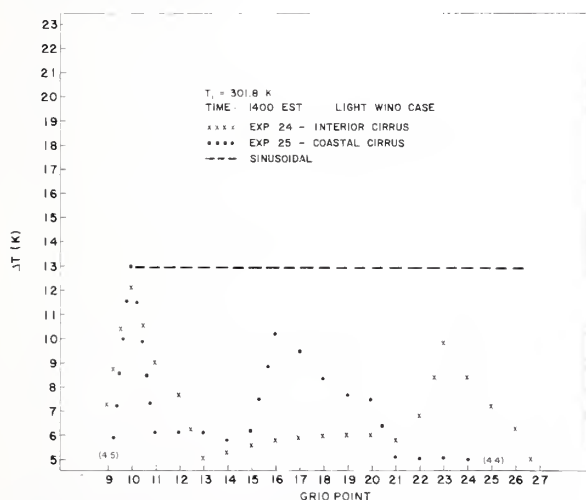


Figure 36. Land surface temperature deviations from 0600 EST value when distribution of thick cirrus is varied. Cirrus cloud optical properties are uniformly prescribed for interior and coastal zones (light wind case).

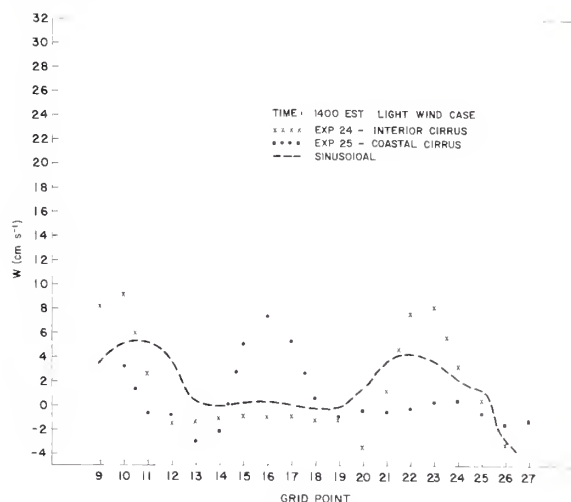


Figure 37. Vertical motion (w) at 1220 m for various distributions of thick cirrus. Cirrus cloud optical properties are prescribed for interior and coastal zones (light wind case).

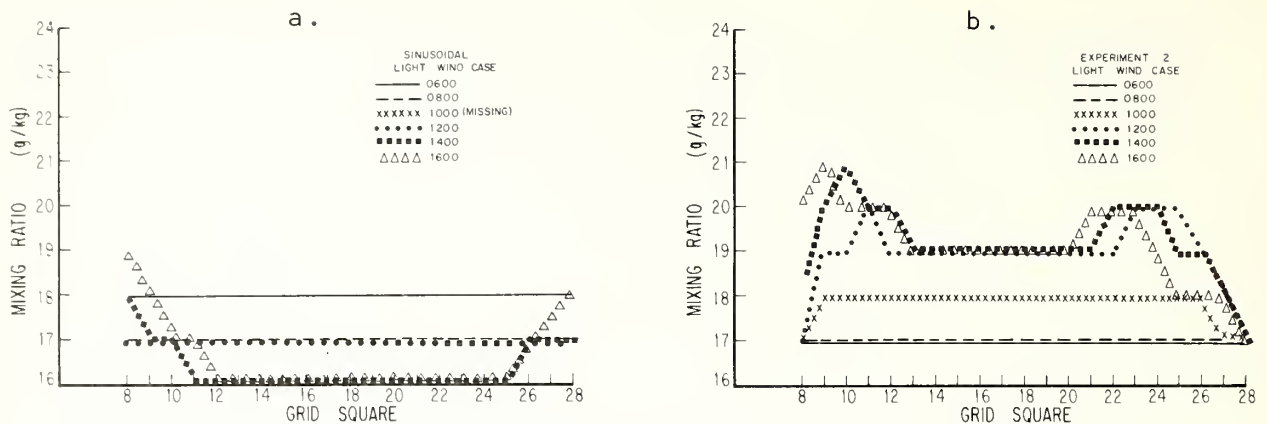


Figure 38. Time histories of mixing ratio at 75 m for each grid square across the study area. (a) Sinusoidal experiment (light wind case). (b) Experiment 2 (light wind case).

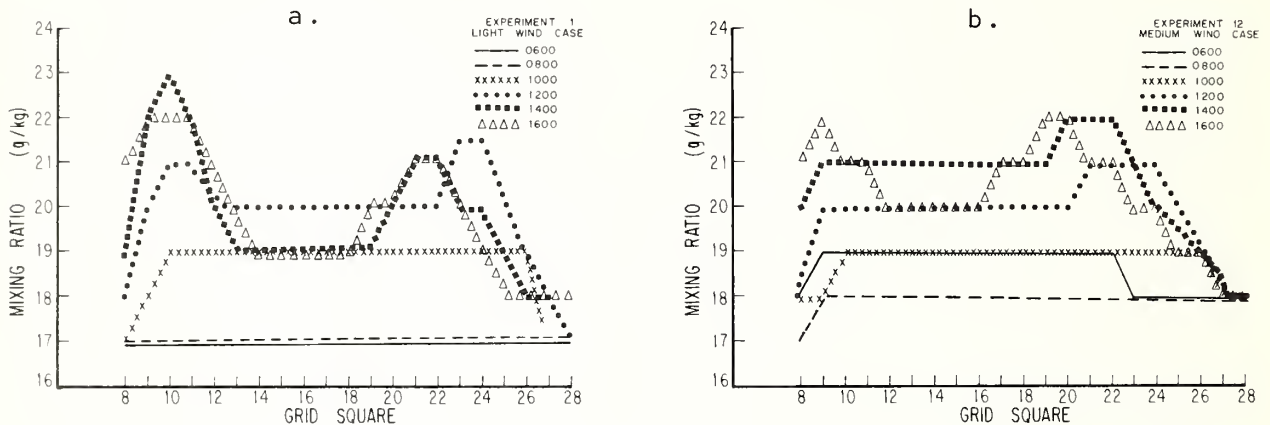


Figure 39. Time histories of mixing ratio at 75 m for each grid square across the study area. (a) Experiment 1 (light wind case). (b) Experiment 12 (medium wind case).

Figure 38a is a time history of mixing ratio (g/kg) at 75 m for each grid square across the study area. These profiles result from the sinusoidal experiment (initial wind speed is -1.5 m s^{-1}). Here the initial surface water vapor distribution over land has that value appropriate to the initial sounding value at 75 m, whereas over water it is defined by the saturation value for sea surface temperature. No additional moisture sources are prescribed during the diurnal cycle after initialization. The trend towards convergence (moistening) along the coasts and divergence (drying) in the interior is clearly shown.

By contrast, figure 38b shows the time history

of moisture for heat budget Experiment 2 with these conditions:

Initial wind:	-1.5 m s^{-1}
Surface albedo:	25%
Thermal inertia:	0.10
Surface RH	85%

The major contribution to the increased moisture at 75 m is the evaporation from the peninsula. Water vapor amounts are well in excess of those predicted when only advection of oceanic air is considered.

Figure 39a shows the moisture time history when surface albedo is lowered. This experiment

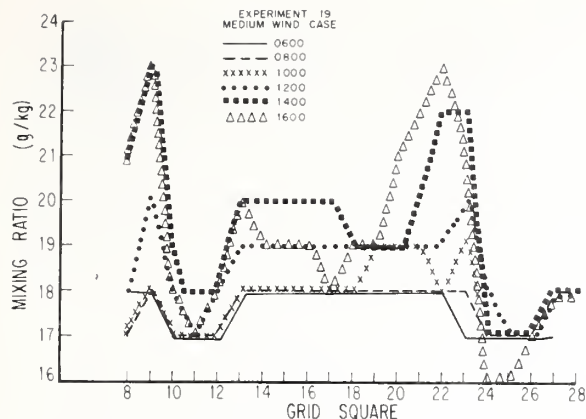


Figure 40. Time history of mixing ratio at 75 m for each grid square across the study area for Experiment 19 (medium wind case).

(#1) is identical to Experiment 2 (fig. 38b), except that albedo is specified as 5% instead of 25%. Note the enhanced moisture distributions along the coasts. These result from increased surface heating, which results in greater evaporation and a more intense sea breeze circulation.

When initial wind speeds increase to 3.0 m s^{-1} and soil moisture is specified as 95% RH, considerable moistening is seen across the peninsula. Figure 39b (Experiment 12) shows this clearly. The coastal organization seen in figure 39a is not evident here.

When soil moisture and thermal inertia are lowered along coastal strips and maintained at high levels inland, the moisture is highly concentrated on both coasts. Figure 40 (Experiment 19) shows the time history of moisture for the heat budget experiment having the following conditions:

Initial wind: -3.0 m s^{-1}
 Surface albedo: 15%
 Thermal inertia: 0.05 (grid points 10, 11, 12, and 24, 25, 26);
 0.15 (grid points 13–23)
 Surface RH: 25% (grid points 10, 11, 12, and 24, 25, 26);
 95% (grid points 13–23)

Note the well-organized and intense maxima on both coasts and the relative drying in the interior. These profiles demonstrate the effect of variable spatial distributions of surface properties,

particularly soil moisture. The ascending branches of the sea breeze circulation are concentrated along coastal regions. The potential for convection is enhanced by the moisture gained through evaporation in the interior which subsequently converges toward coastal regions in response to the evolving sea breeze circulation. These experiments demonstrate that latent heat flux into the atmosphere from heated land and water surfaces over Florida is a highly significant moisture source and should not be ignored in moisture budget studies for this region.

6.8 Summary of Sensitivity Studies

The sensitivity experiments show the following:

1) Realistic diurnal surface temperature profiles are obtained with heat budget experiments. One exception is the localized anomaly with light winds at one grid point on the west coast.

2) w from heat budget version generally decreases with increasing wind speed while w from sinusoidal version increases.

3) West coast sea breeze is stronger than east coast sea breeze for basic easterly flow.

4) Soil moisture is the most important surface property, followed by albedo and thermal inertia.

5) With values of soil moisture (surface relative humidity) $> 25\%$, differences in thermal inertia over the prescribed range result in little change in sea breeze response.

6) Changes in surface thermal properties over relatively small space scales yield large changes in sea breeze response. There is a large increase in w and significant retardation of east coast sea breeze with surface property changes on both coasts.

7) Variations in sensible heat flux from the surface are responsible for the variations in intensity. Soil moisture and albedo must be known for proper simulation of sea breeze behavior. Little variation is seen in downward IR.

8) Cirrus clouds can exercise a large and even dominant influence over surface heating and sea breeze response. Considerable variation in sea breeze behavior is possible depending on cirrus thickness and horizontal distribution.

9) Evaporation from the land and water surfaces of peninsular Florida constitutes an important source of water vapor to the lowest atmospheric layers.

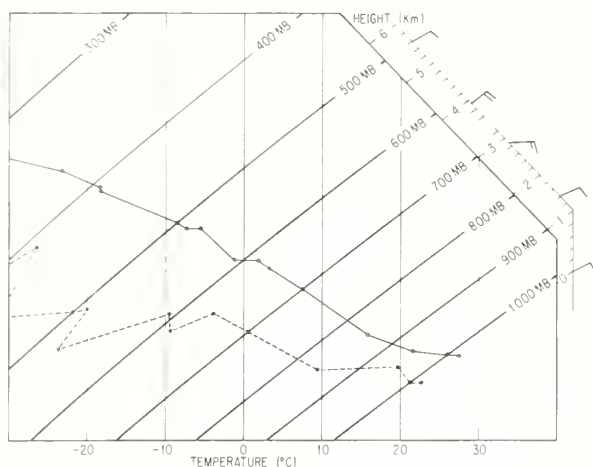
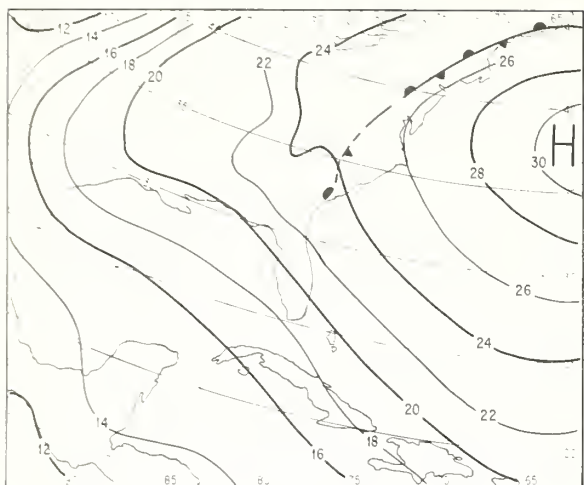


Figure 41. Prevailing meteorological conditions on July 16, 1975, in the vicinity of South Florida. Above: Surface weather map analysis of 1200 GMT. Below: Upper-air sounding for 1200 GMT, Miami, Florida.

6.9 Case Study of July 16, 1975

This day was chosen for a case study because it fits the criteria of a typical sea breeze day over South Florida. The day was synoptically undisturbed. Wind flow was generally east-southeast and therefore the flow was reasonably parallel to the two-dimensional x - z plane along $26^{\circ}30'N$. Thus, it is reasonable to expect surface layer air to be largely modified by the surface properties observed along this latitude strip.

Figure 41 shows the 1200 GMT surface map for that day and the 1200 GMT Miami sounding. During the preceding 48 hours, the Atlantic high had increased in central pressure and retrograded westward. A moderate gradient was established

which resulted in surface winds of 7 to 10 kt from the east-southeast. At 600 mb, wind speeds increased to 14 kt. The sounding was fairly moist up to 600 mb; above that level, drying was moderate.

The albedo profile shown in figure 5 was obtained from the NCAR Queen-Air pyranometers on that day. Surface infrared temperature signatures and airborne photography were obtained with the NOAA DC-6 and the Queen-Air. SMS-1 visual and infrared satellite coverage was excellent.

The grid square mean thermal inertia was obtained through use of figure 2. The day-versus-midnight temperature difference (ΔT) was obtained from the noon IR temperature profile from July 16, 1975, and the midnight IR temperature profile of August 20, 1975 (fig. 15). As albedo measurements are available for this day, soil moisture estimation was the remaining and formidable problem.

As cloud shielding can override the effects of surface properties, it was necessary to prescribe cloud cover, bases, and tops with care. For every half hour from 0530 EST through 1600 EST, the cloud cover in tenths was evaluated for each of the 19 grid squares constituting the cross section. Cirrus was not present until anvils were generated much later in the afternoon, so all clouds were treated as cumuliform. For each grid square, a square area equal to six grid squares was set up on the Bausch and Lomb (B & L) TV display console (Appendix B). This area was then centered on the grid square in question on the SMS-1 visible imagery while being displayed in color on the densitometer display TV monitor. All colors corresponding to clouds on the densitometer were identified, and the corresponding densities on the B & L TV were blacked out. The relative area of the clouds within the prescribed square was displayed with the throw of a switch, and the ratio of cloud area to total area was easily computed. This procedure was repeated for each grid square so that 437 separate cloud-cover calculations were performed. The cloud-cover calculations were based upon overlapping areas. Thus, clouds outside the confines of the grid square were included to account for cloud attenuation at high solar zenith angles. For four early morning periods, SMS-1 imagery was missing, so interpolation was necessary. Figure 42 shows the half-hourly cloud cover figures. Note the progression westward of cloud maxima after 1130 EST. The cloud bases were specified as being at 945 mb, which is equivalent to 2000 ft. Cloud tops were determined with the aid of a color densitometer display of SMS-1, 4-nmi-resolution, full-disk IR. This imagery, available at half-hourly intervals, provided color shadings that were compared with a precalibrated step wedge color/density and temperature relation.

GRID SQUARE TIME (EST)	10	11	12	13	14	15	16	17	18	19	20	21	22	23	24	25
0530	5	4	4	4	4	4	3	4	3	2	2	2	2	2	2	2
0600	5	4	4	4	4	4	3	4	3	2	2	2	2	2	2	2
0630	5	4	4	4	4	4	3	4	3	2	2	2	2	2	2	2
0700	4	4	4	4	4	4	2	3	2	2	2	2	2	2	2	2
0730	3	3	3	3	3	3	2	2	2	2	2	2	2	2	2	2
0800	2	2	2	2	2	2	2	2	2	2	2	2	2	2	2	2
0830	2	1	2	1	2	1	2	2	2	3	2	3	2	3	2	2
0900	0	0	0	0	0	0	0	1	1	2	3	4	3	3	2	1
0930	0	0	0	0	0	0	1	3	5	6	7	6	4	4	2	2
1000	0	0	0	0	0	0	1	3	4	5	5	3	2	3	3	3
1030	0	0	0	0	0	0	1	2	3	5	4	4	3	4	3	3
1100	0	0	0	0	0	1	2	3	4	4	4	4	2	3	2	1
1130	0	0	0	0	0	0	0	2	2	3	3	3	2	3	3	3
1200	0	0	0	0	0	1	2	3	2	4	5	5	4	3	1	0
1230	1	0	0	0	1	2	2	4	6	7	7	5	3	3	1	1
1300	1	0	0	1	0	0	1	3	4	4	2	1	1	0	0	0
1330	1	1	2	1	0	0	2	3	5	5	4	3	2	1	1	0
1400	0	1	2	1	1	2	2	2	4	4	2	2	1	1	0	0
1430	0	0	2	7	7	7	7	8	8	7	4	5	2	0	0	0
1500	1	3	5	7	7	7	5	4	3	4	3	1	0	0	0	0
1530	5	7	9	10	10	10	10	10	9	8	6	4	2	0	0	0
1600	10	10	10	10	10	10	10	10	10	8	5	4	5	3	0	0
1630	10	10	10	10	10	10	10	10	7	5	5	3	1	1	1	0

Figure 42. Time history of cumuliiform cloud cover in tenths at grid points 10 through 25.

From the temperature so determined, the appropriate pressure level corresponding to the cloud top was obtained from the 1200 GMT Miami sounding for July 16, 1975 (fig. 41).

The most difficult initialization task was the determination of grid square mean soil moisture. Every available relevant item of information bearing on this quantity was exploited. This was motivated by the recognition that the evapotranspirative component exerted the major control on the

differential heating. No daily water budgeting program for the area existed, and satellite microwave observations of soil moisture were not available. Therefore it was decided to make the best use of the limited resources on hand. Water-covered, vegetated and bare surfaces along the cross section were identified from the DC-6 nose camera color photographs for July 16, 1975. Special attention was given to the IR trace when the aircraft was over "hot spots" and the type of surface identified.

This information provided a reference frame for densitometer evaluation of combined (superimposed) LANDSAT (ERTS) II MSS-5 ($0.6\text{--}0.7\ \mu\text{m}$) visible and ($0.8\text{--}1.1\ \mu\text{m}$) near-IR data for July 7 and July 25, 1975. (LANDSAT data were not available for July 16, 1975.) The vegetation, water content, water, and soil moisture sensitivity of the four LANDSAT spectral intervals is adequately covered by NASA (1974) as well as by Coulson and Reynolds (1971). The capability of discriminating water from land and vegetation, particularly with the aid of the color densitometer, is very good. It was established that black organic peat muck, when saturated, has the same signature as water. Wet sand can be distinguished from dry sand; dry vegetation can be distinguished from wet vegetation. The general distribution of wet and dry areas for July 16 was thus established from aerial photos and interpolation between LANDSAT data.

The second and most tedious step was the calculation of daily mean rainfall, evaporation, and drainage for each grid square across the state. For each day from June 30 to July 16, 1975, mean evaporation from seven reporting stations in South Florida was obtained. The standard pan evaporation factor of 0.7 was applied as in the *Climatic Atlas of the United States* (Environmental Science Services Administration, 1968). Rainfall data were obtainable in the form of digitized WSR-57 radar rainfall (Woodley and Sax, 1976) for each grid square, the FACE 1975 rain gage network (fig. 8) and 11 South Florida National Weather Service reporting stations. The rainfall and evaporation data for NWS stations were obtained from NOAA/EDS climatological data (1975).

To calculate drainage, the predominant soil type and properties in each grid square were determined. From the Soil Survey for Okeechobee County, U.S. Dept. of Agriculture, 1971, the texture class, available water capacity, permeability, and drainage classification were obtained for soils along the cross section as listed on the General Soil Map (fig. 6). Drainage (hydraulic conductivity) curves for three texture classes of sand and organic peat soil were extrapolated from Elzef-tawy and Mansell (1975). Their curve relating the time rate of change of water content ($\text{cm}^3\ \text{cm}^{-3}\ \text{h}^{-1}$) to water content ($\text{cm}^3\ \text{cm}^{-3}$) applied to Lakeland fine sand, which is classified as a well-drained to moderately well-drained soil. The time rate of change of soil volumetric water content was assumed proportional to the available water capacity (AWC) so that, for example, if the AWC were twice the AWC for Lakeland fine sand, then its drainage time rate of change was assumed to be one-half that of the fine sand. Figure 43 shows the drainage curves for the four major soil types along the cross section. The curve for organic peat muck

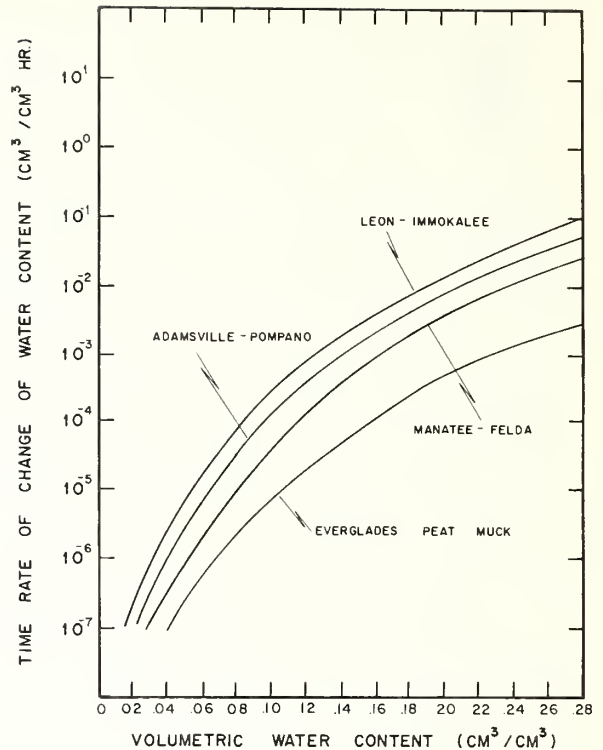


Figure 43. Drainage rate ($\text{cm}^3/\text{cm}^3/\text{h}$) as a function of volumetric water content (cm^3/cm^3) for the four major soil types along $26^\circ 30'\text{N}$.

was established in its location as the AWC is 40 times that of Lakeland fine sand. Note that for all curves there is a high rate of loss for high water contents and rapidly decreasing rates for low water contents.

The relation between the remaining (after drainage) volumetric water content ($\text{cm}^3\ \text{cm}^{-3}$) and relative humidity (RH) at the air-ground interface was determined in a similar manner. The surface relative humidity and water content relation of Nappo (1975) was modified. The curves were relabeled if they were in a position compatible with the AWC relation above. Otherwise, a new curve was established. Figure 44 shows this relation.

The following procedure was followed for each of the 15 days. For every one of the 19 grid squares, the area mean rainfall was determined. The drainage was calculated for each hour for 24 hours. The average evaporation figure for that day was then subtracted from the remaining soil moisture. This procedure provided the residual soil moisture for the next computation, and was followed until the initial grid square soil moisture values for July 16, 1975, were determined. From figure 44, surface relative humidity (RH) was then determined. Additional information concerning

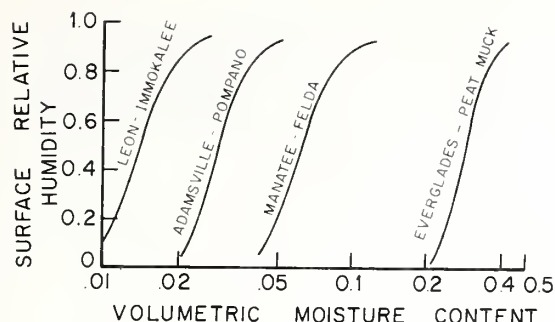


Figure 44. Near-surface relative humidity (%) as a function of volumetric water content (cm^3/cm^3) for the four major soil types along $26^\circ 30' \text{N}$.

soil moisture variations during the 15-day period is provided in Appendix C.

The thermal inertia and RH values were weighted according to the fraction of each grid square occupied by urban development or water. Swampy areas were given a thermal inertia of 0.05 and an RH of 25%. The thermal inertia, albedo, and surface relative humidity values are given in table 18.

Figure 45 compares model-predicted grid square average land surface temperatures at 1200 EST with the average surface temperatures obtained with the Barnes PRT-5 radiometer. This instrument was on the NOAA DC-6 aircraft which flew along $26^\circ 30' \text{N}$ from 1135 EST to 1210 EST on July 16, 1975. Grid points 9 and 27 are not included, as these are partially occupied by water. The following factors must be considered in comparing the two sets of data:

- 1) The model temperatures are to be considered averages for grid squares; IR-derived values are really 11-km averages for linear profiles.

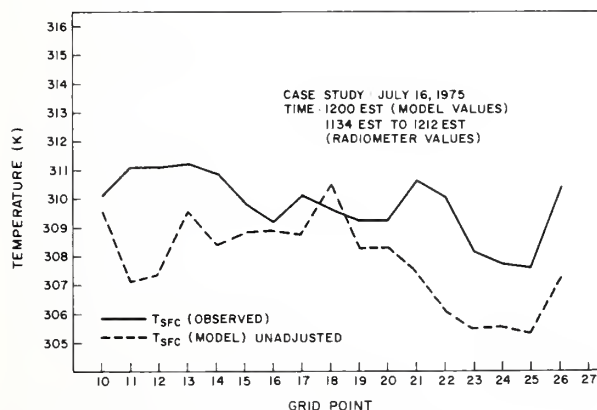


Figure 45. Land surface temperature predicted from model, and mean grid square surface temperature observed by radiometer.

- 2) Owing to the moisture distribution between 600 m (aircraft flight level) and the surface, the aircraft values should be increased 0.8°C . This latter figure is based on the attenuation curve used for the Hurricane Eloise research flight of September 17, 1975.

It is obvious that predicted temperatures are underestimates of the observed, except in the interior. As the sensitivity tests show, errors in surface temperature prediction will result primarily from errors in estimation of albedo or soil moisture. Thermal inertia is unlikely to exert a significant influence. The albedo values for this day are observed values. Therefore, the error lies in the data and/or the techniques used in the water-budgeting calculations used to determine soil moisture. The expected sources of error are listed below in decreasing order of importance.

- 1) None of the stations making pan evaporation measurements was located along the study area. Six of the seven stations were along the coast or on the shores of Lake Okeechobee. Use of a daily peninsular average value of evaporation is not realistic.

- 2) Radar rainfall estimates for July 15, the day preceding test day, had to be derived from the microfilm record because the digitized product was not available. This led to serious errors in averaging over grid squares.

- 3) Controlled drainage and irrigation in the mesonet black muck area produced variations in heating that could not be accounted for. Drainage is largely controlled by the water table resting upon relatively impervious limestone and marl layers (USDA, 1960). The transpiration effect of sugar cane during this period is unknown.

Because this case study is a special sensitivity experiment, the results using the surface relative humidity values from table 18 are presented and then compared with results obtained from adjusted values of surface relative humidity.

Unadjusted Experiment

Figures 46 and 47 are ΔT and w profiles plotted as a function of time and distance. Note, in figure 46, the heated strip along the east coast (grid point 26) and the weak ΔT minimum in the vicinity of the reservoir (grid points 24 and 25). The cloud field is responsible for much of the diurnal ΔT variation west of grid point 24. The maximum ΔT is 15.1°C . The w profile (fig. 47) shows a steady increase in intensity and westward progression of the east and west coast w maxima. The 1600 EST values of M are also plotted in figure 47. The east coast sea breeze intensity is quite large ($77,946 \text{ g cm}^{-1} \text{ s}^{-1}$).

Table 18.
Thermal inertia, albedo, and surface relative humidity for
July 16, 1975

Grid Square	Thermal Inertia ($\text{cal s}^{-1/2}\text{cm}^{-2}\text{C}^{-1}$)	Albedo (%)	RH (%)
9 (west coast)	0.14	12	95
10	0.115	12	96
11	0.105	13	100
12	0.098	12	100
13	0.099	14	83
14	0.102	13	100
15	0.105	12	100
16	0.135	12	100
17	0.101	14	98
18	0.093	13	81
19	0.089	15	100
20	0.092	12	100
21	0.088	10	100
22	0.088	19	100
23	0.125	16	100
24	0.162	8	100
25	0.142	10	100
26	0.091	16	81
27 (east coast)	0.068	17	63

Adjusted Experiment

The surface relative humidity values were adjusted by trial and error until the 1200 EST model-predicted temperature field was almost comparable with the observed field (fig. 48). Figures 49 and 50 show the ΔT and w profiles as a function of time and distance for the adjusted experiment. This experiment is the one best simulating the sea breeze events of this day. The maximum ΔT is

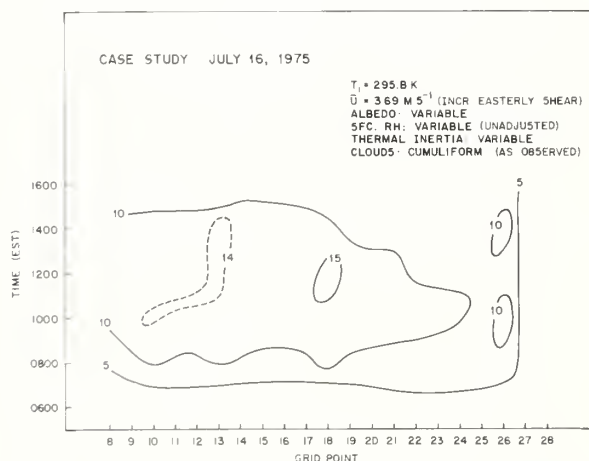


Figure 46. Land surface temperature deviation (unadjusted) from 0530 EST temperature (T_i) as a function of time and horizontal coordinate.

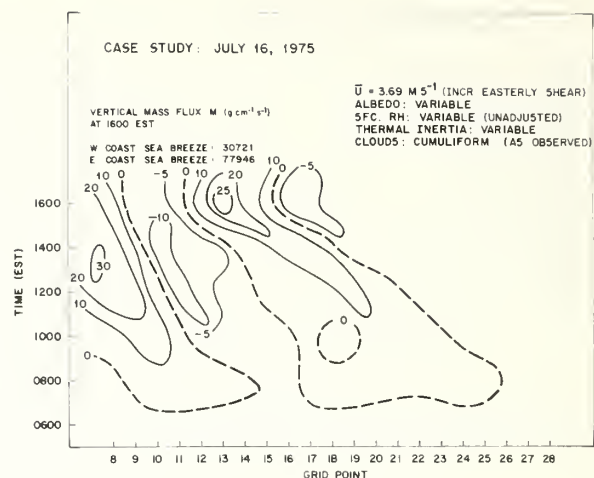


Figure 47. Vertical motion w (cm s^{-1}) at 1220 m (unadjusted) as a function of time and horizontal coordinate. Plot includes vertical mass flux M ($\text{g cm}^{-1} \text{s}^{-1}$) at 1600 EST.

15.6°C and the warmest temperatures appear 44 km farther to the east than on figure 46. The ΔT values along the east coast are higher by about 2°C . The value of M for the west coast sea breeze is stronger than the unadjusted case by 51%, while the east coast M value has decreased by 7%. Both the west and east coast sea breeze positions lag the unadjusted locations by 1600 EST. These differences in w result solely from the differences in surface temperature (2° – 3°C) made by altering surface soil moisture. Table 19 shows the difference between the unadjusted and adjusted values of surface relative humidity.

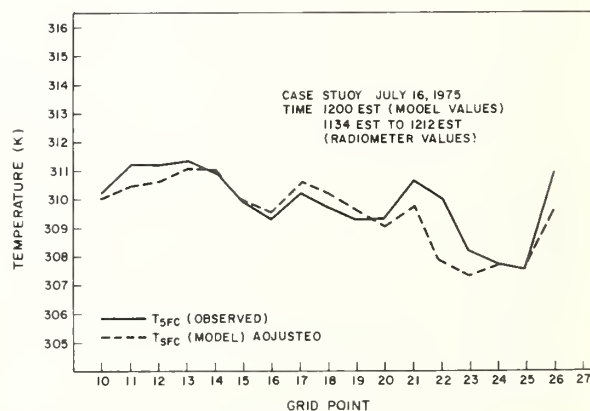


Figure 48. Predicted land surface temperature T , adjusted, and mean grid square surface temperature observed by radiometer.

Table 19.
Comparison of unadjusted and adjusted values of surface
relative humidity on July 16, 1975

Grid square	RH unadj (%)	RH adj (%)	RH adj- RH unadj
10	96	91	- 5
11	100	70	-30
12	100	70	-30
13	83	70	-13
14	100	75	-25
15	100	90	-10
16	100	97	- 3
17	98	89	- 9
18	81	95	+14
19	100	95	- 5
20	100	92	- 8
21	100	77	-23
22	100	80	-20
23	100	83	-17
24	100	83	-17
25	100	83	-17
26	81	65	-16

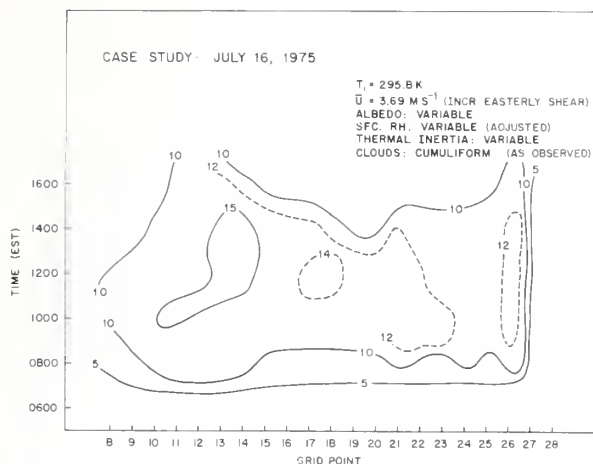


Figure 49. Land surface temperature deviation (adjusted) from
0530 EST temperature (T_i) as a function of time and hori-
zontal coordinate.

The rather marked westward progression of the east coast sea breeze and displacement of the west coast sea breeze over the Gulf are not caused solely by the prevailing basic wind field. Rather, they are partially caused by the cumulus cloud feedback effect where the surface is cooled owing to clouds shielding the surface from solar radiation. Sea breeze intensity is also affected. This is shown by figures 51 and 52. These results are from an experiment in which all variables are unchanged, except that cloud cover is completely removed. Figure 51 shows the maximum value of ΔT which is 15.8°C and two distinct maxima in excess of 15°C . Figure 52 shows that the east coast

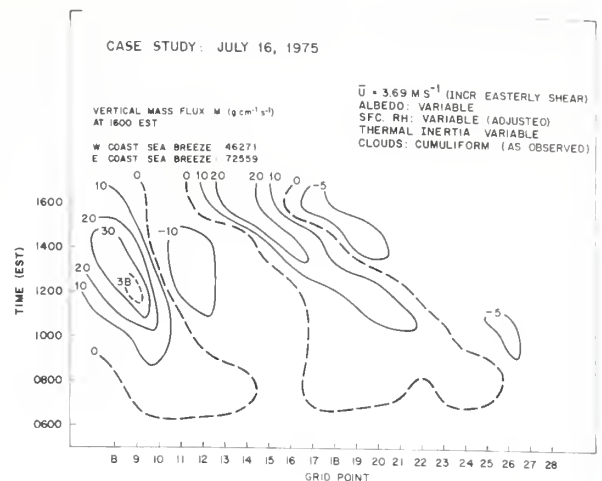


Figure 50. Vertical motion w (cm s^{-1}) at a height of 1220 m (ad-
justed) as a function of time and horizontal coordinate. Plot
includes vertical mass flux M ($\text{g cm}^{-1} \text{s}^{-1}$) at 1600 EST.

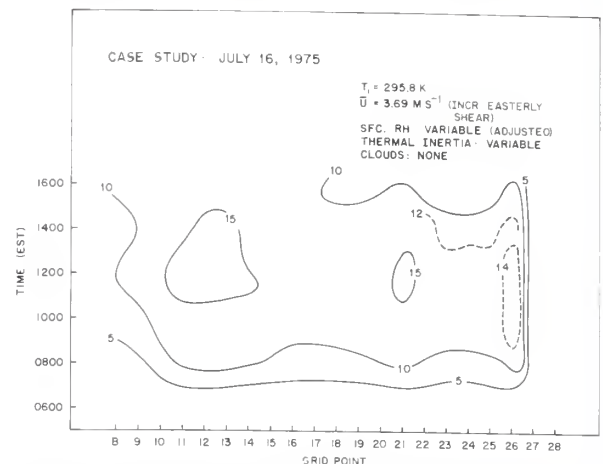


Figure 51. Land surface temperature (adjusted no-cloud) from
0530 EST temperature (T_i) as a function of time and hori-
zontal coordinate.

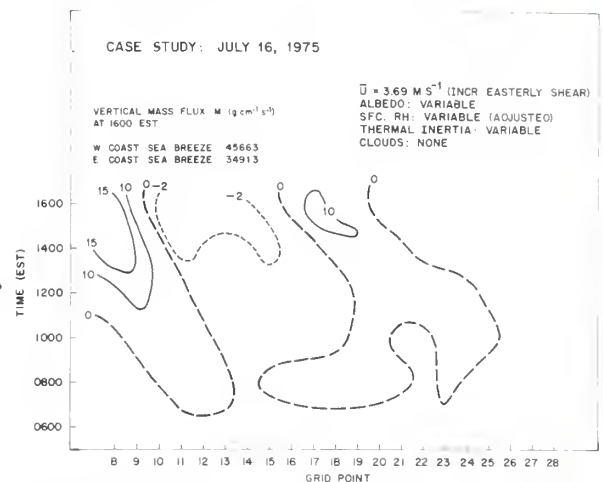


Figure 52. Vertical motion w (cm s^{-1}) at 1220 m (adjusted no-
cloud) as a function of time and horizontal coordinate. Plot
includes vertical mass flux M ($\text{g cm}^{-1} \text{s}^{-1}$) at 1600 EST.

sea breeze lags the cloud case by 33 km. Although the west coast sea breeze is about as intense as in the cloud case, the east coast sea breeze intensity is only 48% of the intensity of the cloud case.

Verification

Although this case study series is primarily a sensitivity experiment using observed or deduced data, it is of interest to examine the radar and surface wind and satellite cloud fields that existed on this day. The ability to verify the cloud (adjusted) simulation with actual data is limited. Therefore, model results must be viewed in the proper perspective. The following provisos are presented for this purpose:

- 1) The neglect of the third (north-south) dimension resulted in gradual deterioration of the prediction after 1400, particularly in the western third of the study.

- 2) Surface winds used for verification are sparse in all regions, except in the mesonet. Here, the wind field is reflecting both the cumulus scale perturbations superimposed on the mesoscale flow and the mesoscale flow itself. This makes precise identification of the sea breeze "front" or mesoscale convergence zone somewhat difficult.

- 3) One large cloud mass developed over the study area and could not be correlated with any of the predictive modes just discussed. In any situation, extreme care must be taken in depending upon satellite imagery or radar returns alone to mark the location of the center of the sea breeze convergence zone. Cumulus clouds that are formed in the maximum upward motion region of the sea breeze act to shield the surface from solar radiation and thereby cool it. The cloud shielding acts to enlarge the region covered by cool air and increase the temperature gradient. With the increased surface temperature gradient, the sea breeze convergence zone is intensified and accelerated. Figure 49 shows the increased temperature gradient on the surface in the adjusted (cloud) case. The intensification and acceleration of the east coast sea breeze from clouds is seen by comparing figure 50 of the adjusted (cloud) case with figure 52 of the adjusted (no-cloud) case. Also, note that M for the no-cloud is only 48% of the cloud case. The cloud-induced differential

motion appears as a propagation mechanism that continually permits new cloud growth. Growth should occur within the sea breeze convergence zone, which will then be forced once more to precede the cloud field. This process is suggested as a possible mechanism for the "pulsing" behavior of lake breezes observed by Moroz (1967) and Tingle (1971).

- 4) The influence of Lake Okeechobee was probably felt later in the period; however, on this day its influence is considered marginal. This conclusion is based on the apparent lack of significant outflow of air over the lake towards the south.

Figures 53 through 57 show the radar echo history with superimposed w profiles (from fig. 50) from 1000 EST to 1630 EST. It should be recognized that thermal forcing was also altered by nonprecipitating cloud matter undetected by radar. The east coast sea breeze precipitation line appears to be in the vicinity of grid point 21 at 1200 EST while the w maximum is 22 km farther west. The line is seen to move west and accelerate between 1300 EST and 1402 EST. The w maximum precedes throughout. The echoes are organized in a north-south line which passes through grid point 17 at 1402 EST. (The cloud mass that appears at grid point 20 at 1402 EST and links up to a cloud mass south-southeast of this point at 1500 EST cannot be identified with the east coast sea breeze positions predicted by any of the model simulations.)

By 1500 EST, the cloud line passing through grid point 17 at 1402 EST was located north of grid point 15 after decelerating. The deceleration shows in figure 50 as well as in the cloud field. The w maximum was just ahead of the cloud line at this time. From this point on, the pattern becomes distorted by three-dimensional wind flows in the western half of the study area. (These flows will be shown momentarily.) These contribute to the cloud mass generated south of Immokalee, which moves across the study area by 1536 EST. The slow-moving west coast sea breeze is shown to move into the Gulf by 1400 EST. There is a tendency for cloud development immediately to its east from 1430 EST on. The bulk of the offshore convection appears to lie to the south of the study area.

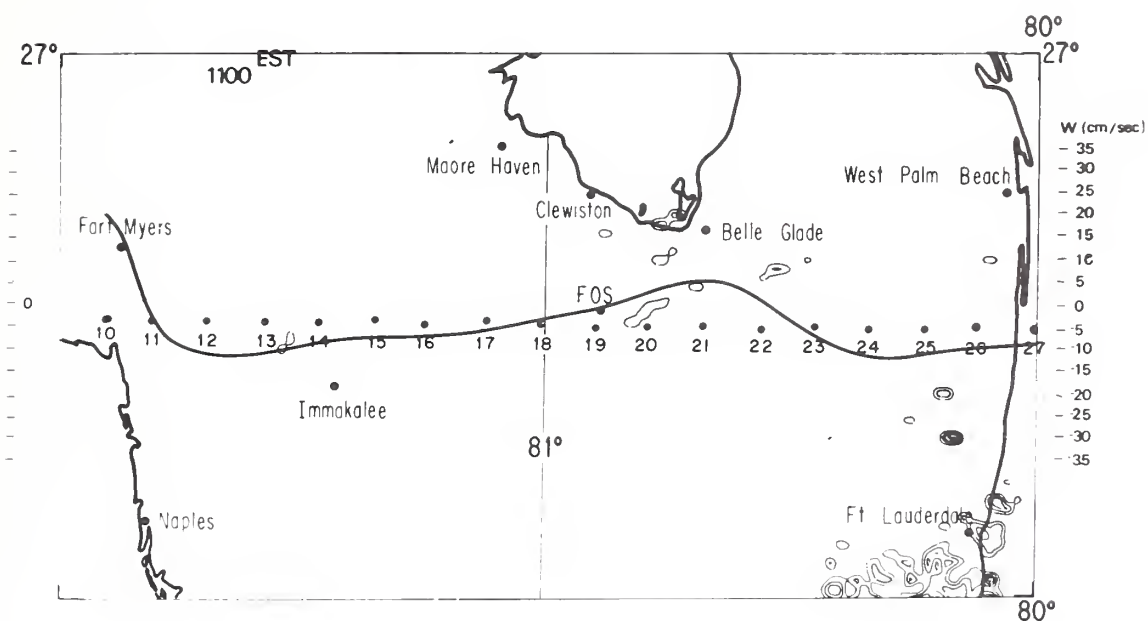
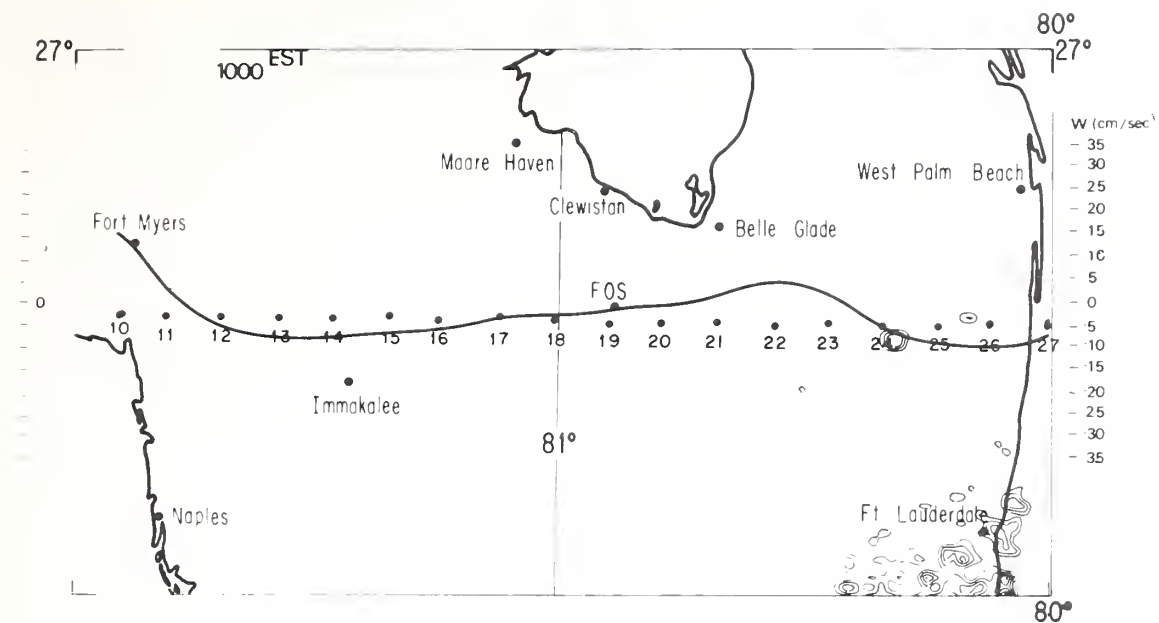


Figure 53. Radar echo contours (every 5 dBZ) and w profiles on July 16, 1975, at 1000 EST and 1100 EST.

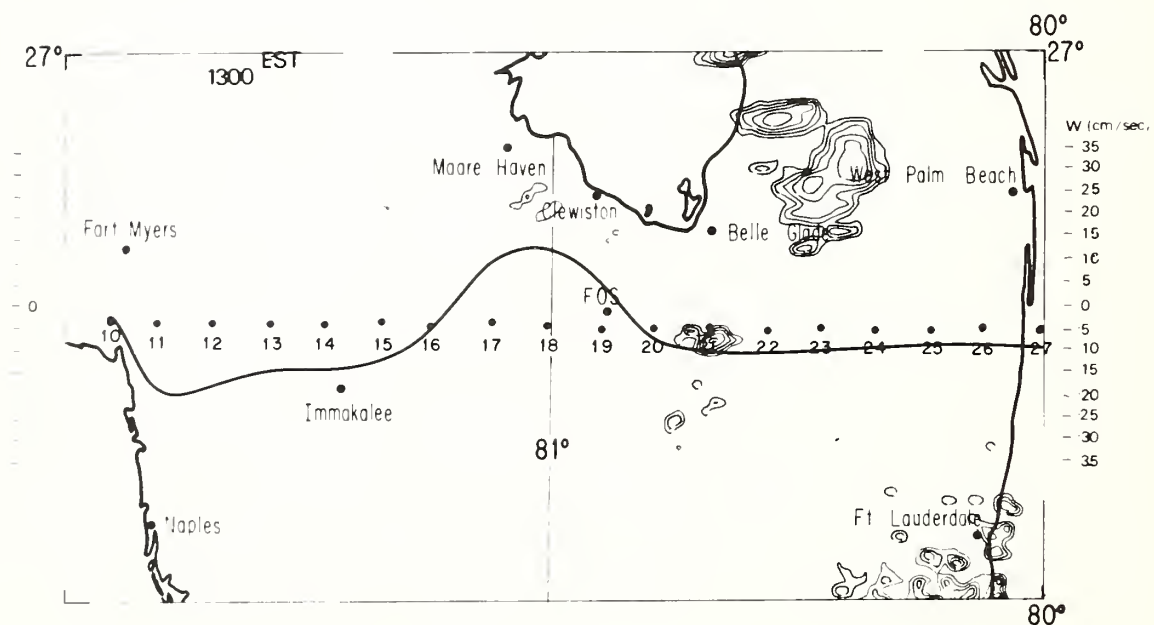
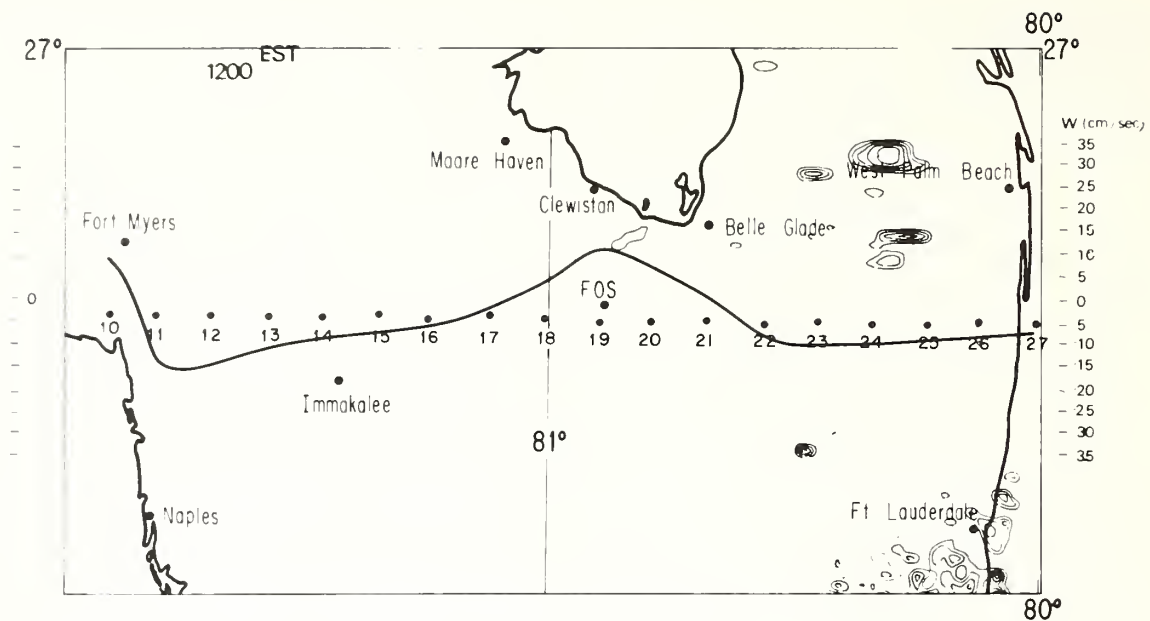


Figure 54. Radar echo contours (every 5 dBZ) and w profiles on July 16, 1975, at 1200 EST and 1300 EST.

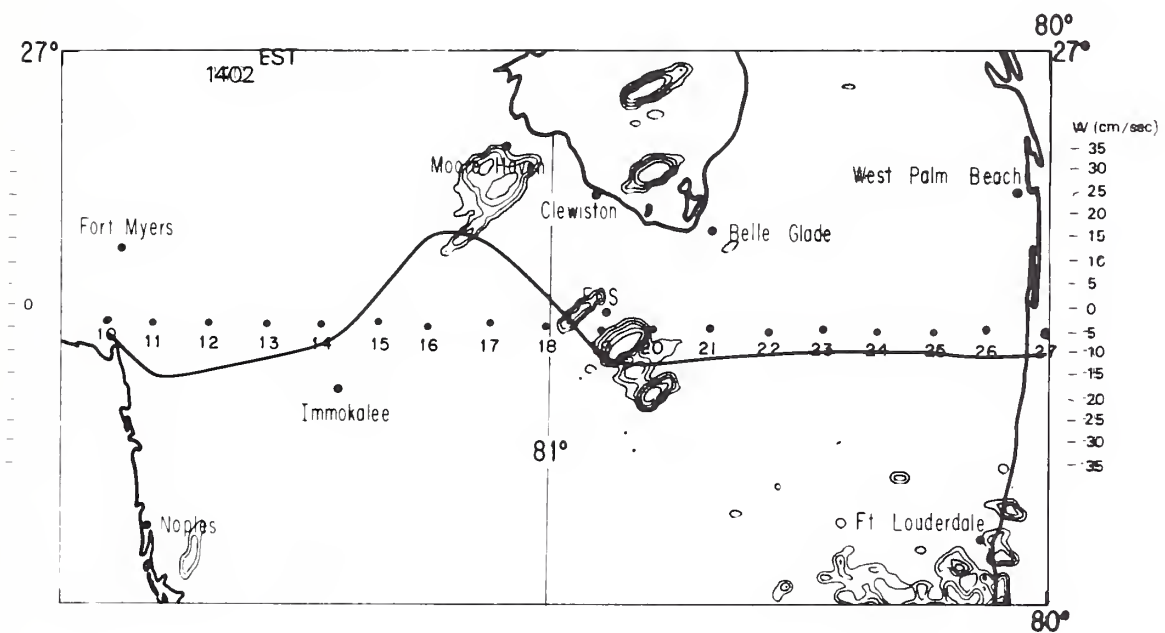
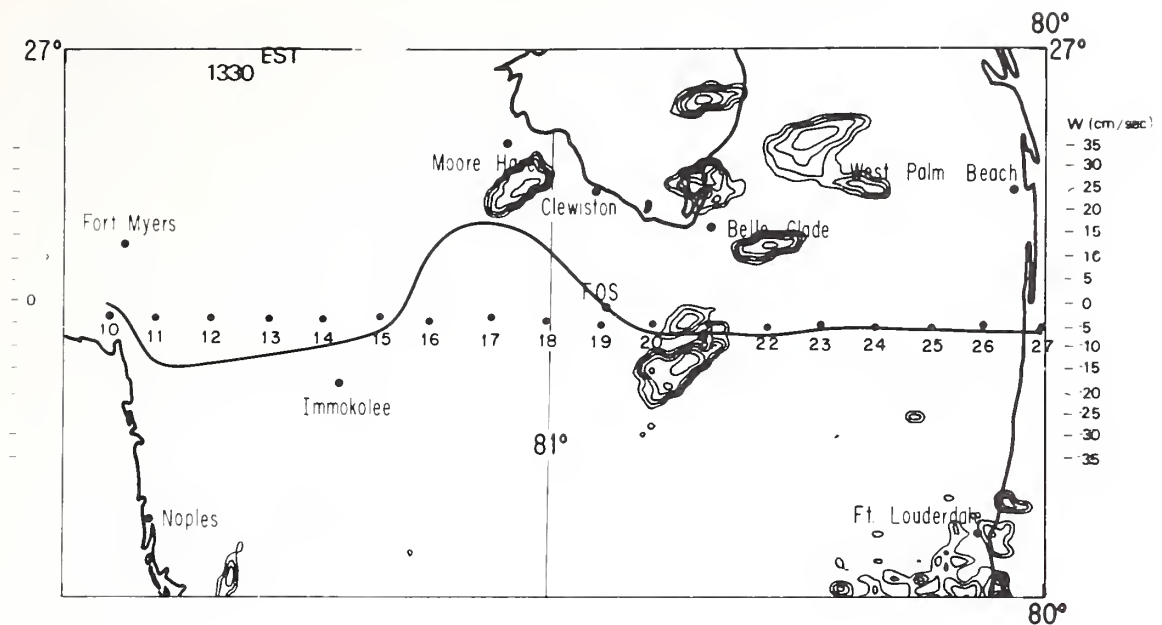


Figure 55. Radar echo contours (every 5 dBZ) and w profiles on July 16, 1975, at 1330 EST and 1402 EST.

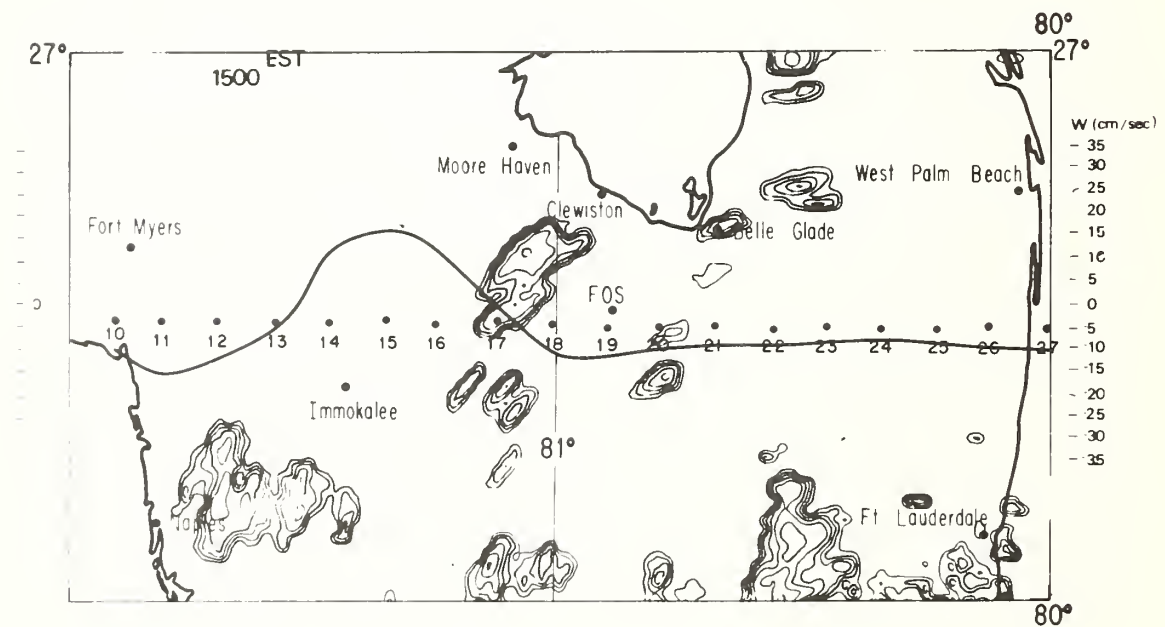
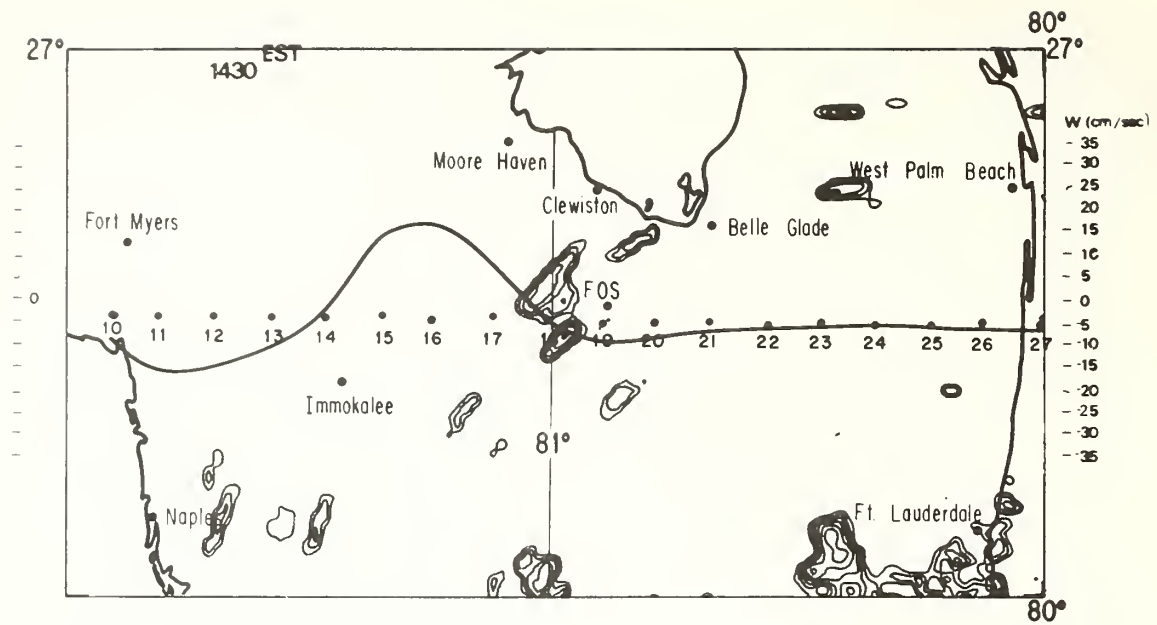


Figure 56. Radar echo contours (every 5 dBZ) and w profiles on July 16, 1975, at 1430 EST and 1500 EST.

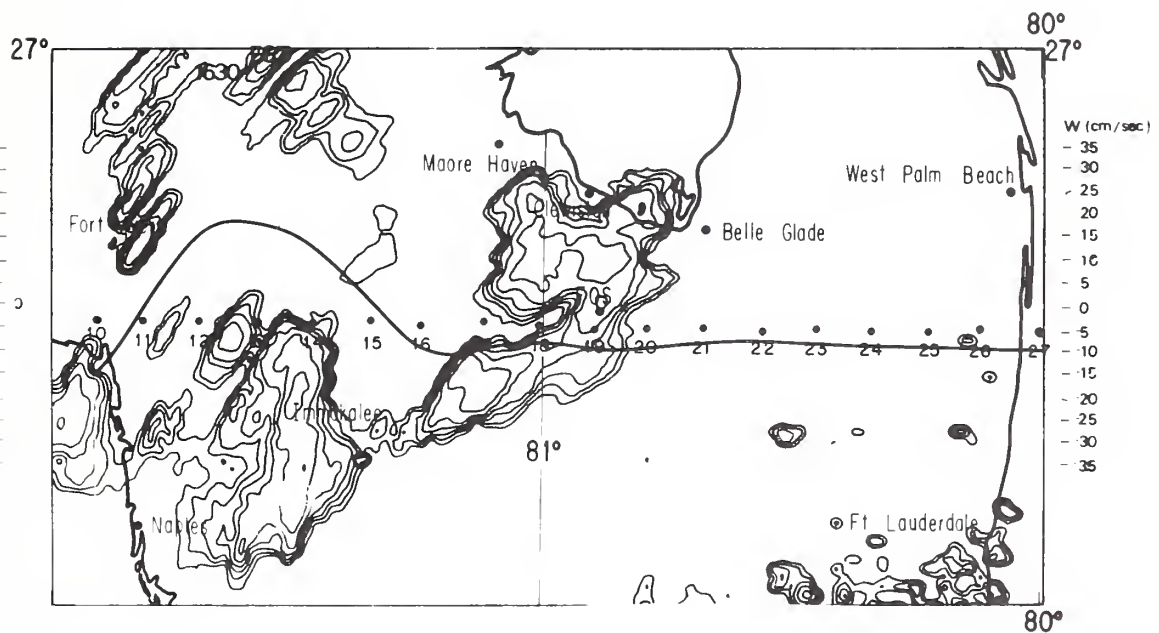
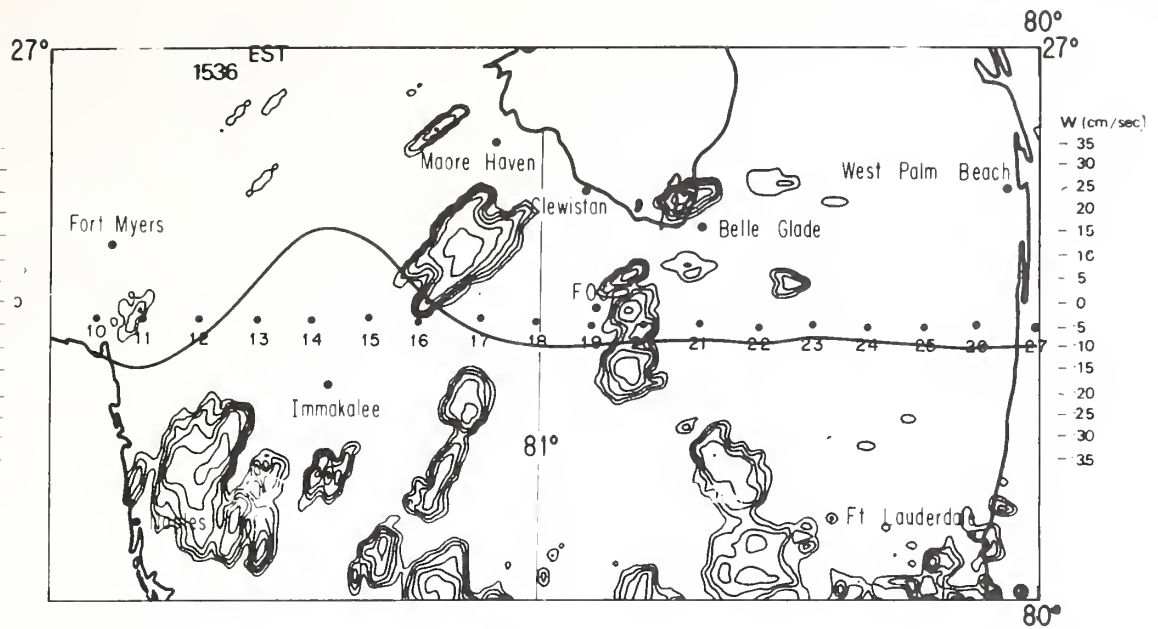


Figure 57. Radar echo contours (every 5 dBZ) and w profiles on July 16, 1975, at 1536 EST and 1630 EST.

Figures 58 and 59 show characteristics of the surface wind field at 1200 EST, 1300 EST, 1400 EST, and 1500 EST. The streamlines are drawn to fit the synoptic surface winds at coastal stations and mesonet winds south of the lake. Perturbations in the wind field due to cloud scale circulations are evident. The model-predicted convergence zones are given by the jagged vertical lines oriented in a north-south direction. The model-predicted winds at 50 m are given at each grid point.

The streamlines were drawn for the observed surface winds before superimposition of the model winds. Note the change of wind flow in the western half of the area with the inclusion of the first observed wind from Naples (1300 EST). The western half of the study area is considered basically unverifiable because wind observations are lacking. Streamlines for the eastern half can be compared fairly well with the observed flow.

At 1200 EST, there is evidence of a broad troughing in the wind field which corresponds to the model-predicted convergence zone. At 1300 EST, this has propagated westward and becomes unverifiable after this time. A new mesoscale perturbation is seen to have extended northward from south of the study area to lie between grid points 20 and 21 by 1300 EST. From this time on, this system moves westward.

The slow-moving west coast cloud mass and more rapidly moving east coast cloud mass are explained by the model very well. It is suggested that the cloud mass that grows to the north from south of the study area into the network resulted from different surface and initial cloud conditions which prevailed south of the study area.

In summary, the following important conclusions from the case study are drawn:

1) Accurate observations of soil moisture and albedo are required for realistic model simulations of surface temperature. Sea breeze behavior is quite sensitive to changes in surface thermal properties and the resultant surface temperature profile.

2) The cloud field is a major influence in establishing the motion and intensity of the sea breeze. The major west and east coast cloud fields were observed to have good continuity. The w maxima, particularly the east coast core, were predicted by the model to move at speeds nearly equal to those attained by the observed clouds. This fact, considered in conjunction with the no-cloud (adjusted) results, shows that cloud radiation shielding does exert an influence and must be considered. The no-cloud experiment does not predict w patterns bearing a clear relationship to any of the observed cloud fields except for the quasi-stationary west coast field.

3) The differences in intensity among the cloud (unadjusted), cloud (adjusted), and no-cloud (adjusted) experiments provide compelling evidence of the importance of surface and cloud properties and the necessity of using a heat budget formulation in sea breeze models. Differences in sea breeze location of 33 to 44 km, seen between the cloud (adjusted) and no-cloud (adjusted) cases are by no means insignificant. Further observational and numerical studies are necessary to establish the degree of difference that exists for other wind regimes and atmospheric stratifications.

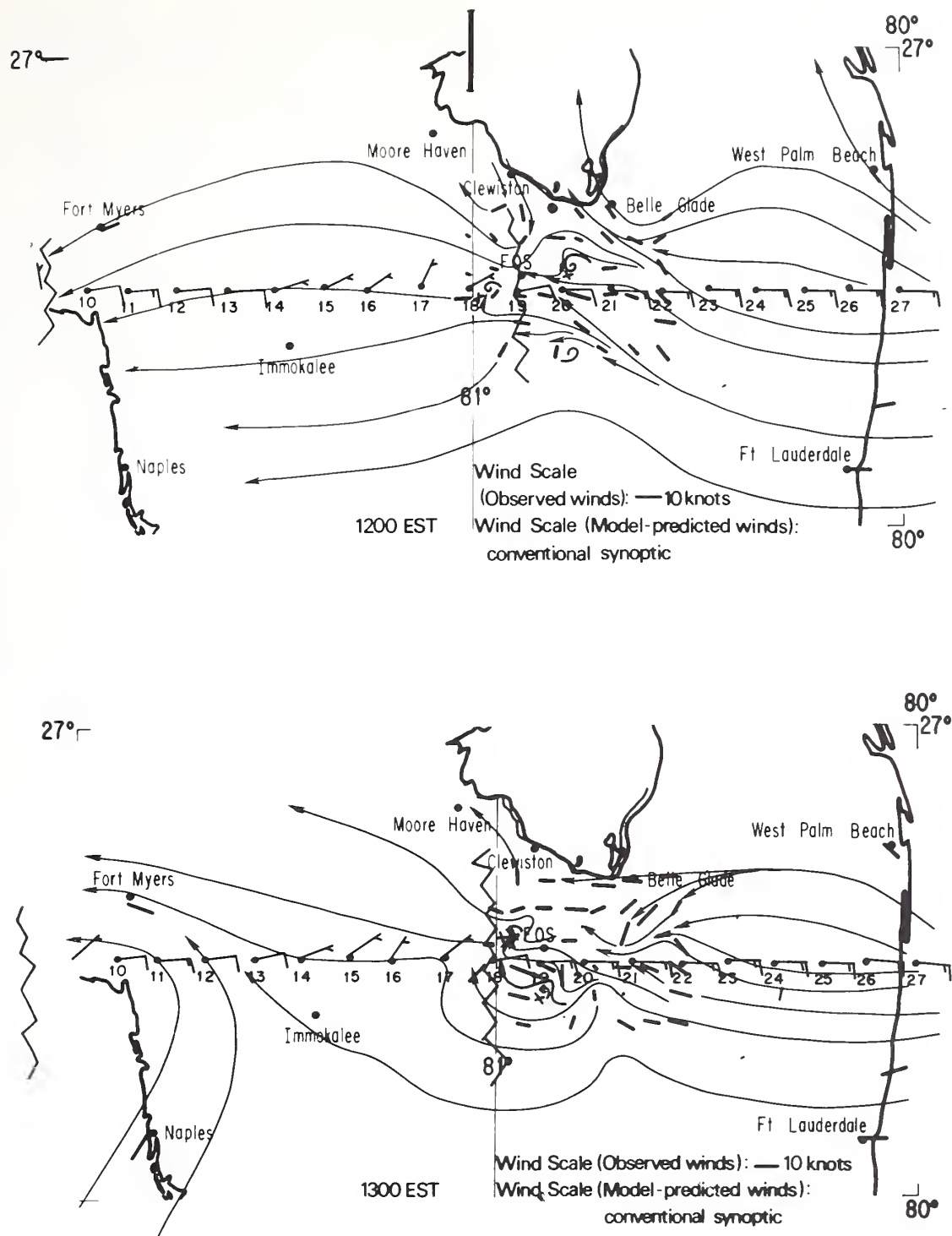


Figure 58. Surface streamlines for observed wind field and predicted 50-m winds, 1200 EST and 1300 EST, July 16, 1975.

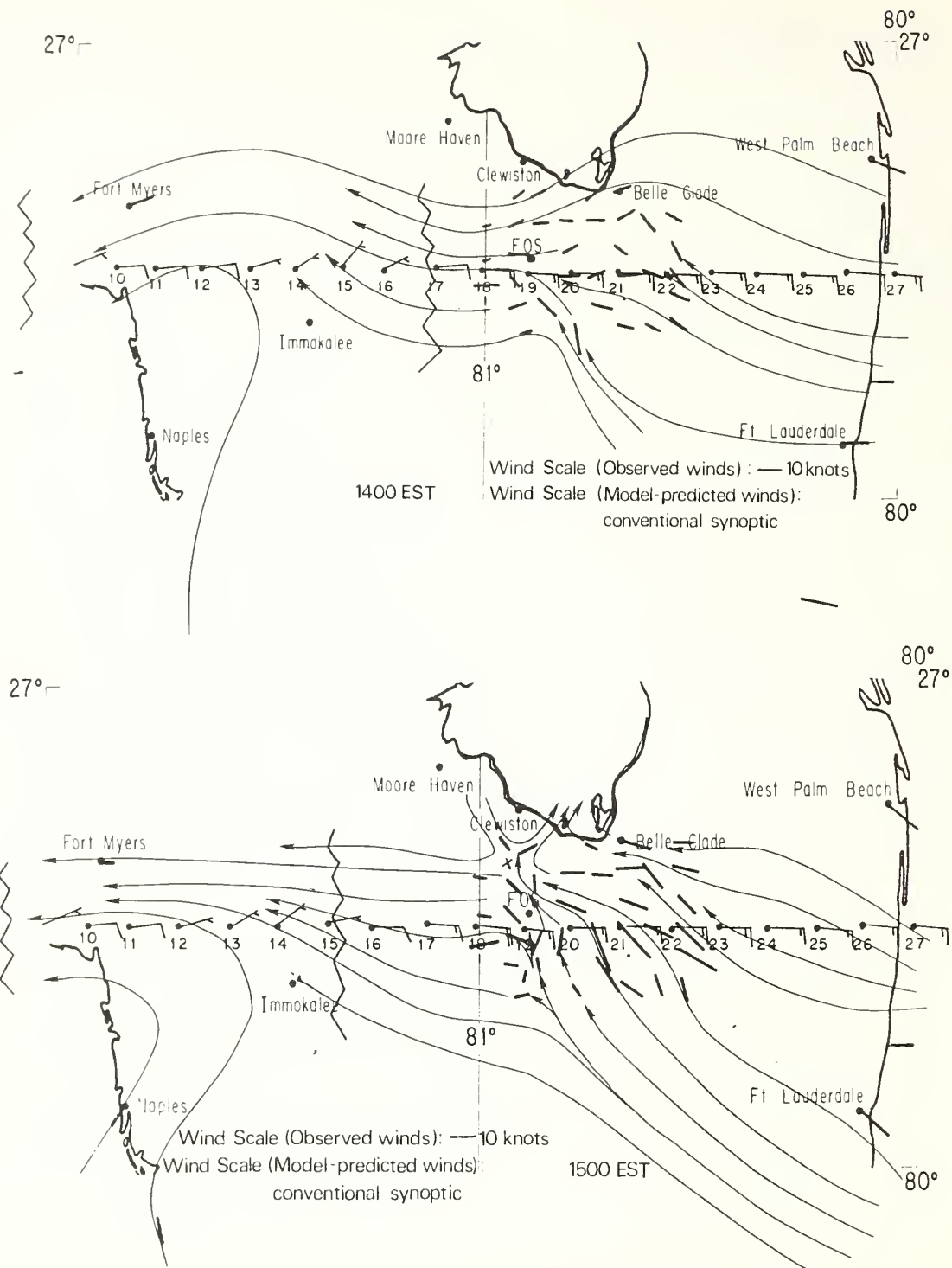


Figure 59. Surface streamlines for observed wind field and predicted 50-m winds, 1400 EST and 1500 EST, July 16, 1975.

7. SUMMARY AND CONCLUSIONS

7.1 Summary of the Problem

The principal objective has been the study of the effects of horizontal and time variations of land surface heating on the sea breeze. This objective is attained through analysis of observations, and through numerical modeling based on the analysis. Observations of surface properties were studied, yielding a knowledge of the numerical ranges of these properties and their temporal and spatial variations across South Florida. The principal objective is then attained by conducting numerical model sensitivity experiments and a numerical case study experiment. The sensitivity experiments enable comparisons to be made between sea breeze model results from a surface heat budget formulation and a prescribed sinusoidal thermal forcing formulation. These experiments also show the relative importance of the surface properties and cirrus cloud cover. The case study is conducted to demonstrate the necessity of considering both surface and cumulus cloud properties in model simulations of the sea breeze.

7.2 Summary of Observational Study

An analysis of observations yielded the following information:

1) Cross-peninsula observations

(a) Albedo. High-surface albedos (20%–25%) characterize developed strips on both coasts of Florida and pasture, sugar cane, and sandy areas inland. Low-surface albedos (7%–14%) are seen for the Atlantic, Gulf, swamp, and muck soil regions.

(b) Thermal inertia. Thermal inertia is deduced from the day-midnight temperature observations and surface albedo, or calculated with the aid of the heat budget equation. The minimum value over land is about $0.05 \text{ cal s}^{-1/2} \text{ cm}^{-2} \text{ }^{\circ}\text{C}^{-1}$ (cities, dry uncultivated areas, etc.) and the maximum is on the order of $0.30 \text{ cal s}^{-1/2} \text{ cm}^{-2} \text{ }^{\circ}\text{C}^{-1}$ (swamps, wet vegetated areas, etc.).

(c) Soil moisture. Soil moisture calculations based on water-budgeting procedures show a range from 0% to 100% in surface relative humidity. The greatest fluctuations are found in sandy soils near coastal regions.

(d) Surface temperature. The surface temperatures were obtained from radiometers mounted on aircraft. Coastal and black muck regions are characterized by high noon surface temperatures (40° – 46°C) under minimum cloud conditions. Swamps and reservoirs exhibit temperatures around 33°C . Some isolated areas were seen to have temperatures of 50°C . Considerable variation in cross-peninsula surface profiles resulted from soil moisture and cloud distributions.

2) Individual station observations

(a) Solar radiation. During typical periods with scattered to broken cloud conditions, peak values at solar noon are about 1.32 Ly min^{-1} . The diurnal radiation record is highly irregular, with amplitude reductions and duration dependent on cloud type, amount, and duration. Overcast medium-to-thick cirrus attenuates the incoming solar radiation significantly.

(b) Soil surface temperature. Soil surface temperature profiles at station locations roughly approximated a sinusoidal form only on days that were mostly clear. The maximum temperature is seen to occur very close to 1400 EST. The amplitudes of these near-sinusoidal temperature profiles changed with variations in soil surface properties. Cirrus and cumulus cloud attenuation of solar radiation resulted in irregular surface temperature profiles and occasional large reductions in surface temperature. On mostly clear days, maximum values about 45°C were recorded; on days with dense cirrus overcast, maximum values were about 30° to 32°C . Surface temperature drops, caused by rainfall, of 5° to 10°C in an hour were observed.

7.3 Summary of Numerical Modeling Experiments

Information obtained through numerical modeling experiments, relative to the principal objectives, is summarized below.

1) Major differences between heat budget model results and prescribed surface heating functions.

(a) In the heat budget model, air flow interacts with the land surface. Prescribed surface heating functions force temperature changes that would not result if radiative, sensible, and latent heat fluxes were allowed to contribute to surface temperature changes.

(b) In the heat budget model, cooler surface temperatures result when sensible heat and latent heat fluxes increase in response to advection of

cooler or drier air and increase of wind speeds over the surface. Warmer surface temperatures result when fluxes are reduced and wind speeds decrease. These processes act to change the temperature gradient in the lowest levels of the atmosphere. The inland penetration and intensity of the sea breeze are seen to vary depending upon the location and magnitude of these gradients.

(c) In the heat budget model, sea breeze intensities decrease with increasing basic wind flow. The opposite effect occurs in the prescribed heating case.

2) Relative importance of soil surface properties and clouds.

(a) Soil moisture is the most important surface property; albedo is next in importance.

(b) Thermal inertia variations are insignificant when soil moisture is greater than 25%.

(c) Cirrus cloud cover, depending upon its distribution and optical thickness, can severely damp sea breeze intensity or shift the location of the sea breeze several tens of kilometers from its position in a cloud-free atmosphere.

3) Behavior of sea breeze for basic easterly flow regime with heat budget version.

(a) West coast sea breeze is more intense than east coast sea breeze. Maximum intensities of both vary inversely with wind speed.

(b) Greater surface heating on coastal strips results in more intense east coast sea breeze. The inland penetration of the east coast sea breeze is retarded with greater coastal heating.

4) Importance of heat budget components.

(a) Sensible heat flux to the atmosphere from the ground drives the sea breeze circulation. This flux increases with reduced albedo and soil moisture. The sum of evaporation and sensible heat fluxes is essentially constant. Evaporation decreases as sensible heat increases.

(b) Little change is seen in upward and downward IR components during diurnal cycle and among experiments.

5) Importance of evaporation over South Florida.

(a) Predicted low-level moisture values are seriously underestimated if a surface heat budget formulation is not used in the numerical model.

(b) Large variations in the distribution of moisture by the sea breeze circulation can occur as a result of differences in soil moisture content and heating across the peninsula.

Case Study of July 16, 1975:

1) Relative importance of surface properties and clouds in establishing the intensity and movement of the sea breeze.

(a) Surface properties—Differences in cloud (unadjusted) and cloud (adjusted) cases show that the east coast sea breeze decreased by 7% and the west coast sea breeze increased by 51%. These changes resulted from relatively minor changes in soil moisture content. This verifies, again, the importance of surface properties, particularly soil moisture.

(b) Clouds—Large differences in sea breeze location and intensity are seen between cloud (adjusted) and no-cloud (adjusted) cases. For the cloud case, the sea breeze is 33 km farther west at 1600 EST, and intensity is 108% higher. The cumulus cloud field intensifies the low-level temperature gradient by shielding the surface from solar radiation. This intensifies the east coast sea breeze and accelerates it westward. Cloud cover effects must be considered in predicting sea breeze behavior after cloud formation.

2) Degree of realism attained through numerical simulation of this sea breeze event in which observed or deduced surface and cloud properties form the data base for the model.

Observations of the sea breeze vertical motions were not available. The observed surface wind field could be compared with the predicted motion field at the lowest model level (50 m) at 1200 EST and 1300 EST. The coincidence of the predicted convergence zone and observed wind fields was quite good. Beyond 1300 EST the predicted field could not be verified against the observed wind field. However, the predicted convergence zone moved at almost the same speed as the major east coast sea breeze cloud field. This demonstrated that a significant effect should be expected from cumulus cloud shielding of the surface from solar radiation. This shielding intensifies and accelerates the sea breeze convergence zone.

7.4 Conclusions

The observed diurnal soil surface temperature profiles were seen to fall into two classes, sinusoidal and nonsinusoidal. The sinusoidal profiles generally occurred under clear skies. The amplitudes of these temperature profiles were seen to vary in space and time as a result of the variations in surface thermal properties and atmospheric conditions. The nonsinusoidal profiles occurred under partly cloudy to cloudy conditions. These

profiles exhibited large fluctuations in time as a consequence of variable cloud cover which reduced the incoming solar flux. Near-noon surface temperature profiles for the entire study area show highly nonuniform heating in space and highly variable heating from day to day. From the foregoing analysis, it is concluded that model formulations of surface heating which prescribe temperature profiles having uniform amplitudes in space do not realistically simulate observed surface temperatures.

The numerical sensitivity experiments showed the importance of surface properties and clouds in altering the sea breeze circulation. It was found that (1) soil moisture is the dominant controlling surface property, followed by albedo and thermal inertia, (2) clouds can exert an influence which far outweighs the influence exerted by surface property variations, and (3) changes in surface and cloud properties over small space scales result in significant increases in intensity and reduction in speed of the east coast sea breeze convergence zone.

The case study experiment showed that both surface properties and clouds must be considered in simulating an actual sea breeze event. Serious errors in interpretation of model results can occur if the radiation-shielding role of cumulus clouds is not understood.

Predicted sea breeze circulations obtained with models using surface heat budget formulations differ significantly from those models which prescribe surface heating. The former predictions are superior as they evolve in response to realistic interactions between the surface and the atmosphere. From the observational study and the numerical experiments, it is concluded that numerical sea breeze models must include accurate radiation transfer algorithms and surface heat budget formulations.

7.5 Suggestions for Further Research

The three-dimensional sea breeze model developed by Pielke (1974) should be expanded to include radiation and surface heat budget physics and an improved finite difference scheme. The height of the free surface should be raised, because vigorous sea breeze circulations can occur as a result of including the surface heat budget. An improved surface layer turbulent transfer formulation is required for the light wind case. A later generation model should have the capability to predict clouds as a result of moist convective processes. When this model is developed, it should be

verified with observations from a major field experiment designed to study the sea breeze and its associated cloudiness and precipitation.

The data base for these model runs would consist of albedo, thermal inertia, and soil moisture values which were measured or deduced for the study region.

In planning for operational acquisition of data sets to support local mesoscale forecasting, provision should be made for platforms and sensors to obtain soil moisture, albedo, thermal inertia, and cloud optical properties. Satellite platforms with high-resolution (e.g., 1-nmi) microwave radiometers should provide a mapping of soil moisture during clear periods at least once daily. The variation of surface albedo with soil moisture should be known for each soil type. Thermal inertia mapping could be determined reliably from high-resolution (1-nmi), high-frequency ($\frac{1}{2}$ -h) infrared imagery from conventional satellites during hours of darkness. Aircraft observations of cirrus thickness, ice particle number density, and particle dimensions should be correlated with visible and infrared imagery to enable correct optical property specification to be made from satellite data alone.

Ground-based sensors should be strategically located to provide ground truth and backup during periods when satellite data acquisition is not possible. These devices would measure soil surface temperature, evapotranspiration, soil moisture, and downward-directed short- and long-wave radiation. A cooperative, coordinated interdisciplinary program would have to be established to collect, format, and disseminate these data. The expertise would be provided by meteorologists, soil scientists, botanists, hydrologists, and specialists in remote sensing.

8. ACKNOWLEDGMENTS

This work was performed to satisfy both the academic requirements for the Ph.D. degree at the University of Miami and the scientific research objectives of the Merger Task Force at the National Hurricane and Experimental Meteorology Laboratory, Coral Gables, Florida.

A special debt of gratitude is owed to Professor Mariano Estoque, my Ph.D. committee chairman, and committee members Professors John Geisler, Claes Rooth, and Dr. Robert Sax. Thanks are also extended to Professor Eric Kraus, who made it possible for me to study at the University of Miami.

Without the time and facilities provided me by Drs. Noel LaSeur, William Woodley, and

Stanley Rosenthal, this work would not have been possible. My sincere thanks go to Cecilia Griffith for the many hours spent assisting me in satellite interpretation and densitometer operation, to John Cuning for emplacement and monitoring of soil and radiation sensors, to James Dugranrut for the splendid technical assistance rendered in calibrating radiation and soil temperature sensors and processing the data, to Dr. Robert Sax for peninsula-scale temperature profiles, to Jack Thomas for radar echo depictions, to Victor Wiggert and Gloria Doyle for converting digitized radar data into rainfall values, to John Stewart for computer systems and programming support, to Hugh Willoughby for providing technical guidance. Special thanks go to Ronald Holle for photographic support.

The assistance provided by Dr. Roger Pielke is deeply appreciated. Thanks are also extended to Dr. William Cotton for suggestions and support. Without the surface albedo data provided by Joseph Wisniewski, this work would have been adversely affected.

I wish to thank Dr. Walter James Koss and Victor Wiggert for their final reviews and suggested corrections.

9. REFERENCES

- Abramowitz, M., and I. Stegun (1964): *Handbook of Mathematical Functions*. U. S. Govt. Printing Office, Washington, D. C., 1046 pp.
- Bhumralkar, C. M. (1974): Numerical experiments on the computation of ground surface temperature in the atmospheric circulation mode. Defense Advanced Research Projects Agency Rept. R-1511-ARPA, 52 pp.
- Burch, D. E., J. M. Howard and D. Williams (1956): Infrared transmission of synthetic atmospheres. V. Absorption laws for overlapping bands. *J. Opt. Soc. Amer.*, 46:452.
- Businger, J. A. (1973): Turbulent transfer in the atmospheric surface layer. *Workshop in Micrometeorology*, Amer. Meteorol. Soc., Boston, Massachusetts, Chapter 2.
- Carlsaw, H. S., and J. C. Jaeger (1959): *Conduction of Heat in Solids*. 2nd ed., Oxford University Press, New York, 510 pp.
- Coantic, M., and B. Seguin (1971): On the interaction of turbulent and radiative transfers in the surface layer. *Boundary Layer Meteorol.*, 1:245.
- Cotton, W. R., and R. A. Pielke (1976): Weather modification and three-dimensional models. *Bull. Amer. Meteorol. Soc.*, 57:788.
- Coulson, K. L., and D. W. Reynolds (1971): The spectral reflectance of natural surfaces. *J. Appl. Meteorol.*, 10:1285.
- Cox, S. K. (1973): Infrared heating calculations with a water vapour pressure broadened continuum. *Q. J. R. Meteorol. Soc.*, 99:669.
- Danielson, R. E., D. R. Moore and H. C. van de Hulst (1969): The transfer of visible radiation through clouds. *J. Atmos. Sci.*, 26:1078.
- Deardorff, J. (1974): Three-dimensional numerical study of the height and mean structure of a heated planetary boundary layer. *Boundary Layer Meteorol.*, 7:81.
- Drummond, A. J., and J. R. Hickey (1971): Large-scale reflection and absorption of solar radiation by clouds as influencing earth radiation budgets: new aircraft measurements. *Proc. Int. Conf. Wea. Mod.*, Canberra, Australia, 267-276.
- Drummond, A. J., and M. P. Thekaekara (1973): *The Extraterrestrial Solar Spectrum*. Institute of Environmental Sciences, Mount Prospect, Illinois, 169 pp.
- Elzeftawy, A. and R. S. Mansell (1975): Hydraulic conductivity calculations for unsaturated steady-state and transient-state flow in sand. *Proc. Soil Sci. Soc. Amer.*, 39:599.
- Environmental Science Services Administration (1968): *Climatic Atlas of the United States*. Environmental Data Service, U. S. Govt. Printing Office, Washington, D. C.
- Estoque, M. A. (1962): The sea breeze as a function of the prevailing synoptic situation. *J. Atmos. Sci.*, 68:1103.
- Estoque, M. A. (1973): A numerical model of the atmospheric boundary layer. *J. Geophys. Res.*, 68:1103.
- Estoque, M. A., and C. M. Bhumralkar (1969): Flow over a localized heat source. *Mon. Wea. Rev.*, 97:850.
- Estoque, M. A., J. Gross and H. W. Lai (1976): A lake breeze over southern Lake Ontario. *Mon. Wea. Rev.*, 104:386.
- Fisher, E. L. (1960): An observational study of the sea breeze. *J. Meteorol.*, 17:645.
- Fleagle, R. G., and J. A. Businger (1963): *An Introduction to Atmospheric Physics*. Academic Press, New York, 346 pp.
- Fleming, J. R., and S. K. Cox (1974): Radiative effects of cirrus clouds. *J. Atmos. Sci.*, 31:2182.
- Garstang, M. (1974): Combined observing and seeding experiment. Final Rep., Dept. of Environmental Sciences, University of Virginia, Charlottesville, Virginia, 45 pp.
- Gooding, E. G. B. (1972): Plant responses to tropical conditions. *Proc. WMO Seminar on Agricultural Meteorol.*, Barbados, 1970, WMO No. 310, Geneva, pp. 71-77.
- Gray, W. M., W. M. Frank, M. L. Corrin and C. A. Stokes (1974): Weather modification by carbon dust absorption of solar energy. *Atmospheric Science Paper No. 225*, Dept. of Atmospheric Science, Colorado State University, Ft. Collins, Colorado, 191 pp.
- Gray, W. M., W. M. Frank, M. L. Corrin and C. A. Stokes (1976): Weather modification through carbon dust absorption of solar energy. *J. Appl. Meteorol.*, 15:355.

- Griffith, C. G., W. L. Woodley, S. Browner, J. Teijeiro, M. Maier, D. W. Martin, J. Stout and D. N. Sikdar (1976): Rainfall estimation from geosynchronous satellite imagery during daylight hours. NOAA Tech. Rep. ERL 356-WMPO 7, 106 pp.
- Hill, G. E. (1974): Factors controlling the size and spacing of cumulus clouds as revealed by numerical experiments. *J. Atmos. Sci.*, 31:646.
- Holmes, R. M., and G. W. Robertson (1963): Application of the relationship between actual and potential evapotranspiration in dry land agriculture. *Trans. Amer. Soc. Agricultural Engineers*, 6:65.
- Hsu, S. (1969): Mesoscale structure of the Texas coast sea breeze. Rep. 16, College of Engineering, University of Texas, Austin, Texas, 237 pp.
- Idso, S. B. (1975): Net radiation—soil heat flux relations as influenced by soil water content variations. *Boundary Layer Meteorol.*, 9:113.
- Idso, S. B., T. J. Schmugge, R. D. Jackson and F. J. Reginato (1975): The utility of surface temperature measurements for the remote sensing of surface soil water status. *J. Geophys. Res.*, 80:3044.
- Irvine, W. M., and J. B. Pollack (1968): Infrared optical properties of water and ice spheres. *Icarus*, 8:324.
- Johnson, R. H. (1977): Effects of cumulus convection on the structure and growth of the mixed layer over south Florida. *Mon. Wea. Rev.*, 105:713.
- Kahle, A. B., A. R. Gillespie, A. F. H. Goetz and J. D. Addington (1975): Thermal inertia mapping. In Preprint, Tenth Int. Symp. on Remote Sensing of Environment, Ann Arbor, Michigan, 985-994.
- Kaiser, J. A. C., and R. H. Hill (1976): Irradiance at sea. *J. Geophys. Res.*, 81:395.
- Kondratyev, K. Ya. (1969): *Radiation in the Atmosphere*. Academic Press, New York, 912 pp.
- Kung, E. C., R. A. Bryson and D. H. Lenschow (1964): Study of a continental surface albedo on the basis of flight measurements and structure of the earth's surface cover over North America. *Mon. Wea. Rev.*, 92:543.
- Lacis, A. A., and J. E. Hansen (1974): A parameterization for the absorption of solar radiation in the earth's atmosphere. *J. Atmos. Sci.*, 31:118.
- Liou, K. N. (1972): Light scattering by ice clouds in the visible and infrared: a theoretical study. *J. Atmos. Sci.*, 29:524.
- Liou, K. N. (1973): Transfer of solar irradiance through cirrus cloud layers. *J. Geophys. Res.*, 78:1409.
- Liou, K. N. (1974): On the radiative properties of cirrus in the window region and their influence on remote sensing of the atmosphere. *J. Atmos. Sci.*, 31:522.
- Lund, I. A. (1972): Haze-free and cloud-free lines-of-sight through the atmosphere. Environmental Research Papers, No. 413, Air Force Cambridge Research Laboratories, Bedford, Massachusetts, 16 pp.
- Mak, M. K. (1974): A study of the role of radiational cooling in a planetary boundary layer. *Mon. Wea. Rev.*, 102:201.
- McKee, T. B., and S. K. Cox (1974): Scattering of visible radiation by finite clouds. *J. Atmos. Sci.*, 31:1885.
- McPherson, R. D. (1968): A three-dimensional numerical study of the Texas coast sea breeze. Rep. 15, NSF Grant GA-367X, University of Texas at Austin, College of Engineering, Atmospheric Science Group, 252 pp.
- Monteith, J. L. (1975): *Vegetation and the Atmosphere*. Academic Press, Inc. (London) Ltd., 278 pp.
- Moroz, W. J. (1967): A lake breeze on the eastern shore of Lake Michigan: observations and model. *J. Atmos. Sci.*, 24:337.
- Nappo, C. J., Jr. (1975): Parameterization of surface moisture and evaporation rate in a planetary boundary layer model. *J. Appl. Meteorol.*, 14:289.
- National Aeronautics and Space Administration (1974): SKYLAB Earth Resources Data Catalog. Lyndon B. Johnson Space Center, Houston, Texas, 393 pp.
- National Oceanic and Atmospheric Administration (1975): *Climatological Data for Florida*. Environmental Data Service, Vol. 79, No. 7, Asheville, North Carolina, 10 pp.
- Neumann, J., and Y. Mahrer (1975): A theoretical study of the lake and land breezes of circular lakes. *Mon. Wea. Rev.*, 103:474.
- Otterman, J. (1975): Possible rainfall reduction through reduced surface temperatures due to overgrazing. Preprint X-910-75-93, NASA, Goddard Space Flight Center, Greenbelt, Maryland, 43 pp.
- Pearson, R. A. (1973): An analytical and numerical model of the sea breezes. Ph.D. Dissertation, University of Miami, Coral Gables, Florida, 292 pp.
- Philip, J. R. (1957): Evaporation, and moisture and heat fields in the soil. *J. Meteorol.*, 14:354.
- Pielke, R. A. (1973): A three-dimensional numerical model of the sea breezes over south Florida. NOAA Tech. Memo. ERL WMPO-2, 136 pp.
- Pielke, R. A. (1974): A three-dimensional numerical model of the sea breezes over south Florida. *Mon. Wea. Rev.*, 102:115.
- Pielke, R. A., and W. R. Cotton (1977): A mesoscale analysis over south Florida for a high rainfall event. *Mon. Wea. Rev.*, 105:343.
- Pielke, R. A., and Y. Mahrer (1975): Technique to represent the planetary boundary layer in mesoscale models with coarse vertical resolution. *J. Atmos. Sci.*, 32:2144.
- Pielke, R. A., and Y. Mahrer (1976): Verification analysis of a three-dimensional mesoscale model prediction over south Florida for July 1, 1973. Unpublished paper, Dept. of Environmental Sciences, University of Virginia, Charlottesville, Virginia, 26 pp.
- Plank, V. G. (1962): The characteristics of cumulus cloud populations at the local and mesosynoptic scales. Projects 5038 and 8620, Air Force Cambridge Research Laboratory, Bedford, Massachusetts, 250 pp.
- Platt, C. M. R. (1975): Infrared emissivity of cirrus—simultaneous satellite, lidar, and radiometric observations. *Q. J. R. Meteorol. Soc.*, 101:119.
- Pochop, L. O., and M. D. Shanklin (1966): Sky cover photograms, a new technique. *Weatherwise*, 19:198.
- Pohn, H. A., T. W. Offield and K. Watson (1974): Thermal inertia mapping from satellite-discrimination of geologic units in Oman. *J. Res., U. S. Geol. Survey*, 2:147.

- Priestley, C. H. B., and R. J. Taylor (1972): On the assessment of surface heat flux and evaporation using large-scale parameters. *Mon. Wea. Rev.*, 100:81.
- Salter, P. J., and J. B. Williams (1965): The influence of texture on the moisture release characteristics of soils, II: Available-water capacity and moisture release characteristics. *J. Soil Sci.*, 16:310.
- Sasamori, T. (1968): The radiative cooling calculation for application to general circulation experiments. *J. Appl. Meteorol.*, 7:721.
- Sasamori, T. (1970): A numerical study of atmospheric and soil boundary layers. *J. Atmos. Sci.*, 27:1122.
- Sasamori, T., J. London and D. V. Hoyt (1972): Radiation budget of the Southern Hemisphere. Ch. 2, Meteorol. Mono. 13, No. 35, Amer. Meteorol. Soc., Boston, Massachusetts, 9-23.
- Shaffer, W. A., and P. E. Long, Jr. (1975): A predictive boundary layer model. NOAA Tech. Memo. NWS TDL-57, Techniques Development Laboratory, Silver Spring, Maryland, 44 pp.
- Staff, Cumulus Group (1976): 1975 Florida Area Cumulus Experiment (FACE): Operational summary. NOAA Tech. Memo. ERL WMPO-28, Wea. Mod. Program Office, Boulder, Colorado, 186 pp.
- Stern, M. E., and J. S. Malkus (1953): The flow of a stable atmosphere over a heated island, Part II. *J. Meteorol.*, 10:105.
- Suomi, V. E., D. O. Staley and P. M. Kuhn (1958): A direct measurement of infrared radiation divergence to 160 mb. *Q. J. R. Meteorol. Soc.*, 84:134.
- Sutton, O. G. (1953): *Micrometeorology: A Study of Physical Processes in the Lowest Layers of the Earth's Atmosphere*. McGraw-Hill, New York, 333 pp.
- Tag, P. M. (1969): Surface temperatures in an urban environment. Part I, Atmospheric modification by surface influences. Rep. 15, NSF Grant GA-3956, Dept. of Meteorology, Pennsylvania State U., University Park, Pennsylvania, 132 pp.
- Thekaekara, M. P. (1974): Extraterrestrial solar spectrum, 3000-6100 Å at 1-Å intervals. *Appl. Optics*, 13:518.
- Tingle, A. G. (1971): A numerical model of the Lake Michigan lake breeze, including a review of theoretical and observational studies of coastal wind circulations. Ph.D. Dissertation, University of Michigan, Ann Arbor, Michigan, 151 pp.
- University of Florida Institute of Food and Agricultural Sciences (IFAS), (1975): Mid-term report on models to predict earth-air interface temperature regimes during freeze conditions. Contract No. NAS10-8774, NASA, Kennedy Space Center, Cape Canaveral, Florida, 40 pp.
- U. S. Dept. of Agriculture (1960): Applying basic soil water data to water control programs in Everglades peaty muck. Agricultural Research Service, 41-40, 15 pp.
- U. S. Dept. of Agriculture (1971): Soil survey, Okeechobee County, Florida. U. S. Govt. Printing Office, Washington, D. C., 62 pp.
- U. S. Dept. of Interior (1974): Water resources data for Florida, Part 2. Surface water quality records. Geological Survey, Miami, Florida.
- van Bavel, C. H. M., C. B. Stirk and K. J. Brust (1968): Hydraulic properties of a clay loam soil and the field measurement of water uptake by roots: I. Interpretation of water content and pressure profiles. II. The water balance of the root zone. *Soil Sci. Soc. Amer. Proc.*, 32:310.
- Walsh, J. E. (1974): Sea breeze theory and applications. *J. Atmos. Sci.*, 31:2012.
- Watson, G. F. (1971): A diagnostic study of the kinematical and physical processes maintaining a strong low-level subsidence inversion over land. Ph.D. Dissertation, Florida State University, Tallahassee, Florida, 150 pp.
- Watson, K. (1970): Remote sensor application studies progress report, July 1, 1968, to June 30, 1969. U. S. Geological Survey Rept., USGS-GD-71-004, Denver, Colorado, 50 pp.
- Watson, K. (1971): A computer program of thermal modeling for interpretation of infrared images. U. S. Geological Survey Rept. USGS-GD-71-023, Denver, Colorado, 33 pp.
- Watson, K. (1975): Geologic applications of thermal infrared images. Proc. Inst. Electrical and Electronics Engineers, 63:128-137.
- Watson, K., L. C. Rowan and T. W. Offield (1971): Application of thermal modeling in the geologic interpretation of IR images. Seventh Int. Symp. Remote Sensing of Environment, Ann Arbor, Michigan, Vol. 3, 2017-2042.
- Weiss, C. E., and J. F. Purdom (1974): The effect of early-morning cloudiness on squall-line activity. *Mon. Wea. Rev.*, 102:400.
- Woodley, W. L., and R. I. Sax (1976): The Florida Area Cumulus Experiment: rationale, design, procedures, results, and future course. NOAA Tech. Report ERL 354-WMPO 6, 204 pp.
- Yong, R. N., and B. P. Warkentin (1975): *Soil Properties and Behavior; Developments in Geotechnical Engineering*, 5. Elsevier, New York, 449 pp.
- Yu, T., and N. K. Wagner (1975): Numerical study of the nocturnal urban boundary layer. *Boundary Layer Meteorol.*, 9:143.
- Zilitinkevich, S. S. (1970): *Dynamics of the Atmospheric Boundary Layer*. Gidrometeoizdat, Leningrad, 291 pp. (National Lending Library for Science and Technology, Translation 647, Boston Spa, Yorks., 1972.)

10. BIBLIOGRAPHY

- Arakawa, A. (1972): Design of the UCLA general circulation model. Numerical simulation of weather and climate. Tech. Rept. No. 7, Dept. of Meteorol., University of California, Berkeley, California, July, 116 pp.
- Baier, W. (1965): The interrelationship of meteorological factors, soil moisture and plant growth. *Int. J. Biometeorol.*, 9:5.

- Bhumralkar, C. M. (1972): An observational and theoretical study of atmospheric flow over a heated island. Ph.D. Dissertation, The University of Miami, Coral Gables, Florida, 150 pp.
- Bhumralkar, C. M. (1975): A survey of parameterization techniques for the planetary boundary layer in atmospheric circulation models. Defense Advanced Research Projects Agency Rept. R-1653-ARPA, 84 pp.
- Black, J. F. (1963): Weather control: use of asphalt coatings to tap solar energy. *Science*, 139:226.
- Bradley, J. T. (1974): The climate of Florida. *Climates of the States*, Vol. 1 (Eastern States [plus Puerto Rico and the U. S. Virgin Islands]). A Water Information Center Publication, NOAA, U. S. Dept. of Commerce, 480 pp.
- Brunt, D. (1944): *Physical and Dynamical Meteorology*. 2nd ed. Cambridge University Press, London, 428 pp.
- Brutsaert, W. (1975): The roughness length for water vapor, sensible heat, and other scalars. *J. Atmos. Sci.*, 32:2028.
- Carlson, T. N., J. M. Prospero and K. J. Hanson (1973): Attenuation of solar radiation by windborne Saharan dust off the west coast of Africa. NOAA Tech. Memo. ERL WMPO-7, Wea. Mod. Program Office, Boulder, Colorado, 27 pp.
- Charney, J., P. H. Stone and W. J. Quirk (1975): Drought in the Sahara: a biogeophysical feedback mechanism. *Science*, 187:434.
- Charney, J., and P. H. Stone (1975): Technical comments on "Drought in the Sahara: insufficient biogeophysical feedback?" *Science*, 191:100.
- Cotton, W. R. (1974): Data requirements for verification and development of models on the cumulus scale. *Proc. Third Symp. Meteorol. Obs. and Instr.*, Washington, D. C., 1-4.
- Cotton, W. R., R. A. Pielke and P. T. Gannon (1976): Numerical experiments on the influence of the meso-scale circulation on the cumulus scale. *J. Atmos. Sci.*, 33:252.
- Cox, S. K., and S. L. Hastenrath (1970): Radiation measurements over the equatorial central Pacific. *Mon. Wea. Rev.*, 98:823.
- Denmead, O. T., and R. H. Shaw (1962): Availability of soil water to plants as affected by soil moisture content and meteorological conditions. *Agronomy J.*, 54:385.
- Elsasser, W. M., and M. F. Culbertson (1960): *Atmospheric radiation tables*. Meteorol. Mono., 4, No. 23 Amer. Meteorol. Soc., Boston, Massachusetts, 43 pp.
- Frizzola, J. A., and E. L. Fisher (1963): A series of sea breeze observations in the New York City area. *J. Appl. Meteorol.*, 2:722.
- Geiger, R. (1950): *The Climate Near the Ground*. Harvard University Press, Cambridge, Massachusetts, 482 pp.
- Geisler, J. E., and F. P. Bretherton (1969): The sea breeze forerunner. *J. Atmos. Sci.*, 26:82.
- Hammond, L. C., and R. S. Mansell (1972): Soil hydraulics and waste water renovation. University of Florida Institute of Food and Agricultural Sciences (IFAS) Waste Water Workshop, Tampa, Florida.
- Haurwitz, B. (1941): *Dynamic Meteorology*. McGraw-Hill, New York, 365 pp.
- Haurwitz, B. (1947): Comments on the sea breeze circulation. *J. Meteorol.*, 4:1.
- Higer, A. L., A. G. Coker, E. H. Cordes and R. H. Rogers (1975): Water-management model in Florida from ERTS-1 data. U. S. Dept. of the Interior, Geological Survey, Final Rpt., Miami, Florida.
- Hudson, J. C. (1963): Work on micro- and macrometeorology, sugar cane growth, and water use, etc. Bulletins No. 33, 34, 38, and 40, Ministry of Agriculture, Barbados.
- Idso, S. B., and W. L. Ehler (1976): Estimating soil moisture in the root zone of crops: a technique adaptable to remote sensing. *Geophys. Res. Letters*, 3:23.
- Jackson, R. D., B. A. Kimball, R. J. Reginato and F. S. Nakayama (1973): Diurnal soil-water evaporation: time-depth-flux patterns. *Soil Sci. Soc. Amer. Proc.*, 37:505.
- Jackson, R. D., and S. D. Idso (1975): Surface albedo and desertification. *Science*, 189:1012.
- Knipling, E. B. (1970): Physical and physiological basis for the reflectance of visible and near-infrared radiation from vegetation. *Remote Sensing of Environment*, 1: 155-159.
- Kraus, R. B. (1972): *Atmosphere-Ocean Interaction*. Oxford University Press, London, 275 pp.
- Kuo, H. L. (1968): The thermal interaction between the atmosphere and the earth and propagation of diurnal temperature waves. *J. Atmos. Sci.*, 25:682.
- Lettau, H. H., and B. Davidson (1957): *Exploring the Atmosphere's First Mile*. Pergamon, New York, Vol. 1, 376 pp.; Vol. 2, 578 pp.
- Lyons, W. A. (1972): The climatology and prediction of the Chicago lake breeze. *J. Appl. Meteorol.*, 11:1259.
- McElroy, J. L. (1972a): A numerical model of the nocturnal urban boundary layer. *Proc. Symp. on Air Pollution, Turbulence, and Diffusion*. Las Cruces, New Mexico, 1971, New Mexico State U. and Sandia Laboratories, 116-121.
- McElroy, J. L. (1972b): Effects of alternate land-use strategies on the structure of the nocturnal urban boundary layer. *Preprints, Conf. on Urban Environment*, Amer. Meteorol. Soc., Philadelphia, 185-190.
- McNaughton, K. G. (1976a): Evaporation and advection I: evaporation from extensive homogeneous surfaces. *Q. J. R. Meteorol. Soc.*, 102:181.
- McNaughton, K. G. (1976b): Evaporation and advection II: evaporation down-wind of a boundary separating regions having different surface resistances and available energies. *Q. J. R. Meteorol. Soc.*, 102:193.
- Murcray, D. G., J. N. Brooks, F. H. Murray and W. J. Williams (1974): 10- to 12- μ spectral emissivity of a cirrus cloud. *J. Atmos. Sci.*, 31:1940.
- National Aeronautics and Space Administration (1969): Nimbus Project. Nimbus III User's Guide, Goddard Space Flight Center, Greenbelt, Maryland.
- National Aeronautics and Space Administration (1970): Nimbus Project. Nimbus IV User's Guide, Goddard Space Flight Center, Greenbelt, Maryland.
- National Aeronautics and Space Administration (1975): Agriculture—Environment. *Proc. NASA Earth Resources Survey Symp.*, Vol. 1-a, Houston, Texas, 598 pp.

- Nickerson, E. C., and V. E. Smiley (1975): Surface layer and energy budget parameterizations for mesoscale models. *J. Appl. Meteorol.*, 14:297.
- Orlanski, I. (1975): A rational subdivision of scales for atmospheric processes. *Bull. Amer. Meteorol. Soc.*, 56:527.
- Otterman, J. (1975): Reply to "Surface albedo and desertification." *Science*, 189:1013.
- Otterman, J., and R. S. Fraser (1975): Earth-atmosphere system and surface reflectances in arid regions from LANDSAT multispectral scanner measurements. NASA Goddard Space Flight Center, Greenbelt, Maryland, 25 pp.
- Pielke, R. A. (1974): A comparison of three-dimensional and two-dimensional numerical predictions of sea breezes. *J. Atmos. Sci.*, 31:1577.
- Planet, W. G. (1969): Some comments on reflectance measurements of wet soils. *Remote Sensing of Environment* 1: 127-129.
- Rao, P. K. (1975): "Invisible" cirrus clouds in NOAA-2 VHRR imagery. *Mon. Wea. Rev.*, 103:72.
- Ripley, E. A. (1975): Drought in the Sahara: insufficient biogeophysical feedback? *Science*, 191:100.
- Schmugge, T., P. Gloersen, T. Wilheit and F. Geiger (1974): Remote sensing of soil moisture with microwave radiometers. *J. Geophys. Res.*, 79:317.
- Sellers, W. D. (1965): *Physical Climatology*. The University of Chicago Press, Chicago and London, 272 pp.
- Sethuraman, S. (1976): Air mass modification due to change in surface characteristics. *Mon. Wea. Rev.*, 104:1040.
- Staff, Experimental Meteorology Laboratory (1974): 1973 Florida Area Cumulus Experiment (FACE): operational and preliminary summary, NOAA Tech. Memo. ERL WMPO-12, Wea. Mod. Program Office, Boulder, Colorado, 254 pp.
- Van Wijk, W. R. (1965): *Soil microclimate, its creation, observation, and modification*. Meteorol. Mono. 6, No. 28, Amer. Meteorol. Soc., Boston, Massachusetts, 59-73.
- Vukovich, F. M. (1973): A study of the atmospheric response due to a diurnal heating function characteristic of an urban complex. *Mon. Wea. Rev.*, 101:467.
- Webb, E. K. (1965): *Aerial microclimate*. Meteorol. Mono. 6, No. 27, Amer. Meteorol. Soc., Boston, Massachusetts.
- Weisman, R. N. (1975): A developing boundary layer over an evaporating surface, *Boundary Layer Meteorol.*, 8:437.
- Woodley, W. L., A. Olsen, A. Herndon and V. Wiggert (1974): Optimizing the measurement of convective rainfall in Florida. NOAA Tech. Memo. ERL WMPO-18, Wea. Mod. Program Office, Boulder, Colorado, 99 pp.
- World Meteorological Organization (1972): The application of micrometeorology to agricultural problems. Rept. of the Working Group on Agrometeorological Aspects of Micrometeorology of the Commission for Agricultural Meteorology, ed. L. P. Smith, WMO No. 298, Geneva, 74 pp.
- Yamamoto, G. (1962): Direct absorption of solar radiation by atmospheric water vapor, carbon dioxide, and molecular oxygen. *J. Atmos. Sci.*, 19:182.

APPENDIX A

RADIATION TRANSFER EQUATIONS

A.1. OZONE ATTENUATION

The ozone path length is defined as

$$u(h) = \frac{a + a \exp(-b/c)}{1 + \exp[(h-b)/c]}$$

where $u(h)$ is the ozone amount (cm NTP) in a vertical column above altitude h , a is the total ozone amount in a vertical column above the ground, b the altitude at which the ozone concentration has its maximum value, and c an adjusted constant. The values of a , b , and c chosen for this experiment were based upon a midlatitude winter ozone distribution (Lacis and Hansen, 1974). It was believed that this distribution would be more representative of 26°30'N. A typical amount of ozone in a vertical column of the atmosphere is 0.4 cm NTP. The value of h was chosen as zero to account for total absorption above the ground. Heating caused by ozone absorption below 9 km is vanishingly small. Following are the values of the parameters in the ozone distribution function:

$$\begin{aligned} a &= 0.4 \text{ cm} \\ b &= 20.0 \text{ km} \\ c &= 5.0 \text{ km} \\ h &= 0.0 \text{ km} \end{aligned}$$

The optical path length $u(h)$ is multiplied by a magnification factor M where

$$M = \frac{35}{(1224\mu_0^2 + 1)^{1/2}}$$

The quantity μ_0 is the solar zenith angle.

The absorption parameterization for the ultraviolet (0.29 μm to 0.38 μm) is

$$A_{\text{OZ}}^{\text{UV}} = \frac{1.082 \times}{(1 + 138.6 \times)^{0.805}} + \frac{0.0658 \times}{1 + (103.6 \times)^3}$$

$A_{\text{OZ}}^{\text{UV}}$ is the fraction of the total solar flux which is absorbed by ozone in the ultraviolet. The product $\times = M \cdot u(h)$ is the effective path length resulting from refraction and the angular difference of the solar beam from the zeroth zenith angle.

The absorption parameterization for the visible (0.46 μm to 0.695 μm and 0.695 μm to 0.75 μm) is

$$A_{\text{OZ}}^{\text{VIS}} = \frac{0.02118 \times}{1 + 0.042 \times + 0.000323 \times^2}$$

$A_{\text{OZ}}^{\text{VIS}}$ is the fraction of the total solar flux which is absorbed by ozone in the visible region.

The solar spectral energy is defined by S_i where the index refers to the appropriate spectral energy intervals given in table 4. The spectral energy (S_i) remaining after ozone absorption is

$$S_1 = (S_1 - A_{\text{OZ}}^{\text{UV}} \cdot \bar{S}) \cos \mu_0$$

$$S_3 = (S_3 - A_{\text{OZ}}^{\text{VIS}} \cdot \bar{S} \cdot 0.848) \cos \mu_0$$

$$S_4 = (S_4 - A_{\text{OZ}}^{\text{VIS}} \cdot \bar{S} \cdot 0.152) \cos \mu_0.$$

$\bar{S} = 0.03230964 \text{ cal cm}^{-2} \text{ s}^{-1}$ (1.9385784 $\text{cal cm}^{-2} \text{ min}^{-1}$). \bar{S} is the solar constant as derived from tabular data in Thekaekara (1974). It does not include solar energy at wavelengths $< 0.29 \mu\text{m}$. The factor 0.848 in S_3 is the fraction of the ozone-attenuated visible spectral energy interval occupied by S_3 . The remainder of this interval is occupied by S_4 ; thus the factor 0.152 is used.

A.2. CIRRUS TRANSFER

All incoming solar radiation is direct radiation until it is subjected to cirrus or atmospheric scattering. Then both direct and diffuse radiation must be considered. The equations to be solved (Liou, 1973) are

Downward flux:

$$F\downarrow(\tau) = v \text{Exp}(c\tau) \cdot K + u \cdot \text{Exp}(-c\tau) \cdot H + \epsilon \cdot \text{Exp}(-\tau/\mu_0); \quad (\text{A.1})$$

Upward flux:

$$F\uparrow(\tau) = u \cdot \text{Exp}(c\tau) \cdot K + v \cdot \text{Exp}(-c\tau) \cdot H + \gamma \cdot \text{Exp}(-\tau/\mu_0); \quad (\text{A.2})$$

where τ is optical thickness.

The terms in $F\downarrow(\tau)$ and $F\uparrow(\tau)$ are defined as follows:

$$\begin{aligned} v &= (1-a)/2 & u &= (1+a)/2 \\ \epsilon &= (\alpha + \beta)/2 & \gamma &= (\alpha - \beta)/2 \\ c^2 &= (1-\tilde{\omega}_0)(1-\tilde{\omega}_0 g) / \langle \mu \rangle^2 & a^2 &= (1-\tilde{\omega}_0) / (1-\tilde{\omega}_0 g) \\ \alpha &= \frac{\pi \mu_0 F_0 [(1-\tilde{\omega}_0 g) \mu_0^2 (q\downarrow + q\uparrow) + \mu_0 \langle \mu \rangle (q\downarrow - q\uparrow)]}{\langle \mu \rangle^2 (c^2 \mu_0^2 - 1)} \end{aligned}$$

$$\beta = \frac{\pi \mu_0 F_0 [(1 - \tilde{\omega}_0) \mu_0^2 (q \downarrow - q \uparrow) + \mu_0 < \mu > (q \downarrow + q \uparrow)]}{< \mu >^2 (c^2 \mu_0^2 - 1)}$$

μ_0 : Cosine of solar zenith angle
 πF_0 : Incident solar flux normalized to unity
 g : $< \cos \Theta >$ (Asymmetry factor)
 $< \mu >$: $\mu_0 (q \downarrow + q \uparrow)$.

The constants K and H , determined by the appropriate boundary conditions, are

$$K = \frac{-\{\epsilon(v - u A_c) \exp(-c\tau_n) + [(1 + \epsilon) A_c - \gamma] u \exp(-\tau_n/\mu_0)\}}{v(v - A_c u) \exp(-c\tau_n) - u(u - A_c v) \exp(c\tau_n)}$$

$$H = \frac{\{\epsilon(u - v A_c) \exp(c\tau_n) + [(1 + \epsilon) A_c - \gamma] v \exp(-\tau_n/\mu_0)\}}{v(v - A_c u) \exp(-c\tau_n) - u(u - A_c v) \exp(c\tau_n)}.$$

K and H are used in (A.1) and (A.2).

A_c is the albedo of underlying cirrus layers. A_c is set equal to zero, because only one cirrus layer is assumed for the present work. In the present context, A_c is relevant only for treatment of the heating of the atmospheric layer that has the cirrus. This heating is irrelevant for this paper.

The quantity $q \downarrow$ in α , β , and $< \mu >$ is the total downward incident flux at the bottom of the cirrus layer recovered after scattering processes in the layer. The quantity $q \uparrow$ is the flux in the upward direction.

$$q = \pi F_0 \mu_0 \frac{1}{2} \sum_{\ell=0}^N \tilde{\omega}_\ell p_\ell(\mu_0) \int_0^{\pm 1} p_\ell(\mu) \mu d\mu \quad (A.3)$$

$\pi F_0 \mu_0$ is the total incident solar flux (after ozone absorption and scattering).

$\tilde{\omega}_\ell (\ell = 0, 1, \dots, N)$ are a series of $N + 1$ constants determined by

$$\tilde{\omega}_\ell = \frac{2\ell + 1}{2} \int_{-1}^{+1} P(\cos \Theta) p_\ell(\cos \Theta) d \cos \Theta \quad (A.4)$$

$\tilde{\omega}_0$ is the single-scattering albedo.

Θ is the scattering angle.

$P(\cos \Theta)$ is the phase function.

$p_\ell(\cos \Theta)$ is the ℓ th Legendre polynomial term.

$p_\ell(\mu_0)$ is the ℓ th Legendre polynomial term as a function of the solar zenith angle.

μ is the emergent angle of the solar beam after transiting the cirrus layer.

$p_\ell(\mu)$ is the ℓ th Legendre polynomial term as a function of the emergent angle of solar beam.

The integral

$$\tilde{\omega}_\ell = \frac{2\ell + 1}{2} \int_{-1}^{+1} P(\cos \Theta) p_\ell(\cos \Theta) d \cos \Theta$$

was calculated using

$$\tilde{\omega}_\ell = \sum_{\ell=1}^{40} \sum_{m=1}^{120} \tilde{\omega}_0 \cdot P_m(\cos \Theta) \cdot \text{LEG}_{\ell,m} \cdot \text{DEL} \quad (A.5)$$

$\text{DEL} = 0.01666666$. $\text{LEG}_{\ell,m}$ is the Legendre polynomial value calculated from $\cos \Theta = -1$ to $\cos \Theta = +1$ at each increment DEL . The appropriate phase function value $P_m(\cos \Theta)$ for each increment was a factor in the summation. Thus, 40 values of $\tilde{\omega}_\ell$ are calculated for each of the eight spectral ranges used in cirrus transfer.

In (A.3), the integral

$$\int_0^{\pm 1} p_\ell(\mu) \mu d\mu$$

($\mu > 0$ for $q \downarrow$; $\mu < 0$ for $q \uparrow$)

was evaluated by means of a gamma function subprogram used to evaluate

$$\int_0^{\pm 1} p_\ell(\mu) \mu d\mu = \frac{\pi^{1/2} \Gamma(2)}{4\Gamma(\frac{3}{2} - \frac{\ell}{2}) \Gamma(2 + \frac{\ell}{2})} \quad (A.6)$$

which derives from Abramowitz and Stegun (1964). q , together with other solar zenith angle dependent variables, is then calculated in the cirrus subroutine every half hour. At these times, 40 Legendre polynomial values for the current value of μ_0 are calculated for (A.3).

Finally, the 24 diffuse components of downcoming radiation flux at the base of the cirrus are calculated. The transmission for each spectral interval is

$$t = \frac{F \downarrow(\tau)}{\pi \mu_0 F_0}$$

where πF_0 is normalized (to unity) solar flux perpendicular to top of cirrus layer. For each spectral interval, the downward flux at base of cirrus layer is then

$$F_{ai} \downarrow(\tau) = t_i S_i$$

where i refers to the appropriate spectral interval.

The 24 direct radiation components are calculated with

$$D_{ai}(\tau) = \bar{S} \cdot \mu_0 \cdot \exp(-\tau/\mu_0) \quad (A.7)$$

where \bar{S} is the total spectral energy after ozone absorption.

A.3. SHORT-WAVE RADIATION TRANSFER BELOW THE CIRRUS LAYER

That spectral energy not affected by water vapor absorption, yet subjected to atmospheric scattering and cloud particle scattering, absorption, and transmission after passing through ozone and cirrus, is

S_i for $i = 1, 2, 3, 5, 7, 9, 11, 13, 21$, and 22 (table 4 of section 4).

For convenience, the direct radiation is defined by

$$D_a = \Sigma D_{ai} \quad (i = 1, 2, 3, 5, 7, 9, 11, 13, 21, \text{ and } 22)$$

where the a denotes this spectral energy category. Similarly, the diffuse radiation is

$$F_a = \Sigma F_{ai} \quad (i = 1, 2, 3, 5, 7, 9, 11, 13, 21, \text{ and } 22).$$

The initial attenuation is due to Rayleigh scattering by atmospheric molecules before interception by low clouds.

$$\begin{aligned} D_a &= D_a (1 - R_r(\mu_0)) \\ F_a &= F_a (1 - R_r(\mu_0)) \end{aligned}$$

where

$$R_r(\mu_0) = \frac{0.28}{1 + 6.43 \mu_0}$$

$R_r(\mu_0)$ is the spherical albedo of the Rayleigh atmosphere (Lacis and Hansen, 1974).

The heating of the layer constituting the cloud for these spectral intervals is neglected. As Lacis and Hansen (1974) point out, cloud particle absorption is only about 5% of the total solar flux. As the cumulus clouds change character rapidly, calculation of the heating caused by absorption by cloud particles is not feasible. Absorption is confined mainly to cloud tops, which would be rising rapidly in midafternoon.

The radiation reaching the surface is

$$D_a = D_a \cdot (P_c + (1 - P_c) \cdot T_c) \quad (\text{direct}) \quad (\text{A.8})$$

$$F_a = F_a \cdot (P_c + (1 - P_c) \cdot T_c) \quad (\text{diffuse}) \quad (\text{A.9})$$

T_c is the cloud transmissivity and is set equal to 0.15. P_c is the CFLOS probability (table 6, in Section 5).

To account for multiple reflections between the surface and the clouds above, upward reflected radiation is defined as

$$D_{au} = D_{au} \cdot A_s \cdot N \quad (\text{direct}) \quad (\text{A.10})$$

$$F_{au} = F_{au} \cdot A_s \cdot N \quad (\text{diffuse}) \quad (\text{A.11})$$

A_s is the surface albedo and N is the normalizing factor (table 1, in Section 1). The radiation finally reaching the ground is

$$R_{dg1} = D_a + (1 - P_c) D_{au} \quad (\text{direct}) \quad (\text{A.12})$$

$$R_{fg1} = F_a + (1 - P_c) F_{au} \quad (\text{diffuse}) \quad (\text{A.13})$$

The second term is included in (A.12) and (A.13) to account for the radiation reflected from clouds on the periphery of the grid square onto the grid square itself. This is an effective way to model the minimum cloud cover reflection and scattering phenomenon discussed by Kaiser and Hill (1976). As the normalized surface albedo will ultimately be applied to these values of D_a and F_a , the multiple reflection process is believed to be adequately represented.

That spectral energy subjected to water vapor absorption is defined by S_i for $i = 4, 6, 8, 10, 12, 14, 15, 16, 17, 18, 19, 20, 23, 24$, and 25 (table 4, in section 5). For convenience, the direct radiation is defined by $D_b = D_{bi}$ ($i = 4, 6, 8, 10, 12, 14, 15, 16, 17, 18, 19, 20, 23, 24$, and 25) where b denotes this spectral energy category. Similarly the diffuse radiation is $F_b = F_{bi}$ ($i = 4, 6, 8, 10, 12, 14, 15, 16, 17, 18, 19, 20, 23, 24$, and 25).

For these spectral numbers, a considerably more complicated procedure is required (Lacis and Hansen, 1974) because spectral energy is affected by water vapor absorption, and a simple transfer process is precluded. Both the clear sky and cloudy sky transfer processes are treated as prescribed by Lacis and Hansen (1974). The partitioning of the spectral energy into cloud-free and cloudy portions is again based upon table 6. That is, the cloud treatment is invoked only for that fraction $(1 - P_c)$ of radiation impinging on clouds.

At the uppermost level, here prescribed as 100 mb, the water vapor path length from infinity to this level is arbitrarily specified as $10^{-5} \text{ gm cm}^{-2}$. The effective water vapor path length from the top of a clear sky layer to the bottom of this layer is (Lacis and Hansen, 1974)

$$Y_t = \frac{M}{g} \int_0^{P_t} q \left(\frac{P}{P_0} \right)^n \left(\frac{T_0}{T} \right)^{1/2} dP \quad (\text{A.14})$$

where M is the magnification factor,

$$M = \frac{35}{(1224 \mu_0^2 + 1)^{1/2}} \quad (\text{direct}) \quad (\text{A.15})$$

$$M = 5/3 \quad (\text{diffuse}) \quad (\text{A.16})$$

q is the specific humidity, $P_0 = 1013$ mb, $N = 1$, and $T_0 = 273$ K. Y_i is calculated for each layer and the absorptivity calculated separately for direct and diffuse radiation. The absorptivity for each layer is

$$A(Y_i) = \frac{2.9}{(1 + 141.5 Y_i)^{0.635} + 5.925 Y_i} \quad (\text{A.17})$$

For any given layer, this quantity is calculated for the total path length from the top of the atmosphere to the top of that layer. The direct and diffuse radiation absorbed in each cloud-free atmospheric layer is

$$D_{cfl} = D_i(A(Y_i) + 1) - A(Y_i), \quad (\text{A.18})$$

and

$$F_{cfl} = F_i(A(Y_i) + 1) - A(Y_i). \quad (\text{A.19})$$

D_i is the total spectral direct energy and F_i is the equivalent total spectral diffuse energy remaining after ozone, cirrus, and atmospheric scattering. $D_i + F_i$ is the total energy impinging on the water vapor atmosphere at level 1.

If low clouds are not present, D_{cfl} and F_{cfl} are calculated for each layer down to the surface. The radiation reaching the ground is

$$R_{dg2} = D_b - \sum_1^{\ell} D_{cfl} \quad (\text{direct}) \quad (\text{A.20})$$

and

$$R_{fg2} = F_b - \sum_1^{\ell} F_{cfl} \quad (\text{diffuse}) \quad (\text{A.21})$$

Summation from level 1 to level ℓ is conducted from the level at which D_i and F_i are defined down to the last layer adjoining the surface (layer ℓ). D_b is the total spectral direct radiation contained in the water vapor bands which reaches the top of the water vapor atmosphere. F_b is the equivalent for diffuse radiation. The quantities on the right hand side of (A.20) and (A.21) represent the total direct and diffuse radiation, respectively, which are absorbed by the water vapor atmosphere. The absorption by water vapor of the surface-related radiation is neglected for clear skies or the clear sky portion P_c .

If low clouds are present, the procedure above is followed down to the prescribed low

cloud-top level. At that level, the radiation which will be affected by clouds in the amount of $(1 - P_c)$ is

$$D_c = (1 - P_c) \cdot (D_b - \sum_1^{\ell_c} D_{cfl}) \quad (\text{direct}) \quad (\text{A.22})$$

and

$$F_c = (1 - P_c) \cdot (F_b - \sum_1^{\ell_c} F_{cfl}) \quad (\text{diffuse}) \quad (\text{A.23})$$

ℓ_c refers to the layer just above the layer containing prescribed low cloud tops. The procedure for transfer through open cloud spaces is the same for clear skies, except that the factor P_c is used in (A.22) and A.23).

The transfer through the water vapor atmosphere in clouds, for these spectral energy values affected by water vapor, is based upon the multiple scattering treatment of Lacis and Hansen (1974). The present procedure deviates from that prescribed by these authors by treating partly cloudy atmospheres $(1 - P_c)$ as well as those which are completely cloudy.

The total optical thickness of a cloud layer is

$$\tau_{in} = \tau_i^c + k_n \cdot M \cdot Y_i \quad (n = 8 \text{ for each layer}) \quad (\text{A.24})$$

$$\tau_i^c = \frac{(P_b - P_t) \cdot 8}{\Delta P} \quad (\text{optical thickness of cloud})$$

P_b , P_t are pressures at the bottom and top of the layer, respectively. ΔP is 100 mb. k_n is the absorption coefficient. The eight spectrally dependent values are given in table 1 (Lacis and Hansen, 1974).

$$M = 5/3 \quad (\text{magnification factor for diffuse radiation}) \quad (\text{A.25})$$

Y_i is the layer optical thickness due to water vapor (A.14).

The single scattering albedo, required in the following multiple scattering treatment, is

$$\tilde{\omega}_{in} = \frac{\tau_i^c}{\tau_{in}} \cdot (n = 8 \text{ for each layer}) \quad (\text{A.26})$$

The reflection and transmission functions are calculated for each layer containing clouds.

$$R_i = \frac{(u + 1)(u - 1)(e^t - e^{-t})}{(u + 1)^2 e^t - (u - 1)^2 e^{-t}} \quad (\text{reflection function})$$

$$T_i = \frac{4u}{(u + 1)^2 e^t - (u - 1)^2 e^{-t}} \quad (\text{transmission function}) \quad (\text{A.27})$$

$$u = \left\{ \frac{1 - g \cdot \tilde{\omega}_{\ell,n}}{1 - \tilde{\omega}_{\ell,n}} \right\}^{1/2}$$

$$t = [3(1 - \tilde{\omega}_{\ell,n})(1 - g \cdot \tilde{\omega}_{\ell,n})]^{1/2} \cdot \tau_c^\ell$$

(asymmetry factor for clouds)

$$g = 0.85$$

The basic rationale and procedures for the multiple scattering treatment known as the doubling and adding method are given in Lacis and Hansen (1974). The reflection and transmission functions for a composite layer are

$$R_{1,2} = R_1 + T_1 \cdot R_2 \cdot T_1^* / (1 - R_1^* R_2) \quad (\text{A.28})$$

and

$$T_{1,2} = T_1 \cdot T_2 / (1 - R^* \cdot R_2) \quad (\text{A.29})$$

where R_2 and T_2 refer to the bottom layer reflection and transmission functions. The composite layer reflection and transmission functions, $R_{1,2}$ and $T_{1,2}$, are for the composite of all layers above. That is, as each layer below is "added," R_1 becomes $R_{1,2}$ from the last computation. Similarly, T_1 becomes $T_{1,2}$. T_1^* is equal to T_1 and R_1^* is equal to R_1 in a cloudy atmosphere.

A composite layer reflection function is calculated for illumination from below. This is

$$R_{1,2}^* = R_2^* - T_2^* \cdot R_1^* \cdot T_1 / (1 - R_1^* \cdot R_2) \quad (\text{A.30})$$

The initially incident radiation going up is that reflected by the surface. The functions are calculated in reverse order starting from the surface and "added" as each layer is encountered in the vertical. At each level, at the boundary between the composite layers, eight upward and eight downward flux functions are calculated for each computation of (A.28), (A.29), and (A.30).

These are

$$U_\ell = T_{1,\ell} \cdot R_{\ell+1,L+1} / (1 - R_{1,\ell}^* R_{\ell+1,L+1}) \quad (\text{A.31})$$

and

$$D_\ell = T_{1,\ell} / (1 - R_{1,\ell}^* \cdot R_{\ell+1,L+1}) \quad (\text{A.32})$$

$R_{1,\ell}^*$ is the composite layer reflection function calculated down to a particular level, while $R_{\ell+1,L+1}$ is the composite layer reflection function calculated up to this level. $T_{1,\ell}$ is the composite layer function for all layers going down to this level.

The absorptivity for each of the $n(n = 8)$ probabilities $P(k_n)$ in table 1 of Lacis and Hansen (1974) is calculated for composite layers

$$A_{1,\ell}(n) = P(k_n)[1 - R_{1,L+1}(n) + U_\ell(n) - D_\ell(n)]. \quad (\text{A.33})$$

The absorptivity for an individual layer is

$$A_2(n) = A_{1,\ell}(n) - A_1(n) \quad (\text{A.34})$$

where subscript 2 refers to the layer in question and subscript 1 refers to the composite layer next above.

Summation over each of the eight values of $A_2(n)$ for each layer is then carried out:

$$A_\ell = \sum_{n=1}^8 A_\ell(n) \quad (\text{A.35})$$

The radiation absorbed owing to water vapor in each layer is then

$$R_\ell = (D_{c\ell} + F_{c\ell}) + A_\ell(D_c + F_c) \quad (\text{A.36})$$

The incremental temperature change for each layer containing a model level is

$$\Delta\theta = \frac{g}{C_p} \left(\frac{P_0}{P} \right)^* \frac{R_\ell}{\Delta P} \quad (\text{A.37})$$

The radiation reaching the surface is

$$R_{dg3} = D_c - \sum_\ell A_\ell D_c \quad (\text{A.38})$$

and

$$R_{fg3} = F_c - \sum_\ell A_\ell F_c \quad (\text{A.39})$$

Finally, all direct and diffuse fluxes in all wavelengths which reach the surface are summed.

$$R_{gT} = R_{dg1} + R_{fg1} + R_{dg2} + R_{fg2} + R_{dg3} + R_{fg3} \quad (\text{A.40})$$

At this point, the attenuation from dust, oxygen, and carbon dioxide is taken into account. R_{gT} is subjected to a bulk depletion from these gases. Although the depletion takes place at higher levels, the application of the depletion formulations at this point still provides a good final correction to the incoming solar radiation. The formulations are those of Sasamori et al. (1972) and are applied regardless of the cloud cover amount.

$$\text{Dust} = 1 - 0.97^a + 1 - 0.975^b \quad (\text{dust depletion}) \quad (\text{A.41})$$

$$a = \frac{\text{PSF}}{1013.2 \mu_0}$$

PSF is surface pressure

b = total atmospheric water vapor path length

$$\text{GAS1} = 2.35 \cdot 0.001 [u(\text{CO}_2) \cdot M + 0.0129]^c - 7.5 \cdot 0.0001 \quad (\text{carbon dioxide depletion}) \quad (\text{A.42})$$

$$c = 0.26$$

$u(\text{CO}_2)$ is total atmospheric carbon dioxide path length.

$$M = \frac{35}{(1224 \mu_0^2 + 1)^{1/2}} \quad (\text{magnification factor})$$

$$\text{GAS2} = 7.5 \cdot 0.001 \left(\frac{\text{PSE}}{\mu_0 \cdot 1013.2} \right)^d \quad (\text{oxygen depletion}) \quad (\text{A.43})$$

$$d = 0.875$$

Thus, the following radiation reaches the ground:

$$R_{gT} = R_{gT} - (\text{GAS 1} + \text{GAS 2} + \text{DUST}) \cdot R_{gT}.$$

Finally, the total radiation is subjected to reflection from the ground. The amount of incoming solar energy that enters the surface layer and heats it is

$$R_{gT} = R_{gT} (1 - A_s N). \quad (\text{A.44})$$

$A_s N$ is the normalized albedo of the ground. R_{gT} is the solar component of energy in the heat balance equation used in the surface heating subroutine.

A.4. LONG-WAVE RADIATION TRANSFER

The optical path length for carbon dioxide and water vapor is

$$u = \frac{1}{g} \int_{P_{\ell+1}}^{P_{\ell}} q \left(\frac{P}{P_0} \right) dP. \quad (\text{A.45})$$

g is gravity, q is the mixing ratio of the absorbing gas, P_0 is the standard pressure (1013.5 mb), and P_{ℓ} and $P_{\ell+1}$ are the pressures at the top and bottom of the air column, respectively.

For carbon dioxide, the optical path length across a layer extending from P_{ℓ} to $P_{\ell+1}$ is

$$du \text{ (cm STP)} = (P_{\ell}^2 - P_{\ell+1}^2) \cdot (1.178 \times 10^{-4}) \quad (\text{A.46})$$

This derives from

$$u(\text{cm STP}) = \frac{N}{\eta_0 m} [u(g \text{ cm}^{-2})],$$

$$\begin{aligned} N &= 6.023\text{E}23 \text{ mole}^{-1} && (\text{Avogadro's number}), \\ \eta_0 &= 2.687\text{E}19 \text{ cm}^{-3} \text{ at STP} && (\text{Loschmidt's number}), \\ m &= 44 \text{ g mole}^{-1} && (\text{molecular weight of CO}_2). \end{aligned}$$

Thus,

$$u(\text{cm STP}) = 5.094 \times 10^2 \text{ cm}^3 \text{ g}^{-1} \cdot [u(g \text{ cm}^{-2})]. \quad (\text{A.47})$$

With

$$Q_{\text{CO}_2} = 4.6 \times 10^{-4} \frac{g_{\text{CO}_2}}{g_{\text{AIR}}} \quad (\text{percent by mass})$$

in (A.45), (A.46) can be obtained.

For water vapor, the optical path length across a layer is

$$\begin{aligned} du(g) &= (Q_{\text{H}_2\text{O}(t)} + Q_{\text{H}_2\text{O}(t+1)}) \\ &\quad \cdot (P_{\ell}^2 - P_{\ell+1}^2) / 3.97 \times 10^6 \end{aligned} \quad (\text{A.48})$$

This follows directly from (A.39).

The water vapor and carbon dioxide absorptivities and transmissivities of Sasamori (1968) as employed in the G. F. Watson (1971) program are used without alteration here.

The water vapor absorptivity which holds for the range of temperature from 30°C to -50°C is

$$\begin{aligned} \bar{A}_0 &= 0.846 (u_1 + 3.59 \times 10^{-5})^{0.243} - 6.90 \times 10^{-2} \\ &\quad \text{for } u_1 \equiv u(\text{H}_2\text{O}) \leq 0.01 \text{ g} \end{aligned} \quad (\text{A.49})$$

and

$$\begin{aligned} \bar{A}_0 &= 0.240 \log_{10} (u_1 + 0.010) + 0.622 \\ &\quad \text{for } 0.01 \leq u_1 < 5 \text{ g} \end{aligned} \quad (\text{A.50})$$

The water vapor absorptivity which is temperature-dependent is

$$\bar{A}(u, T) = 8.34 T^{(0.353 \log_{10} u_1 - 0.44)} \times u_1^{(-0.03455 \log_{10} u_1 - 0.705)}. \quad (\text{A.51})$$

The transmissivity of water vapor near 15 μm is

$$\tau(\text{H}_2\text{O}) = 1.33 - 0.832(u_1 + 0.0286)^{0.260}. \quad (\text{A.52})$$

Carbon dioxide absorptivity, which holds for the range of temperature from 30°C to -50°C, is

$$\begin{aligned} \bar{A}_0 &= 0.0676 (u_2 + 0.01022)^{0.421} - 0.00982 \\ &\quad \text{for } u_2 = u(\text{CO}_2) \leq 1 \text{ cm}, \end{aligned} \quad (\text{A.53})$$

and

$$\bar{A}_0 = 0.0546 \log_{10} u_2 + 0.0581 \quad \text{for } u_2 > 1 \text{ cm.} \quad (\text{A.54})$$

Carbon dioxide absorptivity based upon a temperature equal to -60°C is

$$\bar{A} = 0.0825 u_2^{0.456} \quad \text{for } u_2 \leq 0.5 \text{ cm} \quad (\text{A.55})$$

and

$$\bar{A} = 0.0461 \log_{10} u_2 + 0.074 \quad \text{for } u_2 > 0.5 \text{ cm} \quad (\text{A.56})$$

Ozone was not considered in the infrared transmission calculations. The total path length in these expressions refers to the total optical depth from a radiating level (surface, cloud base, cloud top, etc.) to the reference level where upward and downward fluxes are evaluated.

The absorptivities for carbon dioxide at each level are corrected by multiplication with the water vapor transmissivities for that level. This is an empirical method for correcting overlapping absorption of the water vapor and carbon dioxide bands near $15 \mu\text{m}$. The effect is similar to that employed by Burch et al. (1956) in correcting overlap near $2.7 \mu\text{m}$. That is, in consideration of

$$\bar{A}_{\text{CO}_2} = \bar{A}_{\text{CO}_2} \cdot \tau_{\text{H}_2\text{O}}$$

it can be seen that where $\tau_{\text{H}_2\text{O}}$ is large, as would be true in the upper atmosphere, \bar{A}_{CO_2} dominates. Where $\tau_{\text{H}_2\text{O}}$ is small, as near the surface, $A_{\text{H}_2\text{O}}$ would dominate and \bar{A}_{CO_2} would be minimal.

The infrared transfer routine is designed to calculate fluxes for clear skies or variable cloud conditions in two cloud layers. The cloud layers consist of low clouds (previously defined) and cirriform clouds. For downward-directed radiation in clear skies, the carbon dioxide and water vapor fluxes received at the surface or any higher level (subscript TL) are

$$F\downarrow_{\text{CO}_2} = -\sigma \int_{F_L}^{F_{TL}} \bar{A}_{\text{CO}_2}(u) dF - \sigma T_{TL}^4 \cdot \bar{A}_{\text{CO}_2} \cdot \tau_{\text{H}_2\text{O}(TL)} \quad (\text{A.57})$$

and

$$F\downarrow_{\text{H}_2\text{O}} = -\sigma \int_{F_L}^{F_{TL}} \bar{A}_{\text{H}_2\text{O}}(u) dF - \sigma T_{TL}^4 \cdot \bar{A}_{\text{H}_2\text{O}} \quad (\text{A.58})$$

TL refers to the highest model level, 100 mb.

$$S_{\text{IR}} = \sum_{i=23}^{25} (D_{ai} + F_{ai}) \cdot (1 - \bar{A}_{\text{H}_2\text{O}}) \quad (\text{A.59})$$

This contribution is that very small amount of solar radiation which lies in the far infrared from $12.5 \mu\text{m}$ to $1000 \mu\text{m}$. The factor $(1 - \bar{A}_{\text{H}_2\text{O}})$ is a gross correction which is primarily intended to represent total atmospheric absorption of energy in these wavelengths before its arrival at the surface. Although available measurements indicate the effective black-body temperature of the sun decreases as wavelength increases (Drummond and Thekaekara, 1973), it is conceivable that orbiting satellites will show otherwise in the future, particularly for quiet sun periods. Thus, the capability of accounting for this spectral region is retained.

$$\sigma = 1.3533 \times 10^{-12} \text{ cal cm}^{-2} \text{ sec}^{-1} \text{ } ^\circ\text{K}^{-4} \quad (\text{Stefan-Boltzmann constant})$$

$F = \sigma T^4 \text{ cal cm}^{-2} \text{ sec}^{-1}$; the black-body flux emitted at the temperature of the level in question.

The integrations are performed by means of a modified Simpson's routine (G. F. Watson, 1971). The accuracy of the routine is increased by the addition of levels where warranted. The total downward flux for the clear sky case is then

$$F\downarrow_T = F\downarrow_{\text{H}_2\text{O}} + F\downarrow_{\text{CO}_2} + S_{\text{IR}} \quad (\text{A.60})$$

For upward-directed radiation in clear skies, the fluxes at any level are

$$F\uparrow_{\text{CO}_2} = -\sigma \int_{F_{sfc}}^{F_L} A_{\text{CO}_2}(u) dF \quad (\text{A.61})$$

and

$$F\uparrow_{\text{H}_2\text{O}} = -\sigma \int_{F_{sfc}}^{F_L} A_{\text{H}_2\text{O}}(u) dF \quad (\text{A.62})$$

The total upward flux for the clear sky case is then:

$$F\uparrow_T = \sigma T_{sfc}^4 + F\uparrow_{\text{H}_2\text{O}} + F\uparrow_{\text{CO}_2} \quad (\text{A.63})$$

To account for downward-directed radiation when cirriform clouds are present, certain modifications were made to the original program. These modifications allow cirriform clouds to have variable emissivities. The original version treated cirrus as black in the infrared and assigned it a 5/10 cloud cover at the cirrus level. Since infrared radiation measurements at the bases and tops of

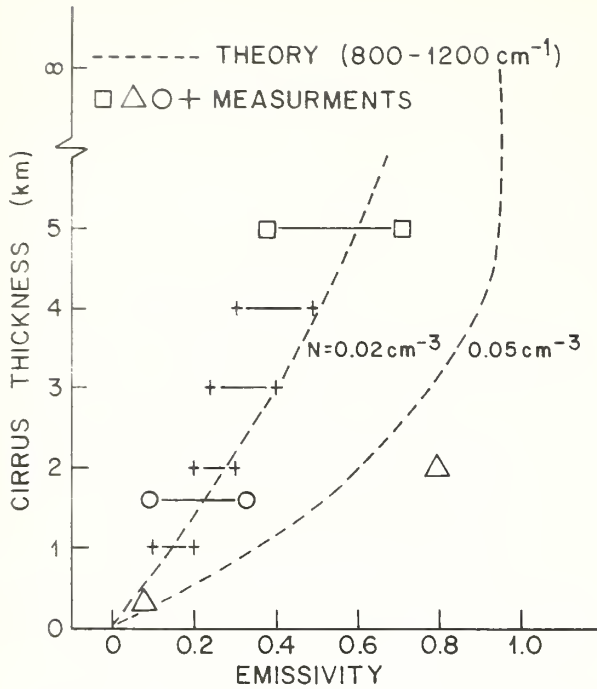


Figure A-1. Cirrus thickness (km) and emissivity (from Liou, 1974, Fig. 6, p. 529, with permission of the author and the American Meteorological Society).

cirrus layers were not made, effective emissivities could not be determined in the manner described by Fleming and Cox (1974). Therefore, an alternative procedure was employed.

The assumption is made that the number density of cirrus particles is 0.05 cm^{-3} (Liou, 1974). This assumed average number density does conflict with the average number density of 0.5 cm^{-3} used to define optical properties for solar short wave transfer (Liou, 1973). The differences arise from the number densities obtained from two different experimental data sets. As Platt (1975) has shown, cirrus emissivity can vary widely in time and space. It is safe to assume that other optical properties can also vary in the same manner. Although figure A-1 (Liou, 1974) shows a certain regularity in the cirrus thickness/emissivity relationships, an element of uncertainty exists concerning the true optical properties of cirrus in a given numerical experiment designed to simulate a case study day. The calibration procedures used to define these properties over the averaging domain used in case studies are described in Appendix B.

The cirrus geometric thickness is determined from the densitometer (Appendix B) and the emissivity determined from figure A-1 (Liou, 1974).

To illustrate the procedure for calculating downward-directed flux when clouds are present,

the most complicated situation, that of two cloud layers, is presented. The fluxes (S_{IR} not considered) arriving at the top of the cirrus layer are

$$F\downarrow_{CO_2} = -\sigma \int_{F_{CTL}}^{F_{TL}} \bar{A}_{CO_2}(u) dF - \sigma T_{TL}^4 \cdot \bar{A}_{CO_2} \cdot \tau_{H_2O_{TL}} \quad (\text{A.64})$$

and

$$F\downarrow_{H_2O} = -\sigma \int_{F_{CTL}}^{F_{TL}} \bar{A}_{H_2O}(u) dF - \sigma T_{TL}^4 \cdot \bar{A}_{H_2O}. \quad (\text{A.65})$$

The subscript TL refers to 100-mb level; CTL to cirrus top level. The sum of these components would be the total flux arriving at the top of the cirrus layer.

The downward fluxes arriving at an intermediate level between the bases of high clouds and the tops of low clouds would be

$$F\downarrow_{CO_2} = -\sigma \int_{F_L}^{F_{TL}} \bar{A}_{CO_2}(u) dF + (1-\epsilon) \times \text{Eq. (A.64)} \quad (\text{A.66})$$

$$F\downarrow_{H_2O} = -\sigma \int_{F_L}^{F_{TL}} \bar{A}_{H_2O}(u) dF + (1-\epsilon) \times \text{Eq. (A.65)} \quad (\text{A.67})$$

and

$$F\downarrow_{CL} = \epsilon \cdot \sigma \cdot \bar{T}_{CL}^4. \quad (\text{A.68})$$

ϵ is the emissivity of the cirrus determined from satellite imagery or simply prescribed.

\bar{T}_{CL} is the mean temperature of the cirrus layer.

$F\downarrow_{CL}$ is flux originating from ice particles in the cirrus cloud layer.

The emissivities are approximations based upon the densitometer analysis of satellite images of cirrus layers. Therefore, the emissivities will differ from the true effective emissivities (Fleming and Cox, 1974), which also include the effects of emission by gases in the cirrus layer. The gaseous absorption and reemission processes in the layer are considered to be independent of the cirrus particles, while the cirrus particles radiate at the mean temperature of the layer. The modifications to the original model, in which it is assumed that cirrus is black in the infrared and characterized by 5/10 cloud cover, are consequential only for cirrus layers below 300 mb. As Fleming and Cox (1974) point out, in a tropical atmosphere the downward flux at the surface is relatively insensitive to the emissivity of a high cloud layer.

The total downward flux at the intermediate level (T_1) is then

$$F\downarrow_{T_1} = F\downarrow_{CO_2} + F\downarrow_{H_2O} + F\downarrow_{CL}. \quad (\text{A.69})$$

At the base of the low clouds,

$$F\downarrow_{\text{CO}_2} = 0,$$

$$F\downarrow_{\text{H}_2\text{O}} = 0,$$

and

$$F\downarrow_{\text{BLC}} = \sigma T_{\text{BLC}}^4.$$

where the subscript *BLC* refers to the low cloud base. Thus, the total downward flux at low cloud base level (*T2*) is

$$F\downarrow_{T2} = N \cdot F\downarrow_{\text{BLC}} + (1 - N) \cdot F\downarrow_{T1} \quad (\text{A.70})$$

where *N* is the low cloud cover in tenths. *F_{T1}* is calculated for this level.

The downward fluxes that originate at low cloud base and arrive at levels (*T3*) between low cloud base and the surface are

$$F\downarrow_{\text{CO}_2} = -\sigma \int_{F_L}^{F_{\text{BLC}}} \bar{A}_{\text{CO}_2}(u) dF, \quad (\text{A.71})$$

$$F\downarrow_{\text{H}_2\text{O}} = -\sigma \int_{F_L}^{F_{\text{BLC}}} \bar{A}_{\text{H}_2\text{O}}(u) dF, \quad (\text{A.72})$$

and

$$F\downarrow_{T3} = \sigma T_{\text{BLC}}^4 + F\downarrow_{\text{CO}_2} + F\downarrow_{\text{H}_2\text{O}}. \quad (\text{A.73})$$

The total (*T*) downward flux from all levels above the surface or a level (*1*) between the surface and low cloud base is

$$F\downarrow_T = N \cdot F\downarrow_{T3} + (1 - N) \cdot F\downarrow_1 \quad (\text{A.74})$$

where *F₁* is calculated at this lower level.

Upward flux originating at the surface is simply

$$F\uparrow_G = \sigma T_G^4 \quad (\text{A.75})$$

where subscript *G* refers to the ground.

For levels intermediate between the surface and low cloud base,

$$F\uparrow_{\text{CO}_2} = -\sigma \int_{F_G}^{F_L} \bar{A}_{\text{CO}_2}(u) dF, \quad (\text{A.76})$$

$$F\uparrow_{\text{H}_2\text{O}} = -\sigma \int_{F_G}^{F_L} \bar{A}_{\text{H}_2\text{O}}(u) dF,$$

and

$$F\uparrow_{T1} = \sigma T_G^4 + F\uparrow_{\text{CO}_2} + F\uparrow_{\text{H}_2\text{O}}. \quad (\text{A.77})$$

At the tops of low clouds

$$F\uparrow_{\text{CO}_2} = 0,$$

$$F\uparrow_{\text{H}_2\text{O}} = 0,$$

and

$$F\uparrow_{T2} = \sigma T_{\text{TLC}}^4.$$

where the subscript *TLC* refers to the low cloud top. Thus, the total upward flux at low cloud top level is

$$F\uparrow_{CT} = N \cdot F\uparrow_{T2} + (1 - N) \cdot F\uparrow_{T1} \quad (\text{A.78})$$

where *F_{T1}* is calculated at this level.

For levels between low cloud tops and cirrus base level, the upward fluxes which originate at low cloud tops are

$$F\uparrow_{\text{CO}_2} = -\sigma \int_{F_{\text{TLC}}}^{F_L} \bar{A}_{\text{CO}_2}(u) dF, \quad (\text{A.79})$$

$$F\uparrow_{\text{H}_2\text{O}} = -\sigma \int_{F_{\text{TLC}}}^{F_L} \bar{A}_{\text{H}_2\text{O}}(u) dF, \quad (\text{A.80})$$

and

$$F\uparrow_3 = \sigma T_{\text{TLC}}^4 + F\uparrow_{\text{CO}_2} + F\uparrow_{\text{H}_2\text{O}}. \quad (\text{A.81})$$

The total upward flux for these levels is then

$$F\uparrow_T = N \cdot F\uparrow_3 + (1 - n) \cdot F\uparrow_1. \quad (\text{A.82})$$

F₁ is evaluated for this level.

The upward fluxes above the cirrus top level were not evaluated since cooling rate requirements terminate at the height of the material surface in the vicinity of 500 mb.

The net flux at each reference level is

$$F_N = F\uparrow_T - F\downarrow_T. \quad (\text{A.83})$$

Cooling rates are calculated for Pielke model levels lying between reference levels. The cooling rate (potential temperature) at each of the Pielke model levels is

$$\theta' = 4.083 \frac{(F_{N_{\text{TRL}}} - F_{N_{\text{BRL}}})}{(P_{\text{TRL}} - P_{\text{BRL}})} (^\circ\text{C sec}^{-1}). \quad (\text{A.84})$$

The subscripts *TRL* and *BRL* refer to the top reference level and bottom reference level, respectively. The value of *F_{1,fc}* at the air-ground interface is the atmospheric infrared flux contribution to the surface heat balance equation used in the model.

Appendix B

DENSITOMETER TECHNIQUES FOR DERIVATION OF CLOUD PROPERTIES

B.1 INTRODUCTION

High resolution ($\frac{1}{2}$ -1 nmi) visible and medium resolution (4 nmi) infrared positive transparency images from the Synchronous Meteorological Satellite (SMS-1) were used to determine cloud type, height, geometric and optical thickness, emissivity, and areal coverage. These images were analyzed by a color densitometer (Griffith et al., 1976) and an automatic photographic analyzer. The two instruments were electronically linked to provide a unique analysis capability. The combined system enables instantaneous cloud areal coverage measurements to be made.

B.2 COLOR DENSITOMETER

The densitometer is an I²S (International Imaging System) Digicol system. The instrument, owned by the Miami-based NOAA community, converts positive or negative transparency or paper images into a false color display. The color depends upon the gray shades of the image. The advantage of the color-coded information lies in the enhanced ability of the observer to interpret the desired information. Quantitative density, transmissivity, and color enhancements are derived from the instrumentation.

Figure B-1 shows the light table, Polaroid camera, TV monitor, density monitor, density control unit (DCU), and digital image processor (DIP). The small switch box is the Quantitative Metallurgical System (QMS) interface unit. The QMS is described below, in Section B.3. The satellite images are placed on the light table, the camera is focused, and the cloud images displayed in color hues and increments chosen by the operator. Figure B-2 is a representative densitometer monitor image of a satellite scene of Florida and prevailing cloud cover. The optical densities or transmissivities of these gray shades (which are represented in color on the TV monitor) are determined with techniques given in Griffith et al. (1976).

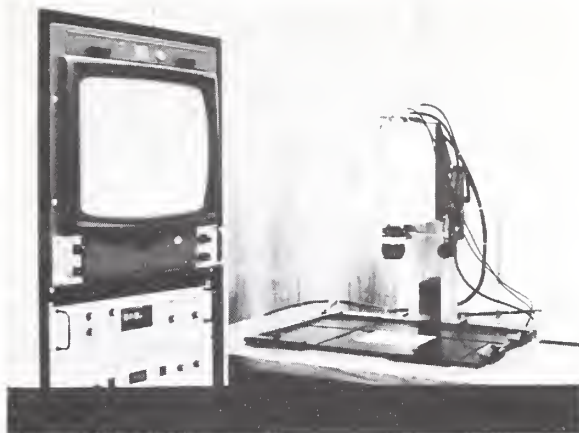


Figure B-1. Miami-based NOAA I²S color densitometer showing light table, Polaroid camera, TV monitor, density control unit, digital image processor, and Quantitative Metallurgical System interface unit.

B.3 QUANTITATIVE METALLURGICAL SYSTEM (QMS)

The QMS is a Bausch and Lomb device whose principal function at the NOAA facility in Miami is to aid in evaluation of ice particle and water droplet size and density spectra. It was designed primarily to assist in evaluation of metallic particulate size and density spectra (e.g., percentage area of lead and size distribution in leaded brass). The QMS was electronically mated to the I²S. Thus, appropriate switches on the I²S DIP. The lever on the also be displayed on the QMS display monitor. Figure B-3 shows the processing and control unit, the display section, and the control box. With the control box, a variable area is selected (e.g., one

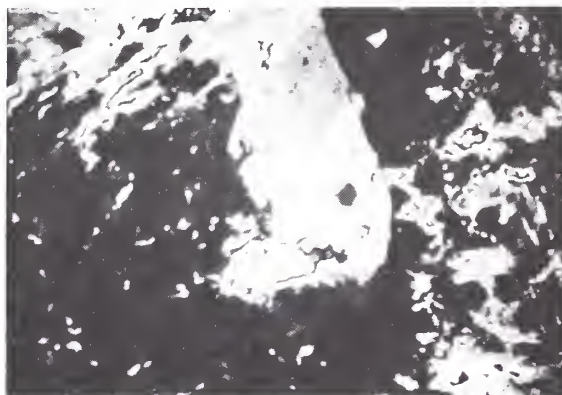


Figure B-2. Color densitometer monitor image of a satellite picture.

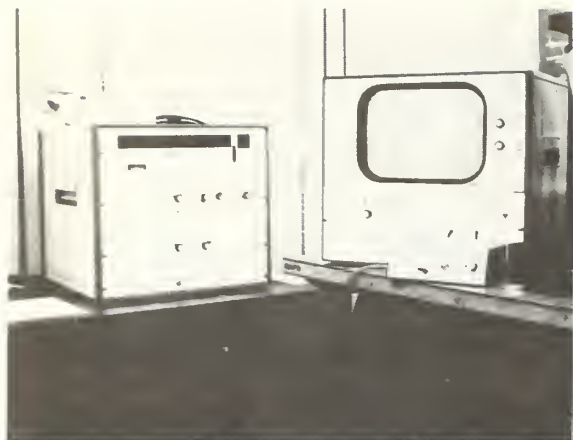


Figure B-3. Miami-based NOAA Quantitative Metallurgical System automatic analyzer.

grid square). The horizontal and vertical axes of this rectangular area are adjusted at will with the control box joy stick. A level is thrown and the number of areal units covered by this area are instantly displayed on the QMS display monitor. With the switch of the QMS interface unit in the "on" position, the densitometer images are displayed on the QMS monitor. The colors corresponding to the cloud forms of interest within the chosen area are retained while other cloud form images are eliminated by the throwing of appropriate switches on the I²S DIP. The lever on the QMS control box is thrown again and the number of area units covered by the chosen cloud form image within the chosen area is instantly displayed on the QMS monitor. The ratio of cloud cover to the chosen area provided the percentage of cloud cover required for that grid square or other chosen area.

B.4 LOW CLOUDS

Low clouds were in most instances easily identified on SMS-1 visible imagery. The densitometer colors and densities corresponding to these clouds were identified and their areal coverage determined in the manner discussed in Section 3. In lieu of measuring areal coverage over one grid square, cloud cover was determined for overlapping areas covering six grid squares. That is, the basic 66 × 66 km area on the QMS was centered over a region equal to one model grid square (11 × 11 km) and cloud cover was determined. The basic area was then centered over the next adjoining model grid square and the process repeated. In this way, the effect of low clouds on the incoming and reflected radiation under all solar zenith angles was adequately represented.

Low cloud-top temperatures were determined from the mean temperature corresponding to the colors displayed on the I²S from full disk SMS-1 4-nmi resolution infrared imagery. Low cloud heights and pressures were obtained from the heights and pressures corresponding to the temperatures on the nearest rawinsonde sounding.

B.5 HIGH CLOUDS

High clouds were, in most instances, easily identified on SMS-1 visible imagery. Occasional comparisons between SMS-1 infrared imagery and surface observations were required to firmly establish cloud type. Anvil cirrus directly over a cumulonimbus, here classified as low cloud, was considered to be part of the low cloud. It was found that seven discrete hues corresponding to cirriform clouds could be identified with the color densitometer. It was suspected that optical thicknesses (used in cirrus transfer for solar radiation) would vary not only with geometric thickness, but also with variable number densities. It was decided that increases in number density over the value assumed by Liou (1973) could be treated as increases in geometric thickness. The maximum geometric thickness was chosen on the basis of the thickness of the moist layer at cirrus level. The appropriate hue corresponding to the brightest (excluding anvil cirrus over low cloud) cirrus cloud was identified and associated with this thickness. The remaining six hues were linearly allocated across the range from zero geometric thickness to that value derived from the sounding. From the geometric thicknesses determined from the imagery, optical thicknesses were derived (Section 5.5). Cirrus cloud emissivities used in long wave radiation transfer (Section 5.6) are determined from the derived geometric thicknesses.

B.6 CLOUD DATA FOR MODEL

The procedures discussed in Sections 4 and 5 were conducted for case study days on visible and infrared images on the half hour from 0539 EST to 1800 EST. This necessitated evaluation of cloud properties at 18 grid squares every half hour for a total of 936 separate grid-square evaluations. This was time-consuming "in extremum," yet vitally necessary to demonstrate real cloud effects.

This is a unique effort and one which has not been duplicated elsewhere. These procedures must be simplified and expanded so that three-dimensional studies can be conducted without prohibitive time constraints.

Appendix C

SOIL MOISTURE HISTORY: JULY 1 TO 16, 1975

If operational numerical predictions of the South Florida sea breeze are to be conducted, the persistence of initial soil moisture profiles should be known. This appendix provides an indication that dependency upon persistence is, in general, not warranted.

Table C-1 provides the mean, maximum, and minimum values in surface soil moisture and relative humidity across the study region from July 1 to July 16, 1975. In addition, the surface relative humidity is classified into four groups to give a frequency distribution.

Figure C-1 shows three representative time histories of surface soil moisture and relative humidity. These graphically illustrate the large temporal and spatial variations in surface soil moisture and relative humidity which occurred during the period.

The soil moisture and relative humidity values were obtained using figures 53 and 54 and procedures provided in Section 6.9. Radar rainfall estimates for grid points 9 and 10 were not available for the period July 4 through July 10, 1975,

and are not included in table C-1. As grid points 24 and 25 lie in the Water Conservation Area, soil moisture and drainage processes are not applicable. Thus, data for these grid points are not given. The adjustments to soil moisture for these two grid points (p. 107) have to be considered as compensating for initial surface temperatures being prescribed too low. Note that soil moisture values greater than the saturation value (a soil water volume ≤ 1) are given in table C-1. Any value greater than the saturation value (see fig. 54) is considered as standing water which is also subjected to evaporation and drainage.

The drainage curves in figure 53 were established on the basis of one experimental curve for fine sand and adjustments based upon available water capacity. Based upon the adjustments necessary for the peat muck soils (figs. 55 and 58), it is highly probable that the actual drainage rates are somewhat higher than indicated on figure 53. Another element of uncertainty arises from the partial dependence of peat muck soil moisture on the water table level (USDA, 1960).

Despite these uncertainties, the differences in water retention capability among the sandy soils and muck soils are so large that the conclusions derived from table C-1 and figure C-1 are considered valid. Table C-1 shows the surface soil moisture-relative humidity relationship varies as the soil type in a manner similar to figure 54. For

Table C-1.
Surface soil moisture (SM) and relative humidity (RH) from July 1 to July 16, 1975

Grid point	Soil type*	Mean		Maximum		Minimum		Frequency (days) of Surface RH (%)			
		SM($\text{cm}^3\text{cm}^{-3}$)	RH(%)	SM($\text{cm}^3\text{cm}^{-3}$)	RH(%)	SM($\text{cm}^3\text{cm}^{-3}$)	RH(%)	0-25	26-50	51-75	76-100
11	2	0.1	53	0.4	100	0.0	0	7	0	0	8
12	2	0.1	49	0.8	98	0.0	0	7	1	0	7
13	3	0.3	57	2.3	100	0.0	0	6	0	0	9
14	1	0.1	53	0.6	100	0.0	0	7	0	0	8
15	2	0.6	67	4.6	100	0.0	0	5	0	0	10
16	3	0.1	57	0.4	100	0.0	0	6	0	0	9
17	3	0.1	56	0.2	96	0.0	0	6	0	0	9
18	3	0.1	62	0.2	98	0.0	0	5	0	0	10
19	4	4.0	100	5.2	100	2.7	100	0	0	0	15
20	4	1.0	71	2.7	100	0.0	0	4	0	1	10
21	4	1.6	96	2.7	100	0.3	52	0	0	1	14
22	4	5.8	100	6.5	100	4.6	100	0	0	0	15
23	4	4.6	100	5.6	100	3.9	100	0	0	0	15
24	water and grass										
25	water and grass										
26	1	0.1	85	0.1	100	0.0	0	2	0	0	13
27	1	0.8	64	4.9	100	0.0	0	5	0	1	9

*Soil types:

1: Leon-Immokalee

2: Adamsville-Pompano

3: Manatee-Felda

4: Everglades-peat muck

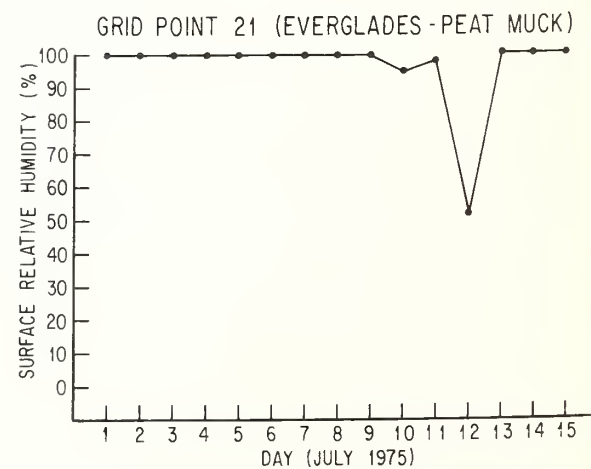
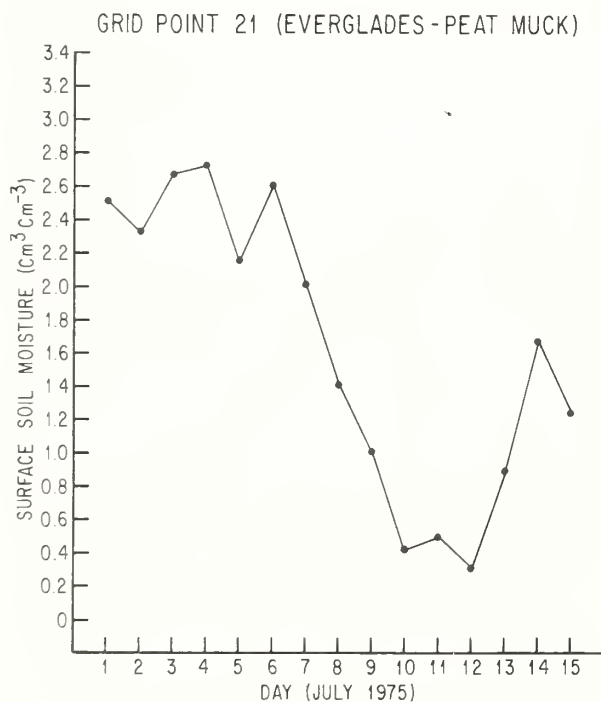
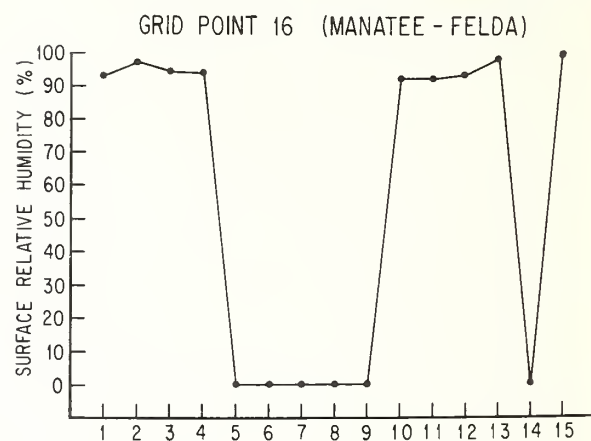
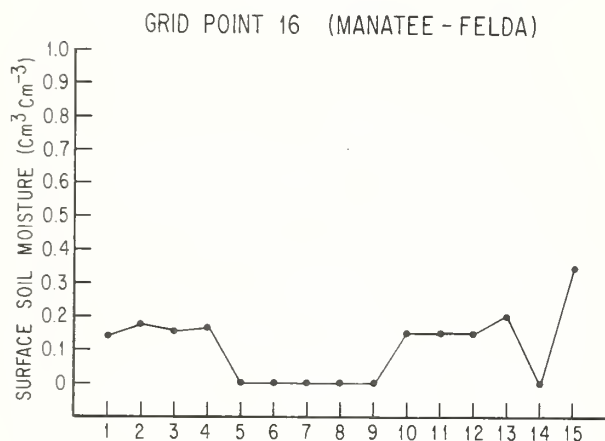
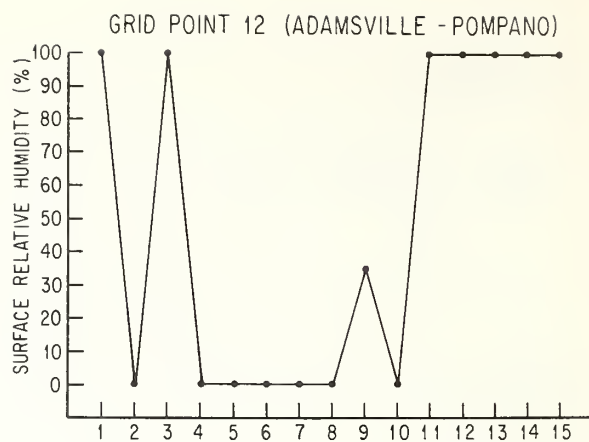
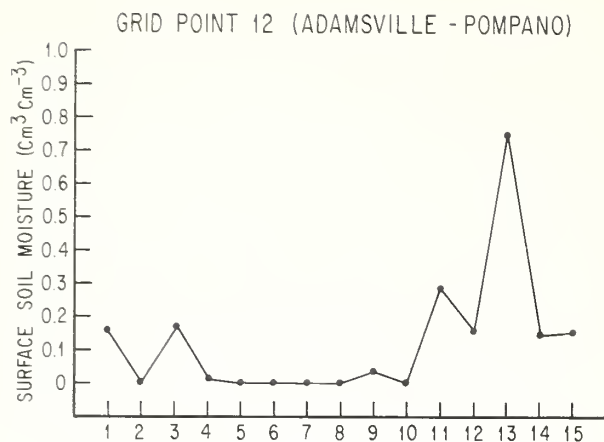


Figure C-1. Soil moisture and surface relative humidity estimates from July 1 to July 16, 1975, at grid point 12, grid point 16, and grid point 21.

soils having a large percentage of sand, roughly one-half of the days show very dry soils and one-half are near or at saturation. That is, the sandy soils are either at saturation or near-zero soil moisture. Conversely, the peat muck soils are largely maintained at near-saturation levels by the sluggish drainage rates.

Figure C-1 shows time histories of soil moisture and relative humidity for three of the four soil types. The large day-to-day variations in surface relative humidity with relatively small changes in surface soil moisture are seen for the first half of the period at grid point 12. The latter half of the period shows soil moisture increasing and humidities at saturation or above. At grid point 16, the same general pattern is seen; however, the oscillations in surface relative humidity seen at grid

point 12 are missing during the first four days in July. At grid point 21, soil moisture is seen to decrease steadily from July 6 to 10; however, relative humidity remains at or near 100% until July 11, when it decreases sharply. Recovery to 100% relative humidity occurs on July 13 with a relatively small increase in soil moisture.

The curves reflect, overall, the rapid change in surface relative humidity which occurs with very limited changes in surface soil moisture. As the ratio between surface latent and sensible heat flux to the atmosphere will change most rapidly once the drying phase commences, it is vital that reliable soil moisture estimates or observations be made on a daily basis. The temporal and spatial variance of surface relative humidity precludes dependence upon persistence.



Environmental Research LABORATORIES

The mission of the Environmental Research Laboratories (ERL) is to conduct an integrated program of fundamental research, related technology development, and services to improve understanding and prediction of the geophysical environment comprising the oceans and inland waters, the lower and upper atmosphere, the space environment, and the Earth. The following participate in the ERL missions:

MESA	<i>Marine EcoSystems Analysis Program.</i> Plans, directs, and coordinates the regional projects of NOAA and other federal agencies to assess the effect of ocean dumping, municipal and industrial waste discharge, deep ocean mining, and similar activities on marine ecosystems.	GLERL	<i>Great Lakes Environmental Research Laboratory.</i> Studies hydrology, waves, currents, lake levels, biological and chemical processes, and lake-air interaction in the Great Lakes and their watersheds; forecasts lake ice conditions
OCSEA	<i>Outer Continental Shelf Environmental Assessment Program Office.</i> Plans and directs research studies supporting the assessment of the primary environmental impact of energy development along the outer continental shelf of Alaska, coordinates related research activities of federal, state, and private institutions.	GFDL	<i>Geophysical Fluid Dynamics Laboratory.</i> Studies the dynamics of geophysical fluid systems (the atmosphere, the hydrosphere and the cryosphere) through theoretical analysis and numerical simulation using powerful, high-speed digital computers.
W/M	<i>Weather Modification Program Office.</i> Plans and coordinates ERL weather modification projects for precipitation enhancement and severe storms mitigation.	APCL	<i>Atmospheric Physics and Chemistry Laboratory.</i> Studies cloud and precipitation physics, chemical and particulate composition of the atmosphere, atmospheric electricity, and atmospheric heat transfer, with focus on developing methods of beneficial weather modification
NHEML	<i>National Hurricane and Experimental Meteorology Laboratory.</i> Develops techniques for more effective understanding and forecasting of tropical weather. Research areas include: hurricanes and tropical cumulus systems; experimental methods for their beneficial modification.	NSSL	<i>National Severe Storms Laboratory.</i> Studies severe-storm circulation and dynamics, and develops techniques to detect and predict tornadoes, thunderstorms, and squall lines
RFC	<i>Research Facilities Center.</i> Provides aircraft and related instrumentation for environmental research programs. Maintains liaison with user and provides required operations or measurement tools, logged data, and related information for airborne or selected surface research programs.	WPL	<i>Wave Propagation Laboratory.</i> Studies the propagation of sound waves and electromagnetic waves at millimeter, infrared, and optical frequencies to develop new methods for remote measuring of the geophysical environment.
AOML	<i>Atlantic Oceanographic and Meteorological Laboratories.</i> Studies the physical, chemical, and geological characteristics and processes of the ocean waters, the sea floor, and the atmosphere above the ocean	ARL	<i>Air Resources Laboratories.</i> Studies the diffusion, transport, and dissipation of atmospheric pollutants; develops methods of predicting and controlling atmospheric pollution; monitors the global physical environment to detect climatic change.
PMEL	<i>Pacific Marine Environmental Laboratory.</i> Monitors and predicts the physical and biological effects of man's activities on Pacific Coast estuarine, coastal, deep-ocean, and near-shore marine environments.	AL	<i>Aeronomy Laboratory.</i> Studies the physical and chemical processes of the stratosphere ionosphere, and exosphere of the Earth and other planets, and their effect on high-altitude meteorological phenomena.
		SEL	<i>Space Environment Laboratory.</i> Studies solar-terrestrial physics (interplanetary, magnetospheric, and ionospheric); develops techniques for forecasting solar disturbances, provides real-time monitoring and forecasting of the space environment.

U.S. DEPARTMENT OF COMMERCE
National Oceanic and Atmospheric Administration
 BOULDER, COLORADO 80302

PENN STATE UNIVERSITY LIBRARIES



A000072021958